Spring 5-5-2023

Application of Particle Transfer by Dipping Using Polymer Binder

Md Ibrahim Khalil
md.khalil@maine.edu

APPLICATION OF PARTICLE TRANSFER BY DIPPING USING POLYMER BINDER

By

Md Ibrahim Khalil

B.Sc. Bangladesh University of Engineering and Technology, 2017

A THESIS

Submitted in Partial Fulfillment of the

Requirements for the Degree of

Master of Science

(in Mechanical Engineering)

The Graduate School

The University of Maine

May 2023

Advisory Committee:

Bashir Khoda, Associate Professor, Mechanical Engineering Department, Advisor

Khalid Jawed, Assistant Professor, Mechanical and Aerospace Engineering Department

William Gramlich, Associate Professor, Department of Chemistry

Yingchao Yang, Associate Professor, Mechanical Engineering Department

APPLICATION OF PARTICLE TRANSFER BY DIPPING USING POLYMER BINDER

By

Md Ibrahim Khalil

Thesis Advisor: Dr. Bashir Khoda

An Abstract of the Thesis Presented
in Partial Fulfillment of the Requirements for the
Degree of Master of Science
(in Mechanical Engineering)
May 2023

The demand for particle transfer is increasing in various industries, such as manufacturing, metal joining, microfluidics, roller lubrication process, fuel cells, super-capacitors, hybrid coating, and protective layer applications. As a result, the importance of efficient transfer of solid micron-size particles is becoming more crucial. Submicron-sized particles can easily adhere to solid substrates due to negligible gravitational force, while micron-sized or larger particles require a binder to overcome the gravitational effects. This thesis aims to investigate the interactions between micro-particles and polymer thin film on cylindrical substrates using particle transfer methods. The process parameters are optimized and demonstrated two applications of this process: sorting particles based on their size from poly-disperse particle mixtures and controlling the friction force of the rods.

To transfer particles into a substrate, a density-mismatching heterogeneous suspension is utilized, where kinetic energy is supplied by a magnetic stirrer's rotation to keep the particles suspended during transfer. Initially, the effect of magnetic stirrer rotation and binder concentration on the optimal particle transfer was investigated. As a result of optimizing process parameters, a novel technique was developed for filtering poly-disperse particles from density mismatching

heterogeneous mixtures at the solid-liquid interface (submerged condition) using entrapment instead of the conventional entrainment approach used in dip-coating processes. The polymer layer thickness formed over the substrate is controlled by controlling the binder concentration in the suspension. The binder concentration is varied from ϕ_b = 1% to ϕ_b = 13% at different intervals and the particle concentration is kept fixed ϕ_p = 10%. The viscosity is measured at room temperature (25 ºC) to observe the behavior of the suspension using a rotational rheometer. The variation in the polymer layer thickness controls the size of the entrapped particles. This work successfully showed the size-based separation of particles from a poly-disperse particle mixture.

Another aspect of this thesis involved the systematic control of frictional forces between elastic rods in contact by transferring particles via dip-coating. Non-spherical particles adhere to the rods using a polymeric binder. A custom continuous dip-coating setup was constructed in the laboratory to coat the elastic rods. The particle delivery over the rods is regulated by controlling the concentration of particles in the suspension. Particle concentration in the suspension is varied from ϕ_p = 1% to ϕ_p = 13% at different intervals to observe the effect of variation of particle concentration keeping the binder concentration fixed (ϕ_b = 5%). The coated rods are dried in the oven to overcome the effect of the solvent during the friction force measurement. Table-top experimental setup with a push-pull digital force gauge is used to measure the variation friction force at different pulling lengths of overhand knots with a variety of unknotting numbers. This work successfully demonstrates a novel method of controlling the friction force of elastic rods by controlling the particle concentration in the suspension.

DEDICATION

This thesis is dedicated to my wife and my mother.

TABLE OF CONTENTS

LIST OF TABLES

LIST OF FIGURES

CHAPTER 1

INTRODUCTION

Particle transfer using thin polymer film (< 5 μm) is of great interest in the scientific community for the last few decades. When the size of the particles is submicron, i.e., the effect of gravity is negligible, particles adhere to the substrate almost effortlessly [1] by using the adhesion force between the particles and substrate which is the result of one or more attraction forces (van der Waals and electrostatic forces [2], covalent and acid-base reactions [3], or surface asperities [4]). However, with the increase in the particle size gravitational force of the particles becomes stronger, so a binder is required to transfer those particles. Thin-film based particle transfer method is used in different industrial applications including modification of cutting tools [5], corrosion protective layers [6, 7], wire coating [8, 9], radio frequency identification [10], e-paper [11], batteries [12], particle filtration [13, 14], controlling friction [15].

Depending on the operating condition different particle delivery methods are applied. For uniform thin film generation, physical vapor deposition [16, 17], chemical vapor deposition [18, 19], or plasma sputtering [20, 21] are very popular, however, these methods are very slow, arduous, and expensive at large-scale production. Wet-deposition techniques are very faster and can be applied in atmospheric conditions, and a liquid carrier system (LCS) is used to carry and deliver the particles to the desired site such as Langmuir-Blodgett [22], dip coating, and spin coating [23]. High-density microparticles and nanoparticles are carried toward the receiver substrate using the liquid carrier system. Evaporation-based dip coating method is the simplest, facile to scale up, low-cost, waste-free, and low-energy consumption among all the wet-deposition methods [24]. A thin film is generated over the interfacial region of the substrate during the withdrawal of the substrate from the liquid bath [25]. The film thickness is determined by the competition between

the viscous drag force and capillary force [26]. The thickness of the liquid film for a Newtonian fluid formed over a flat solid substrate is proposed by Landau Levich [27], and Derjaguin [28] in 1942 , which is known as the famous LLD equation, $h = 0.94\, l_c Ca^{2/3}$; where $l_c = \sqrt{\gamma/\rho g}$ is the capillary length and $Ca = \eta U/\gamma$ is the non-dimensional capillary number. Liquid film thickness by dip coating process is dependent on surface tension, density, viscosity of the liquid and withdrawal speed of the substrate from the solution. The LLD equation is suitable for low capillary number ($Ca < 10^{-2}$) and for the flat substrate which is later modified for different experimental conditions and expanded for different substrates like cylindrical rods, wires, ropes, fibers, and tubes. The addition of solid particles to the liquid solution obstructs the Newtonian behavior of the liquid which creates a complex rheological behavior which is first described by the mathematical expression of Einstein in 1911 [29]. The expression is modified considering the particle concentration of the suspension, particle shape, and shear rate.

The generated film over the substrate (flat, cylindrical, or complex substrate) is used as the vehicle for transferring solid particles to the substrate. Over the last few years, studies have explored the micron-scale large particle transfer from the suspension. Due to reduced surface area and higher particle-to-solution density ratio, micron-scale large particle creates negatively buoyant suspension while added to the liquid carrier system. External kinetic energy is required to keep the particles suspended during the transfer process. Several studies reported particle transfer by entrainment using neutrally buoyant suspensions. Gans et. al. [30] used density matching suspension of polystyrene particles (20, 40, 70, and 125 μm radius) with dense and viscous silicone oil to investigate the effect of the volume fraction of particles during particle transfer. They also measured the liquid film thickness and observed that it remained consistent across a wide variety of withdrawal speeds. In another work, the effect of withdrawal velocity, particle size, and volume

fraction of particles is investigated on particle transfer by using neutrally buoyant suspension consisting of PEGPG (poly (ethylene glycolran-propylene glycol)-mono butyl-ether) water solution and polystyrene particles (80,145, and 550 μm diameter) [30-32]. Sauret et. al. [33] experimentally disclosed the dependency of thin film and particle size and showed that a thin film can transfer a particle that is six times larger than the thin film. The particle transfer process and the effect of particle transfer from density mismatching heterogeneous mixture are yet to be disclosed.

The most common powder manufacturing process includes gas atomization, plasma atomization, and plasma rotating electrode and the resulting powders from these processes are mostly poly-disperse. The distribution of the produced particles from these processes follows rosin-rammler expression [34]. A narrow size range of the particles is desired during manufacturing application [35-37]. In this thesis, the process parameters of particle transfer process are optimized to achieve the maximum particle transfer and using the entrapment method a novel particle sorting process from a poly-disperse particle mixture was demonstrated. Spherical particles are used for the sorting of particles. In another work, a systematic variation of the friction force of elastic rods was demonstrated by transferring irregular-shaped particles using entrainment.

Note: Chapters 2 to 4 of this thesis consist of research articles as those were presented in the journal or preparation stage journal. Chapter 2 is in the preparation stage for journal submission. Chapter 3 is published in a renowned journal titled Journal of **Manufacturing Science and Engineering** (DOI: 10.1115/1.4052440), and chapter 4 is published in another reputed journal named **Journal of Applied Mechanics** (DOI: 10.1115/1.4055544).

CHAPTER 2

EFFECT OF ROTATION OF STIRRER ON PARTICLE TRANSFER BY ENTRAPMENT

Abstract

The utilization of thin films to entrap particles is a fundamental concept in particle transfer and various industrial applications. When the density of particles and the solution are similar, particles can remain suspended in the solution without the need for external energy. However, in situations where there is a density mismatch with high-density particles, a rotating magnetic stirrer is used to provide kinetic energy to keep the particles suspended. Instead of using the traditional dip-coating process, a novel entrapment method was employed to transfer the particles. This method employs the viscous force of the thin polymer film that is formed over the substrate when it is submerged, to trap the particles. During the rotational motion, the particles come in contact with the thin polymer film and get entrapped. In this study, we will systematically investigate the effect of the rotational speed of the stirrer on particle transfer. Our findings show that the particle transfer rate increases with the increase of the rotational speed up to a certain speed (minimum suspending speed at 250 rpm). However, after that speed, the particle transfer rate decreases with the increase of the rotational speed of the stirrer. We also examined the effect of varying the polymer concentration on particle transfer. Additionally, we demonstrated that this entrapment method can be utilized as a novel size-based particle sorting application by altering the thickness of the polymer film.

Introduction

Solution-derived particle transfer using suspension is of great interest in different engineering applications [38, 39]. Improved understanding of the particle transfer process using the thin film

technology can be successfully used in tubular-shaped blood vessels [40], filtration systems [13, 41], flexible electronics [42], biosensors [43], corrosion protective layers [6, 7], and optical displays [44, 45]. When a solid material is immersed in a liquid, a thin film of uniform thickness forms on the surface of the material, ranging from several to hundreds of micrometers, depending on the process parameters employed in the coating method [39]. A thin irreversible adsorbed polymer film is formed over the substrate when it is submerged in the suspension [46]. The thickness of this film can be controlled by adjusting the concentration of the binder present in the suspension, which also governs the size of the particles that become trapped within it. The thickness of the film was determined in pioneering works for the flat plate a non-evaporating solution by Land-Levich and then Derjaguin [27, 28] which is later modified for fiber and cylindrical geometries [1, 47]. In most of the previous works, thin film formation and particle transfer were well-studied for dilute suspensions.

The introduction of particles into a solution leads to complex rheological behavior in the resulting suspension, which has garnered significant attention within the scientific community. Incorporating solid particles into a suspension hinders its rheological behavior, resulting in a shift towards a non-Newtonian behavior at higher solid particle loadings. In a non-Newtonian regime, the viscosity of the suspension is defined as apparent viscosity $\eta_r = \tau/\dot{\gamma}$; where τ is the imposed shear stress and $\dot{\gamma}$ is the shear rate. Initially, Einstein proposed an equation to find the viscosity of suspension with low particle concentration in the suspension [29]. However, Einstein's equation is later modified by Krieger and Dougherty [48] to measure the viscosity at higher particle concentrations and low to high shear rates. Previous studies were focused on the rheology of suspensions containing density-matching particles to investigate the impact of particle transfer through the dip coating method [30, 31, 49]. They demonstrated the influence of viscosity and

withdrawal speed on both film thickness and particle transfer. Working with inorganic particles (IP) of higher density adds an additional layer of complexity, as these particles tend to sediment when added to the solution. To prevent sedimentation, an external source of kinetic energy such as a magnetic stirrer is required to keep the particles suspended [25, 50]. To comprehend the process of particle suspension in a fluid, it is necessary to understand the behavior of the rotating fluid. Despite the magnetic stirrer being a widely used tool in laboratories, the flow pattern has not been thoroughly investigated as of yet. Halasz et al. [51] conducted the first theoretical and experimental investigation of the flow pattern generated by a cylindrical magnetic stirrer in a cylindrical container using optical observations. They demonstrated the formation of vortexes during rotating flow using particle image velocimetry (PIV) and established simple relationships for the vortex parameters based on the measured data. In another work, Mahmud et al. [52] conducted a study on the hydrodynamics of an unbaffled vessel agitated by a cylindrical magnetic stirrer. They used a combination of numerical and experimental methods, including high-speed video cameras and Laser Doppler Velocimetry (LDV), to compute the three components of mean velocity and turbulent kinetic energy. They compared the experimental results with the numerical simulations and found that the flow pattern generated by the magnetic stirrer played a crucial role in suspending all the particles in the vessel. Therefore, understanding the hydrodynamics of magnetic stirred vessels is vital for optimizing particle suspension in various industries such as pharmaceutical and chemical applications.

The level of agitation plays a crucial factor in determining the quantity of suspended particles in a suspension. As the speed of the stirrer increases, the particles that were initially settled at or near the bottom of the vessel begin to suspend. The minimum agitation speed required to keep all the particles uniformly dispersed in the suspension is known as the minimum suspending speed.

Numerous studies have been conducted to experimentally determine the minimum suspending speed. The visual method, which involves observing the behavior of solids in a liquid, is the most traditional and widely used experimental technique for determining the minimum agitation speed required to suspend particles. Specifically, this speed is defined as the velocity at which no solid particles remain stationary at the bottom of the container for a minimum of one to two seconds [53, 54]. Zwietering [53] developed an empirical correlation, utilizing dimensional analysis, to determine the minimum agitation speed based on various parameters. However, this equation is only accurate for a small percentage of solid loading. For higher solid loading in the suspension, the exponent of solid loading was modified in the subsequent research [55, 56]. An alternative method for determining the minimum suspending speed required to suspend particles is solid sampling [57, 58]. The solid sampling method involves weighing slurry samples that have been withdrawn and dried at different agitation speeds. The minimum agitation speed required for particle suspension is determined by identifying the speed at which the maximum amount of solid is transferred. Among the other methods of determining the minimum suspending speed Particle Bed Height method [59, 60], Steady Cone Radius method [61, 62], Pressure Gauge Technique method [63-65], Cloud Height method [66, 67], Power Number method [67, 68], Local Particle Concentration method [69-71] are notable. Prior research has primarily been devoted to exploring the minimum agitation speed required for particle suspension in turbine-reactor systems. To the best of our knowledge, there has been no investigation into the minimum agitation speed required for particle suspension in magnetic stirrers.

The aim of this study was to investigate the impact of kinetic energy, in the form of rotation, and binder concentration on particle transfer using adsorbed polymer films. A novel entrapment method was utilized as the mechanism for particle transfer. Spherical brazing particles were

transferred to a polymer thin film, and the film thickness varied depending on the concentration of binder in the suspension. This article is organized as follows: Section 2 focuses on the experimental methodology employed in this study. Section 3 presents the results of the investigation into the effect of kinetic energy and binder concentration on particle transfer. In section 4 a theoretical model for the entrapment mechanism and provides a discussion of the results is proposed. Finally, the study's findings are summarized in the concluding remarks presented in section 5.

Experimental Method

The experiments in this study were conducted using a density-mismatching heterogeneous suspension. The suspension was prepared using a combination of a granular solute binder (PMMA; molecular weight 350K), a solvent (1,3-Dioxolane), and solid spherical brazing particles (Nicrobraz LM). A high molecular weight binder was utilized in this study because particle transfer is enhanced with an increase in the length of polymer chains at higher molecular weights [72]. The liquid carrier system, comprised of a mixture of solute and solvent, facilitated the transport of particles to the desired location. Both the solute and solvent were procured from Sigma Aldrich in the USA. At room temperature (25ºC), the density of the solute and solvent was approximately 1.17 g/cm^3 and 1.06 g/cm^3, respectively. The surface tension of the solute and solvent was approximately 41 mN/m and 34.3 mN/m, respectively. It is important to note that both the surface tension and density of the solution are dependent on the concentration of the binder and solvent, which are calculated using a weighted average of the binder and solvent [31, 73]. Table 4 presents the values of various properties of the suspension. To dissolve the granular in the solvent, a magnetic stirrer is used for six hours. The dissolution of the binder is confirmed through a dynamic light scattering (DLS) experiment in the LCS solution. The viscosity of the solution is measured

using Anton Paar MCR 302 Rheometer with a parallel plate/plate geometry of 50 mm diameter and a 0.3 mm gap filled with the sample. The viscosity is measured at a variable shear rate.

Solid inorganic brazing particles (Nicrobraz LM) with a spherical diameter range of approximately 0-100 μm were added to the liquid carrier system to prepare the suspension. The particles create a complex behavior with the solution, which has been reported in various previous works. The Nicrobraz LM particles were procured from Wall Colmonoy company in Ohio. In a previous article, Mueller et al [74] demonstrated three regimes: (i) dilute regime ($\phi_p \leq 2\%$), semi-dilute regime ($\phi_p \leq 25\%$) and the concentrated regime ($\phi_p \geq 25\%$). In the dilute regime, the suspension behaves according to Newtonian rheology, while in the concentrated regime, the viscosity rapidly increases, leading to behavior similar to non-Newtonian fluids. In semi-dilute regime, suspension rheology can be approximated as Newtonian fluid [74]. In some previous articles, it was observed that the suspension exhibits Newtonian behavior even for higher volume fractions of micron-sized particles [75, 76]. The experiments in this study were conducted using a constant volume fraction of particles (ϕ_p = 10%), resulting in a Newtonian fluid behavior. The volume fraction of the binder was varied to investigate the entrapment effect with magnetic stirrer rotational speed. The particle dispersion was improved by sieving using a Gilson Performer III shaker through Stainless Steel 635 Mesh (20 μm), and the size of the particles was analyzed using SEM and ImageJ software, which determined an average size of 7.56 ± 3.98 μm. The density of the particles was approximately 7.97 g/cm^3, which was nearly eight times higher than the density of the solution, creating a density imbalance that caused sedimentation and separation in the suspension. To counteract the gravitational effect of the particles, external energy in the form of kinetic energy was required, which was provided by a cylindrical magnetic stirrer measuring 14.88

mm in length and 5.95 mm in diameter. The stirring action created normal stresses that lifted and suspended the particles, resulting in a dispersed mixture ("pseudo suspension").

Table 1: Different physical properties of the suspension.

Binder concentration (%)	Particle concentration (%)	Surface tension of the solution (mN/m)	Density of the solution (g/cm^3)	Viscosity of the solution (mPa.s)	Viscosity of the suspension (mPa.s)
0.2	10	34.313	1.06022	0.701	0.920
0.4	10	34.327	1.06044	1.496	1.964
0.7	10	34.347	1.06077	1.516	1.989
1.0	10	34.367	1.06110	1.741	2.285

AISI 1006 mild steel substrate rods with a diameter of 1.1 mm were used as the substrate for the experiments. The rods were cleaned by immersing them in an ultrasonic bath of acetone for one hour to remove any surface contaminants and passive film. A 20 mL 95020-0 CV Vial with a screw top and a round bottom was used as the dipping reactor, with dimensions of 75.5 × 22.5 mm. For all the experiments, a custom-made dip coating setup was utilized, which was described in a previous article [13]. The coating setup's movement is precisely controlled by a stepper motor (SANYO), which is connected to a Flashcut CNC controller and can maintain a precision of within ±2%. The suspension was stirred at seven different rotational speeds of the magnetic stirrer (100 rpm to 400 rpm in 50 rpm intervals) to examine the effect of rotation during the particle transfer process. To stabilize the suspension at the respective speed, the suspension was stirred for five minutes before dipping the substrate. The substrate was then inserted into the stirred suspension at a speed of 10 mm/s, and the total dwelling time was 25 minutes, with the stirrer's rotation continuing for the first 15 minutes to keep the particles suspended during particle transfer, and the remaining 10 minutes were used for particle sedimentation. To avoid particle loss due to the substrate's vibration, the substrate was withdrawn from the suspension at a slow speed of 3 mm/s.

Entrapment tests were conducted immediately after the sedimentation time, and no particle transfer was observed, confirming that the particles are transferred only by entrapment during the tests, rather than traditional entrainment. To ensure repeatability, each test was conducted three times.

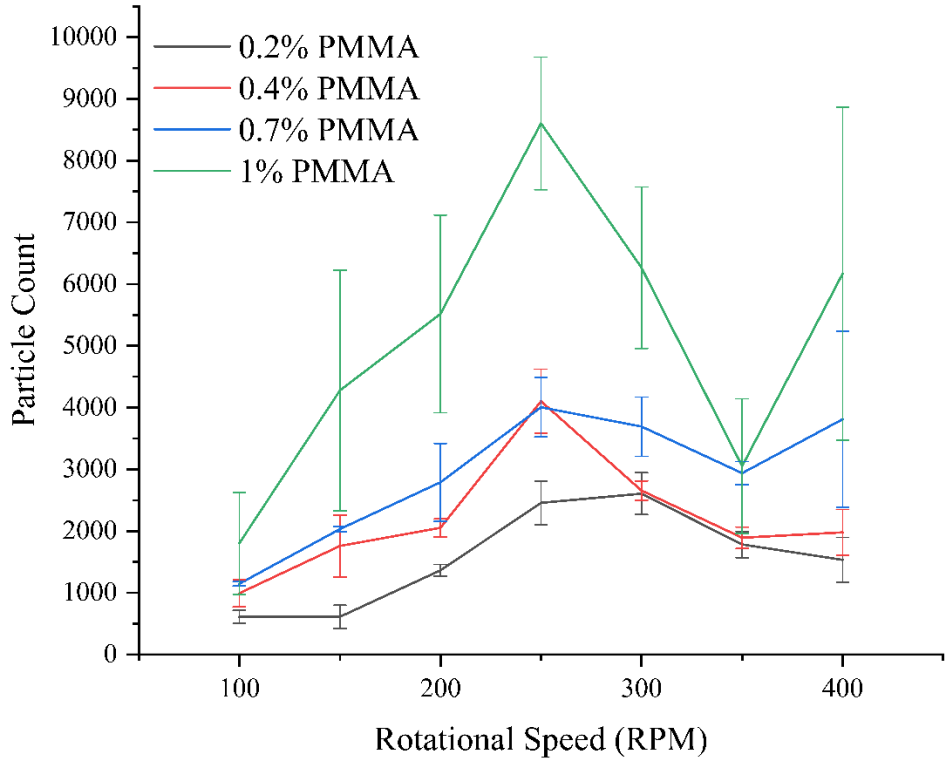

Figure 1: Variation of Particle count with the speed of the rotation.

Once the particles were transferred onto the rods via entrapment, the rods were dried in an oven to remove any remaining solvent, and then imaged at 1000X magnification using a VHX 7000 Digital 4K microscope from KEYENCE corp. Characterizing the images of the coated rods is critical for measuring the efficiency of particle transfer. However, this is a time-consuming process due to the large volume of transferred particles and the lack of contrast between the particles and the substrate. Conventional image analysis tools such as ImageJ and variable thresholding methods are not suitable as they introduce significant errors. To address this issue, we employed a customized object detection algorithm, YOLOv5, based on deep learning techniques. We divided

each substrate into two sides and took three images (bottom, middle, and top) from each side, resulting in six images per substrate. We repeated each test three times to ensure statistical significance, and a total of eighteen images were used to create the dataset for each composition and speed.

Results

We start the analysis by examining the entrapment of micron-sized particles onto the coated rods under different rotational speeds of the magnetic stirrer. The entrapment mechanism involves the kinetic energy of particles getting trapped in the polymer thin film. In our previous research, we focused on sorting particles of different sizes from poly-disperse particle mixtures by leveraging the variation of thin polymer layer thickness [13]. We demonstrated entrapment of particles using a constant kinetic energy of 150 rpm rotation of the magnetic stirrer while varying the strength of the polymer film. In this study, we investigated the effect of varying the kinetic energy during the particle transfer process by changing the binder concentration in the suspension. The high molecular weight binder (350K) with longer polymer chains was found to enhance the intermolecular interaction with the particles and resulted in superior entrapment compared to the previously used low molecular weight binder (15K). The particle transfers initially increased with increasing rotational speed up to the minimum suspending speed, after which particle transfer by entrapment reduced as the kinetic energy of the particles exceeded the viscous strength of the thin polymer film. The entrapped particle size, particle count, and surface coverage variation are presented in table 5, and we observed three different regimes based on the variation of rotational speeds.

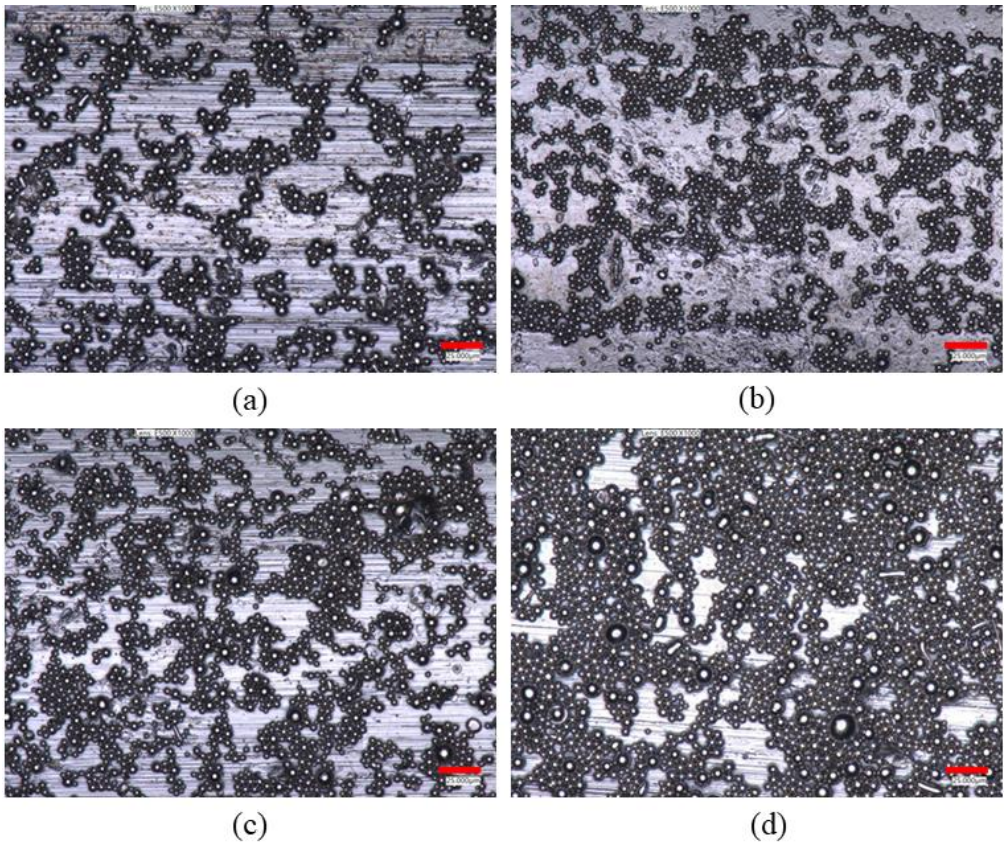

Figure 2: Particle transfer visualization at 250 rpm rotational speed. 0.2% binder concentration (a), 0.4% binder concentration (b), 0.7% binder concentration (c), 1% binder concentration (d). Scale bar is 25 μm for all images.

Low Rotation Regime

To better understand the effect of rotational speed, we carried out systematic variation of the speed at different binder concentrations. Specifically, we used a binder volume fraction $\phi_b \sim$ [0.2%, 0.4%, 0.7%, and 1%] with a constant particle volume fraction (ϕ_p = 10%) and an evaporating solvent. Prior to introducing kinetic energy to the suspension via rotation of the magnetic stirrer, particles were sedimented at the bottom of the reactor due to gravity. As the stirrer rotated, the particles were able to remain suspended in the solution, forming a thin polymer film over the substrate. The particles hit this film and became entrapped due to the viscous force of the polymer. The probability of particle transfer via entrapment is influenced by two key factors: binder

concentration and the probability of hitting the film, which is linked to the number of suspending particles. Our findings indicate that, at a specific binder concentration, particle transfer increases systematically with the rotational speed (up to 250 rpm). Similarly, at a specific rotation speed, we observed a similar trend with increasing binder concentration in the suspension.

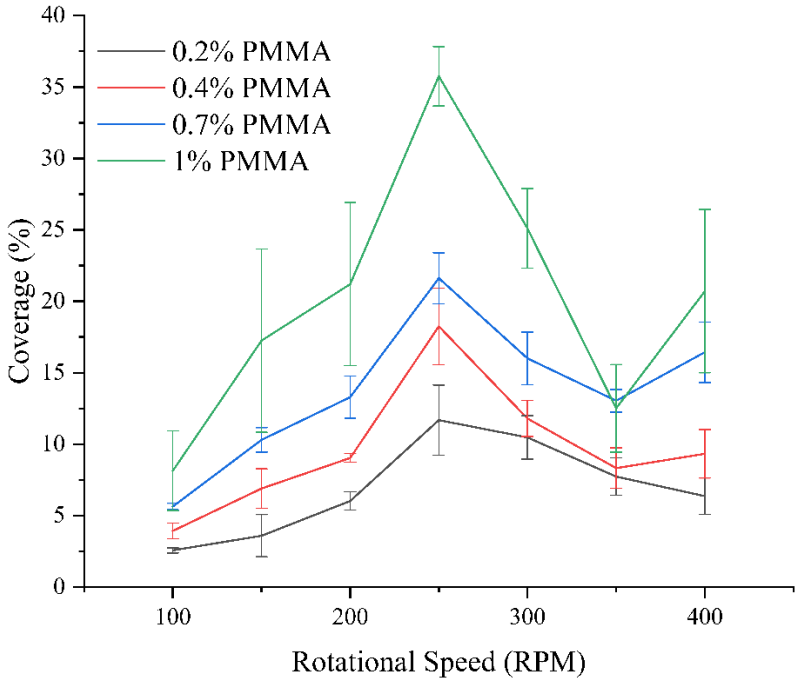

Figure 3: Variation of surface coverage with rotational speed.

In the low viscosity range (< 1 mPa.S), there is a slower rise in particle count with increasing rotational speed. However, in the high viscosity range (> 1 mPa.S), a steep increase occurs due to the thicker polymer film (as shown in figure 1). Surprisingly, a similar increase in surface coverage is observed at low rotational speeds, despite the larger particle entrapment in low viscosity. This phenomenon is counterintuitive. In the low rotation regime, the maximum particle size shows minimal increase, as not all particles remain suspended at those speeds. The maximum entrapped particle size is observed when the suspension viscosity is at its maximum (1.24 mPa.S).

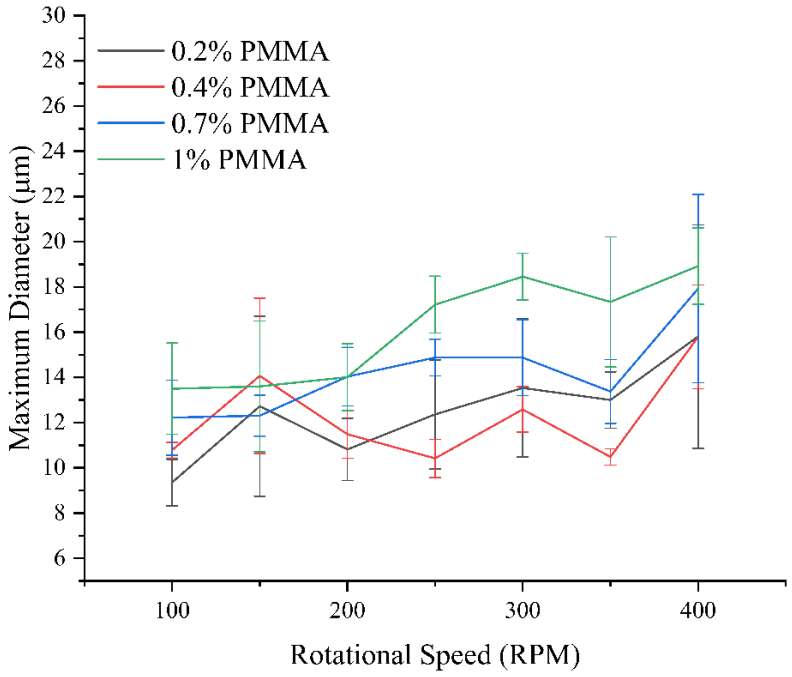

Figure 4: Variation of the maximum size of the entrapped particles with rotational speed.

Minimum Suspending Speed

During the stirring of a suspension with a stirrer, three distinct zones can be observed. The first zone is a clear transparent area with no visible particles, the second zone is a suspended area where particles are suspended, and the third zone is a dense region where particles are not suspended. The size of the suspended zone increases with the kinetic energy of the stirrer. To maximize the yield during the particle transfer process, it is essential to optimize the hydrodynamic interactions between the particles and the solution to ensure maximum contact between them. The minimum speed required to keep all particles suspended in an agitated reactor is the speed at which the particles remain off the bottom of the reactor for at least one second [53]. Previous studies [57, 58], employed solid sampling from the suspension to ascertain the minimum suspending speed. They identified the minimum suspending speed as the point where the solid weight reaches its maximum. However, these previous studies mainly focused on using a turbine for stirring, whereas

this current investigation is centered on determining the minimum suspending speed for suspensions using a magnetic stirrer, which is widely utilized in laboratory-scale experiments.

Table 2: Variation of particle count, surface coverage, and particle size at different binder concentrations and rotational speeds.

Binder concentration (%)	Rotational Speed	Particle Count / 0.4 mm^2	Surface Coverage (%)	Minimum Particle diameter (µm)	Maximum Particle Diameter (µm)
0.2	100	611.00±106.00	2.56±0.17	1.87±0.14	9.35±1.03
	150	612.00±187.00	3.59±1.48	1.87±0.01	12.72±3.98
	200	1365.00±95.00	6.02±0.64	1.98±0.04	10.81±1.38
	250	2456.00±353.00	11.68±2.45	1.84±0.01	12.36±2.42
	300	2607.00±340.00	10.47±1.51	1.91±0.07	13.53±3.05
	350	1781.00±213.00	7.73±1.31	1.84±0.14	13±1.25
	400	1534.00±366.00	6.36±1.26	1.82±0.04	15.81±4.94
0.4	100	992.00±220.00	3.92±0.55	1.89±0.13	10.78±0.34
	150	1758.00±501.00	6.88±1.38	1.87±0.01	14.07±3.44
	200	2053.00±147.00	9.00±0.29	2.04±0.06	11.48±1.06
	250	4104.00±519.00	18.24±2.68	1.79±0.06	10.42±0.84
	300	2655.00±157.00	11.79±1.25	1.85±0.05	12.59±1.01
	350	1892.00±174.00	8.32±1.42	1.77±0.04	10.49±0.36
	400	1977.00±374.00	9.32±1.69	1.82±0.03	15.79±2.29
0.7	100	1148.00±36.00	5.64±0.22	1.79±0.01	12.22±1.66
	150	2032.00±42.00	10.29±0.85	1.67±0.04	12.31±0.91
	200	2789.00±633.00	13.28±1.47	1.99±0.07	14.03±1.3
	250	4005.00±482.00	21.61±1.78	1.87±0.06	14.88±0.81
	300	3692.00±480.00	16.00±1.83	1.89±0.06	14.88±1.67
	350	2939.00±187.00	13.03±0.79	1.79±0.04	13.38±1.41
	400	3812.00±1424.00	16.43±2.11	1.8±0	17.92±4.17
1.0	100	1800.00±824.00	8.14±2.78	2.15±0.13	13.5±2.02
	150	4278.00±1947.00	17.25±6.41	2.01±0.07	13.6±2.89
	200	5518.00±1601.00	21.20±5.71	1.92±0.04	14.02±1.49
	250	8604.00±1075.00	35.75±2.07	1.99±0.04	17.22±1.26
	300	6267.00±1307.00	25.10±2.77	1.8±0.12	18.46±1.03
	350	3051.00±1091.00	12.51±3.06	1.91±0.23	17.34±2.88
	400	6170.00±2699.00	20.70±5.70	1.75±0.05	18.92±1.69

We utilized the maximum particle transfer method to determine the minimum suspending speed. In our experiments, the maximum particle count was observed at 250 rpm for all concentrations except for the 0.2% binder concentration (presented in figure 1), which represents the minimum suspending speed. The variation of transferred particles with the binder concentration at minimum suspending speed is shown in figure 2. We noted a systematic variation in particle transfer (both particle count and surface coverage) at the minimum suspending speed for different binder concentrations. However, the number of entrapped particles at 0.4% binder concentration was higher than at 0.7% binder concentration, possibly due to the smaller-sized nearly monodisperse particles entrapped at 0.4% binder concentration and larger-sized particles entrapped at 0.7% binder concentration. The surface coverage was maximum at 250 rpm for all binder concentrations, confirming the minimum suspending speed. The density variation of the solution with the change in binder concentration was insignificant (as listed in table 4), and the particle concentration was constant for all suspensions, which kept the minimum suspending speed constant.

High Rotation Regime

The uniformity of the particle suspension is disrupted once the rotation speed surpasses the minimum suspending speed, and particle transfer is hindered as well. Figures 1 and 3 demonstrate that particle count and coverage both decrease with the increase of rotational speed after the minimum suspending speed is reached. As the rotational speed of the magnetic stirrer increases, the kinetic energy applied to the particles increases. The entrapment of particles is influenced by the balance between the viscous force of the polymer film formed on the substrate and the kinetic energy of the particles. In the high rotational regime, particles collide with the thin polymer film

with greater kinetic energy and are pushed away from the polymer film due to its low viscous strength.

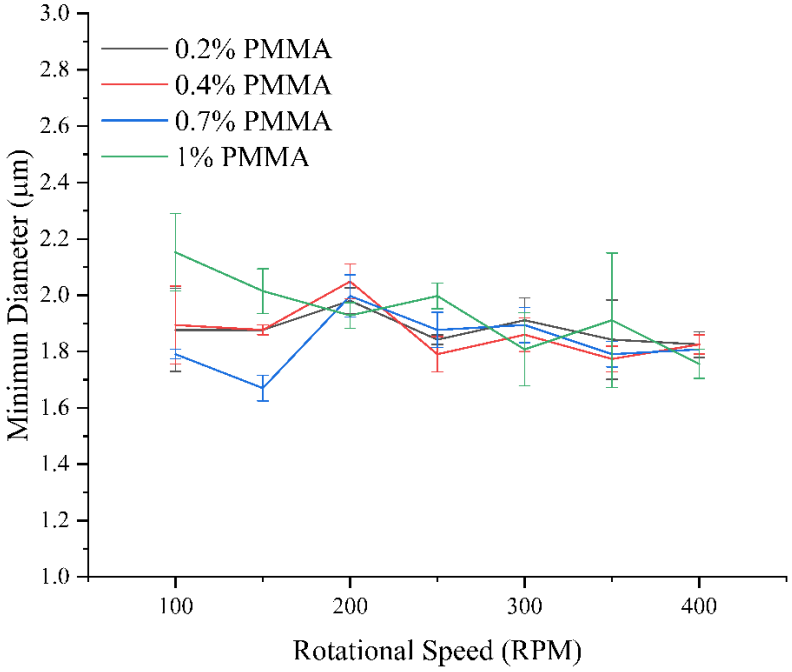

Figure 5: Variation of the maximum size of the entrapped particles with rotational speed.

We have observed a consistent decrease in both particle count and surface coverage entrapment with increasing rotational speed up to 350 rpm (as shown in figures 1 and 3). However, there was an unexpected increase in particle entrapment at 400 rpm, particularly for binder concentrations greater than 0.2%. This trend was also observed to systematically increase with higher binder concentrations. The increased viscosity of the suspension at higher binder concentrations may have contributed to this phenomenon. Moreover, we observed a steady increase in the maximum size of entrapped particles (figure 4), particularly at high rotational speeds above 200 rpm, with increasing binder concentration (except at 4% binder concentration).

Discussion

Entrapment Mechanism

In this section, we will propose a theoretical model for the entrapment of particles into the polymer film, which depends on the competition between the hydrodynamic forces of the fluid acting on the particle and the viscous force of the polymer film. To better understand this process, we have divided it into two stages: the collision between the thin polymer layer and the particle, and the sustainability of the particle entrapment. The collision stage determines the probability of particle entrapment, while the entrapment sustainability stage determines the sustainability of the particle entrapped in the thin polymer film.

Collision between thin polymer layer and particle

This stage initiates the particle entrapment to the polymer layer. The behavior of particle motion is a complex phenomenon which has been discussed in many articles in the last few decades. The Stokes number is a dimensionless parameter that quantifies the relative importance of inertial forces to viscous forces in the motion of particles in a fluid flow. It is commonly used to describe the behavior of particles in various fluid dynamic situations. Stokes' number is defined as follows [77, 78].

$$St = \rho_p V_p v_p / 6\pi\eta r_P^2 = (1/9) Re(\rho_p/\rho_f)$$

In the above-mentioned equation *St*, ρ_p, ρ_f, *Re*, η, v_p, V_p, and r_p are the stokes number, density of the particles, density of the solution, Reynolds number, viscosity of the suspension, velocity of the particles, volume of the particles, and radius of the particle respectively. In a very low Stokes numbers ($St << 1$), particles tend to closely follow the fluid streamlines, exhibiting laminar behavior and being strongly influenced by viscous forces. However, at high Stokes number the

particles are less responsive to the change in fluid flow behavior and resulted in more chaotic and inertial behavior.

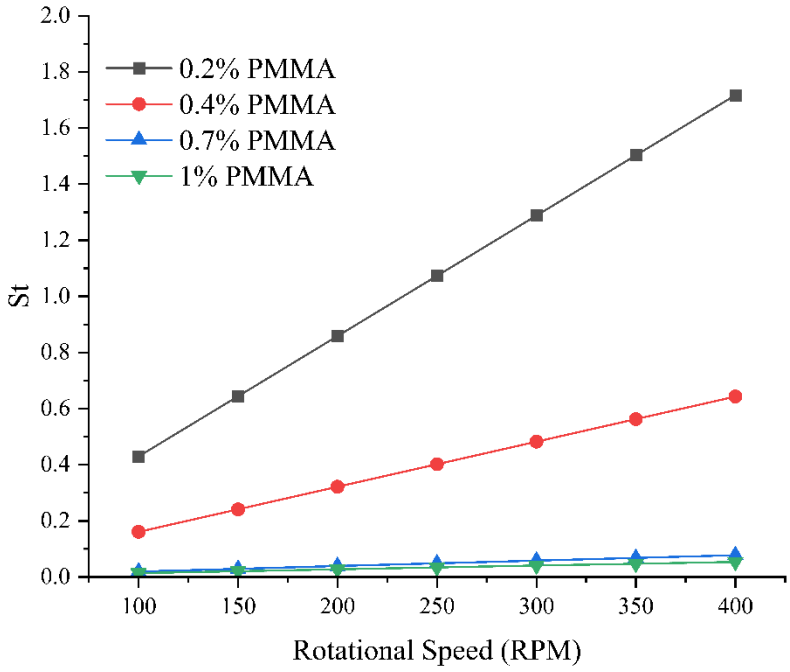

Figure 6: Variation of Stokes number with the variation of Rotational Speed and the binder concentrations.

Figure 6 illustrates the relationship between the variation of Stokes number and changes in rotational speed and binder concentrations within the suspension. In a specific viscosity range of the suspension, a systematic pattern emerges regarding the Stokes number and the magnetic stirrer's rotation speed. It becomes evident that as the rotational speed of the magnetic stirrer increases, the fluid flow transitions into a more turbulent state, deviating from the streamline behavior. Consequently, there is an increased incidence of particle collision with the polymer thin layer on the substrate, leading to a higher yield in particle transfer through entrapment (as depicted in figure 1). Conversely, as the viscosity of the suspension increases, the Stokes number decreases. This decrease signifies an increase in the drag force exerted by the fluid flow due to the elevated suspension viscosity. Consequently, the particle motion shifts towards the Stokes regime.

During the entrapment of particles into the polymer thin film, depending on the direction of contact, the impact of the particles can be categorized into two types: normal impact, which occurs when the particle hits the thin layer perpendicular to the substrate, and oblique contact, which refers to any other type of contact with the substrate. In this section, we will elaborate on the physics underlying these contacts. When a particle approaches the thin polymer layer, radial force assists in the particle's entry into the polymer layer, and the viscous resistive force acts opposite to the direction of particle entrapment for both normal and oblique contacts.

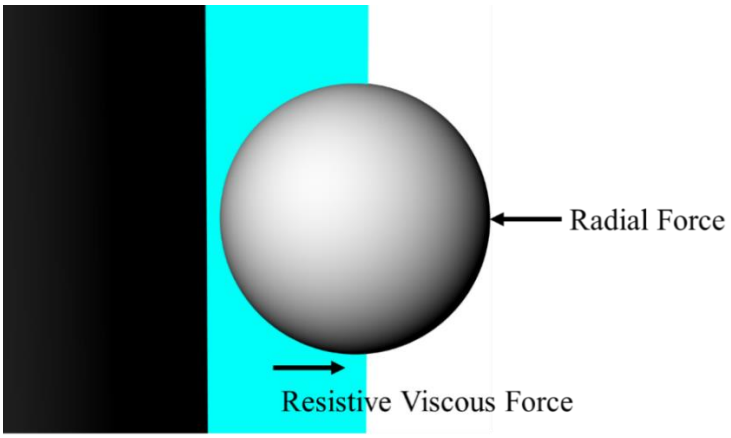

Figure 7: Forces acting on a particle during normal contact.

Normal impact

When particles come into normal contact with the polymer layer, the viscous fluid dynamic force arising from the polymer layer acts as resistance to particle entrapment [77], while the radial force helps in entrapment by providing energy gained by the particles from the rotation of fluids. Figure 7 illustrates the direction of these forces acting on the particles. Stoke's formula for the measurement of viscous drag force acting on the small particles during the fluid motion is presented below [77]:

$$F_V = \left(\frac{6\pi\eta r_P^2 v_P}{x}\right)\int_{\beta_1}^{\beta_2} cos\beta d\beta$$

In this equation, F_v, and x are the viscous force of the polymer film, thickness of the liquid film over the substrate. The velocity has three components along three rectangular co-ordinates. The integration method is used to calculate the viscous force in the contact surface area between the thin film and the particles. On the other hand, the radial force acting on the particle is expressed as

$$F_R = \rho_p V_p \frac{v_p^2}{R}$$

here, F_R is the radial for acting on the particles due to rotation of the fluid and R is the radius of the rotation of the particles during hitting into the polymer film. The radial force acting on the particles should be greater than the resistive viscous force of the polymer layer for the entrapment into the polymer layer.

Oblique impact

When particles hit the thin polymer layer at an angle (θ) with respect to the normal line of the substrate, the radial force component along the direction normal to the cylinder assists in particle entrapment. However, the viscous force of the polymer layer still resists entrapment, and the motion induced by the radial force facilitates entrapment into the thin polymer layer. Figure 8 (a) and (b) show two different modes of hitting during interactions between moving particles and the thin polymer film in oblique contact. In both cases, the horizontal component of the radial force aids in particle entrapment. The condition for particle entrapment in oblique contact with the polymer layer is described by:

$$F_R cos\theta > F_V$$

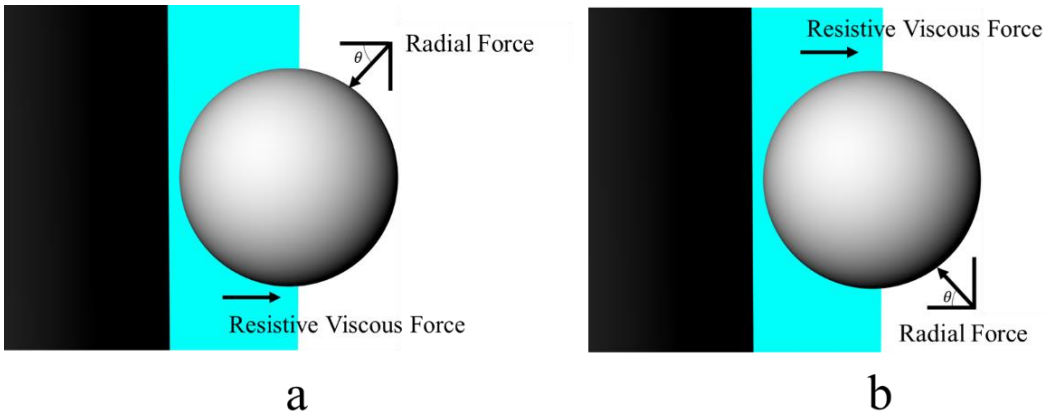

Figure 8: Direction of the forces acting on a particle during oblique contact. (a) particle hits the polymer film from upper direction, (b) particle hits the polymer film from the lower direction.

Post-impact and entrapment sustainability

The particles that have been entrapped into the polymer thin film experience various forces such as viscous fluid dynamic force, gravitational force, stokes drag force of the rotating fluid, and the surface tension force due to contact between the particles and the film (illustrated in figure 9 (a)). When the particle is in a steady condition in the polymer thin film, the combination viscous fluid dynamic force due to the contact between the polymer thin film and particle and the surface tension force acting in the contact line of the particles are considered as the adhesive force. The adhesive force on the particles acts to hold the particles in their location, on the other hand, the drag force of the fluid tries to roll the particle down from that location. The sustainability of the entrapped particles depends on the balance between the forces acting on the particles. The interaction between particles and a solid surface via an interposed liquid film has been discussed in several articles [79, 80]. This interaction is similar to the entrapment of particles in a polymer film. The adhesion force is due to the small amount of liquid present between the particles and solid surface. The surface tension force acting on the particles can be expressed as follows:

$$F_s = 2\pi T r_p \sin(\alpha)$$

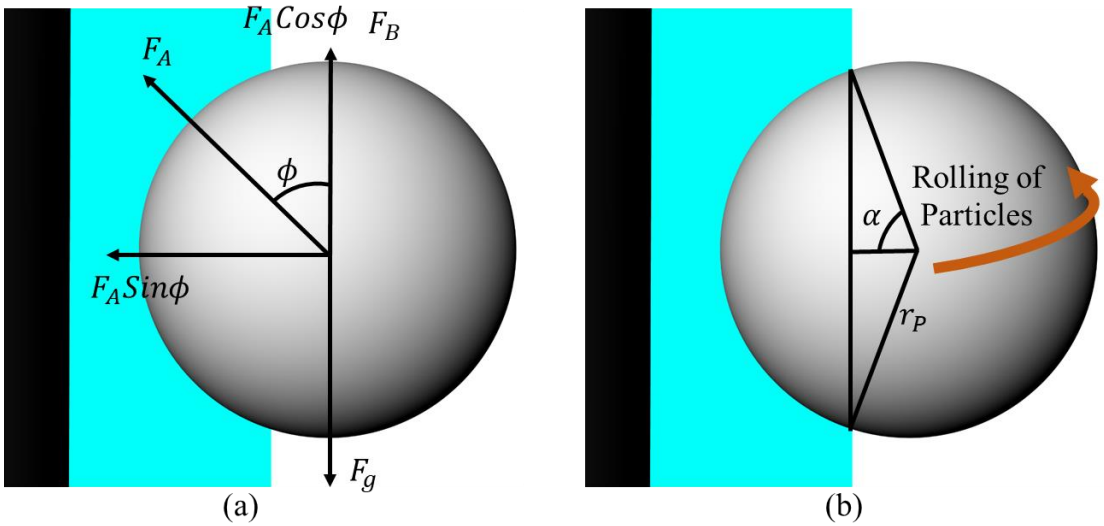

Figure 9: (a) balance of the forces after the entrapment of the particle in the polymer film. (b) direction of the rotation of particles due to drag force of the fluid.

where, T is the surface tension of the liquid, r_p is the radius of the particle and α is angle between the radius of the particle and the contact line of the particle with the polymer thin film (shown in figure 9 (b)). The gravity force is expressed as

$$F_g = \rho_p V_p g$$

here F_g is the gravity force and g is the acceleration due to gravity. Another possible case of particle removal from the polymer film is due to the action of tangential force on the entrapped particles. When the tangential force of the rotating fluid becomes dominant, a particle rolls down from the polymer film.

The rolling force resulted the from viscous drag force due to the fluid flow. The equation of the viscous drag force of the fluid flow is presented as

$$F_D = 1.7009 \times 3\pi\eta d_P v_P$$

In this equation, F_D and d_P are the viscous drag force and diameter of the entrapped particles respectively. The constant 1.7009 is used to observe the effect of the surface on the drag force [81]. In the Cartesian co-ordinate the balance of the forces of the entrapped particles are presented here

$$\sum F_x = ma_x = -\left(\frac{6\pi\eta r_P^2 v_{Px}}{x}\right)\int_{\beta_1}^{\beta_2} cos\beta d\beta - 2\pi T r_p \sin(\alpha) + 1.7009 \times 3\pi\eta d_P v_{Px}$$

$$\sum F_y = ma_y = 1.7009 \times 3\pi\eta d_P v_{fy}\rho_p$$

$$\sum F_z = ma_z = 1.7009 \times 3\pi\eta d_P v_{Pz} + (\rho_p - \rho)V_p g - \rho_p V_p g$$

In figure 9 (a), the balance of forces is illustrated, where the gravity force of the particles is countered by a combination of the buoyancy force and a component of the adhesion force. When the gravity force outweighs the combined balancing forces, the particle will slide downward under the influence of gravity. In this scenario, the dominant force is the downward pull of gravity, causing the particle to move in a sliding motion. On the other hand, the rolling force exerted on the particles by the fluid flow is counterbalanced by the other component of the adhesion force. If this component of the adhesion force surpasses the rolling force, the particle will remain in its current location. However, if the rolling force exceeds this component of the adhesion force, the particle will roll down from its current position. This balance between the rolling force and the opposing component of the adhesion force determines whether the particle remains stationary or undergoes rolling motion.

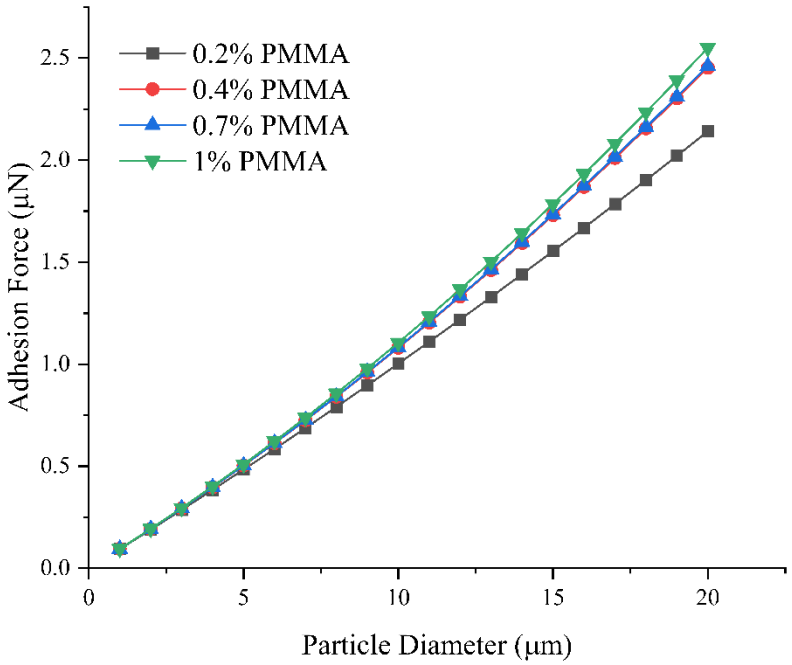

Figure 10: Variation of Adhesion force with the variation of particle diameter.

When particles come into contact with a polymer film on a substrate, the adhesion force exerted on the particles is a result of the combined influence of viscous fluid dynamic force and surface tension. The magnitude of this adhesion force is influenced by factors such as the size and shape of the particles, as well as the impact velocity. In our study, we investigated the relationship between adhesion force and particle size at a specific impact velocity, as depicted in figure 10. Our findings revealed a consistent and increasing trend in the adhesion force with increasing particle size. As the particle size increases, the contact area between the particles and the polymer film also increases. Consequently, the adhesion force experienced by the particles increases as well. This observation indicates that larger particles have a greater contact area with the polymer film, leading to enhanced adhesion forces.

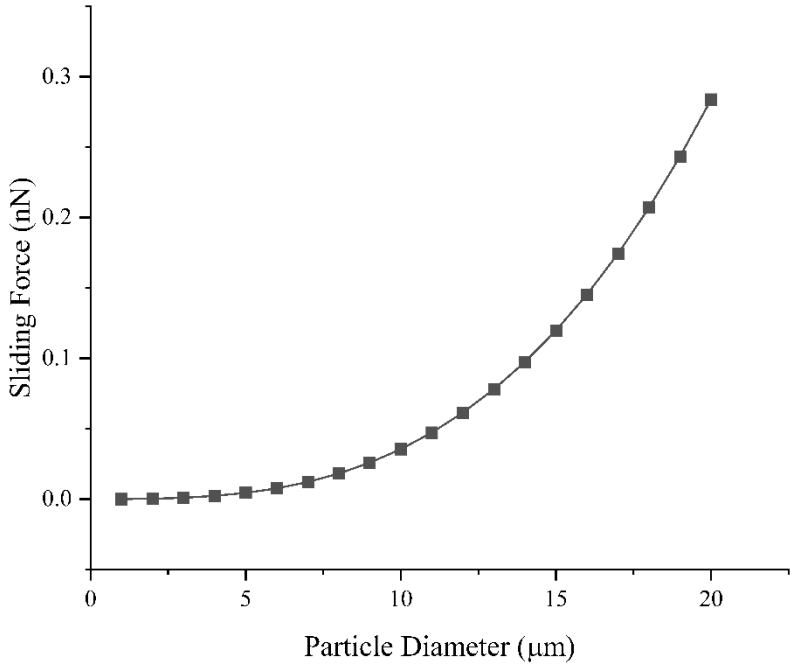

Figure 11: Variation of Sliding force with the variation of particle diameter.

The adhesion force acting on a particle plays a crucial role in keeping the particle in its current hitting location. However, there are several other forces that act in opposition, attempting to displace the particle from that location. One of these forces is the sliding force, which arises from the difference between the gravity and buoyancy forces. To examine the relationship between particle diameter and sliding force, we plotted the variation of sliding force as a function of particle diameter, as depicted in figure 11. The findings reveal that the sliding force acting on the particles increases as the particle diameter increases. Comparing the observations from figures 10 and 11, it becomes evident that the sliding force is relatively small compared to the adhesion force. However, this discrepancy in magnitude will be taken into consideration in our future work. Additionally, another force that contributes to the displacement of particles from their original location is the rolling force. This force is illustrated in figure 9(b) and will be further investigated as part of our research efforts.

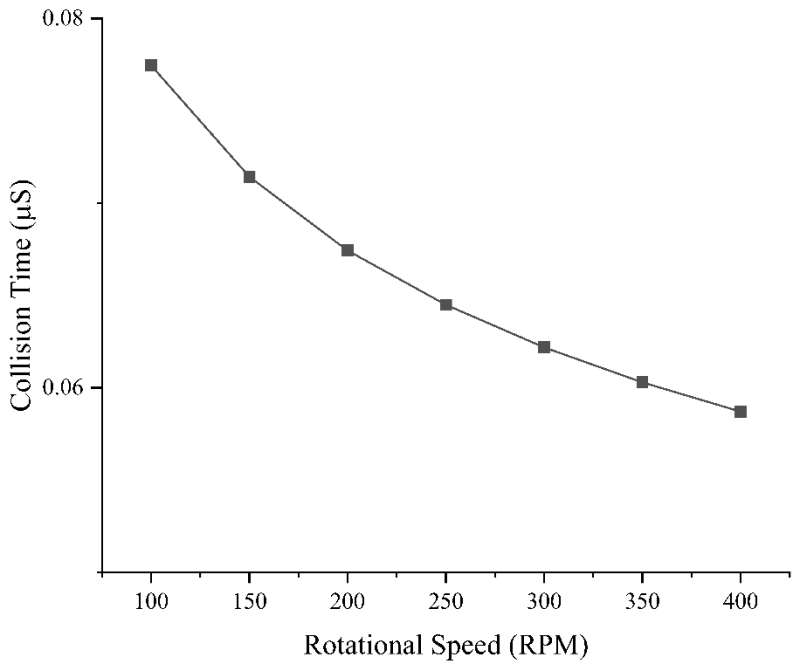

Figure 12: Variation of particle collision time with the rotational speed of the magnetic stirrer.

Another probability of particle hitting on substrate with viscous polymer thin film is rebounding from the substrate. When the particle's impact energy exceeds the adhesive force between the particle and the polymer film, the particle will rebound from the substrate. We conducted theoretical calculations to determine the duration of particle-substrate collisions. Our calculations employed the Hertzian model, known for its accurate prediction of collision timescales. The velocity of the particles in proximity to the substrate's wall was utilized to estimate the collision duration. This collisional duration can be expressed as follows [82]:

$$t_{Hertz} = 7.894\left(\frac{\rho_p^2}{E^{*2}V_{imp}}\right)^{0.2} r_p$$

$$\frac{1}{E^*} = \frac{1}{\pi}\left(\frac{1+\vartheta_P^2}{E_p} + \frac{1+\vartheta_w^2}{E_w}\right)$$

Here V_{imp}, E, and ϑ represents the impact velocity, young modulus, and Poisson ratio respectively. The subscript p and w correspond to the particle and wall respectively. For our study, we utilized Nicrabraz LM brazing particles and AISI 1006 MS rod as the wall material.

Interestingly, we observed that the collision duration of the particle decreases with an increase in the speed of the particles, specifically the rotational speed of the magnetic stirrer which is presented in figure 12. This reduction in collision duration can be attributed to the heightened hitting speed of the particles. When particles gain higher velocities, they acquire greater kinetic energy. This added energy enables them to overcome the resistance posed by the surrounding medium and move towards the wall more swiftly. As a result, the particles possess increased momentum, allowing them to cover the distance to the wall in a shorter period. The higher hitting speed of the particles leads to a reduced interaction time with the fluid or air in their vicinity. Consequently, the impact occurs more rapidly as the particles exhibit enhanced movement and traverse the space between their initial position and the wall more quickly. This observation highlights the relationship between hitting speed and collision duration, suggesting that higher velocities result in shorter interaction times during particle-wall collisions.

Effect of Rotational Speed on Particle Transfer

The rotational speed of the magnetic stirrer drives the kinetic energy of the particles, while the entrapment of particles is determined by their kinetic energy. This energy is transferred to the Liquid Carrier System (LCS), which transports the particles to the substrate. As the particles approach the substrate, an equilibrium is established between the viscous resistance of the organic polymer film and the kinetic energy of the inorganic solid particles, as discussed in the previous section. If the radial force of the particle is dominant, it will be entrapped into the polymer film; otherwise, the viscous resistive force will push it back. After the particle is entrapped, the surface

tension force of the polymer film activates, holding the particle in place. This force depends directly on the contact radius of the polymer film and the entrapped particles. There are two opposing forces that act to remove the particles from their site: the tangential force of the rotating fluid and the gravitational force of the particles.

Increasing the rotational speed of the magnetic stirrer results in higher kinetic energy in the particles of the suspension, leading to an increase in the radial force and contact radius between the particles and the polymer film. At low rotation regimes (up to 200 rpm), the particle transfer is enhanced due to the increase in kinetic energy. For instance, in figure 1 and 3, the maximum particle coverage and particle counts are 13.28% and ≈2789, respectively, for low rotation regimes. The maximum particle transfer occurs at a minimum suspending speed of 250 rpm due to the homogeneous nature of the suspension, which increases the probability of contact between the suspended particles and polymer film over the rod. At this speed, the equilibrium between the viscous force and radial force, along with minimal contribution of tangential force, helps to achieve maximum particle transfer. However, due to the higher kinetic energy of the particles at higher rotation regimes, particle transfer through entrapment is reduced after the minimum suspending speed (up to 350 rpm). Surprisingly, particle transfer increased at 400 rpm (as observed in figure 1 and 3), which is contrary to what was expected. At very high rotational speeds (400 rpm), a turbulent flow regime is observed in the suspension, creating a chaotic condition. Perhaps, due to this turbulent condition, the hitting probability increases, and at high binder concentrations (0.4% to 1% binder concentration), particle transfer increases.

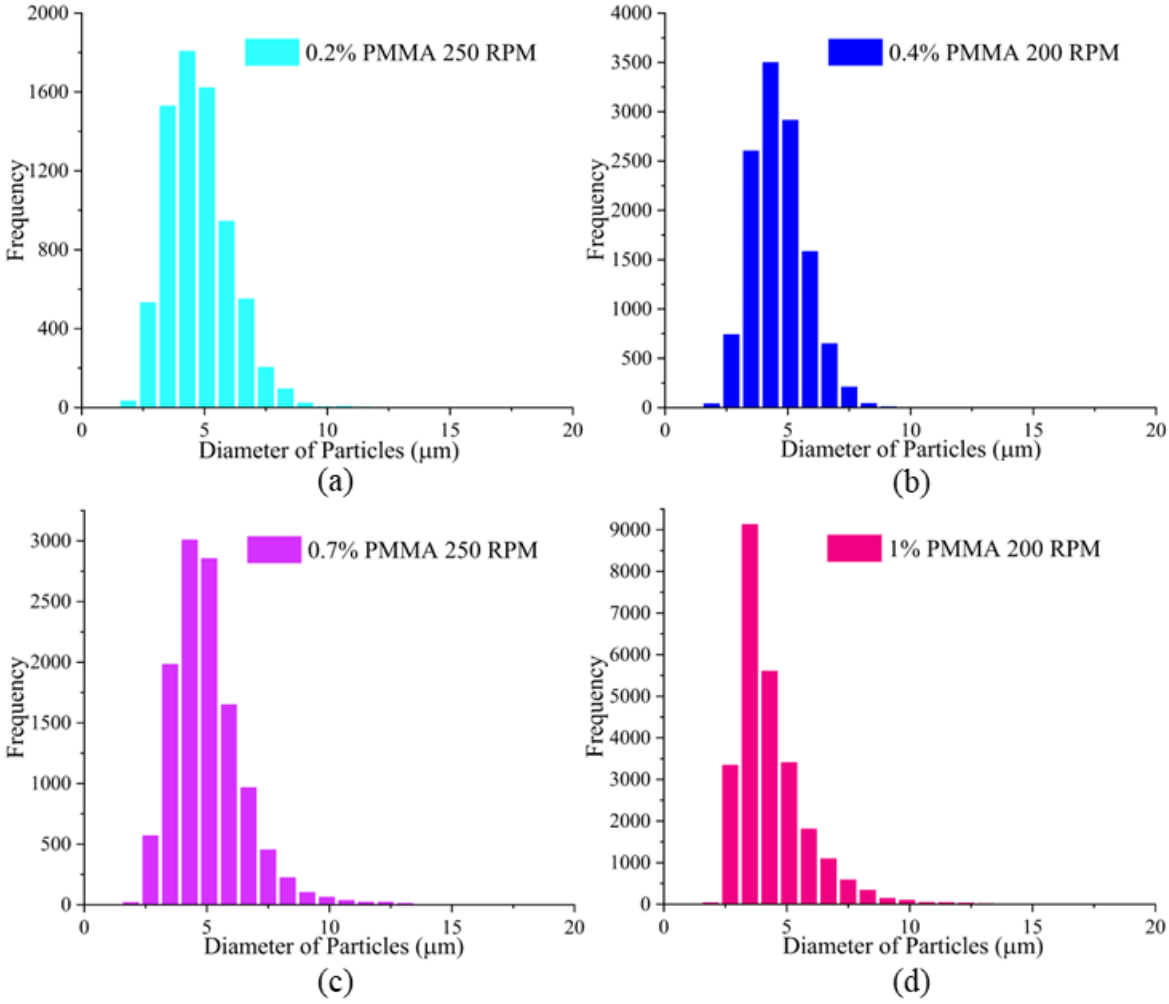

Figure 13: Variation of the particle size entrapped particle distribution with binder concentrations at 250 rpm rotational speed. 0.2% binder concentration (a), 0.4% binder concentration (b), 0.7% binder concentration (c), 1% binder concentration (d).

Effect of Binder Concentration on Particle Transfer

The viscosity of the suspension can be controlled by controlling the concentration of both the binder and particles. In this study, the particle concentration is kept constant (ϕ_p =10%) and the viscosity is varied by the variation of the binder concentration. The viscosity of the suspension is calculated using Krieger dougherty equation [48] which is presented in table 4. When the substrate is submerged in the suspension, a thin layer of polymer adsorbs onto its surface, and the thickness

of this layer is influenced by the binder concentration. A thicker polymer layer is formed at higher binder concentrations, as previously reported and compared with theoretical predictions [13]. The thicker polymer film enhances the binding strength of the inorganic particles.

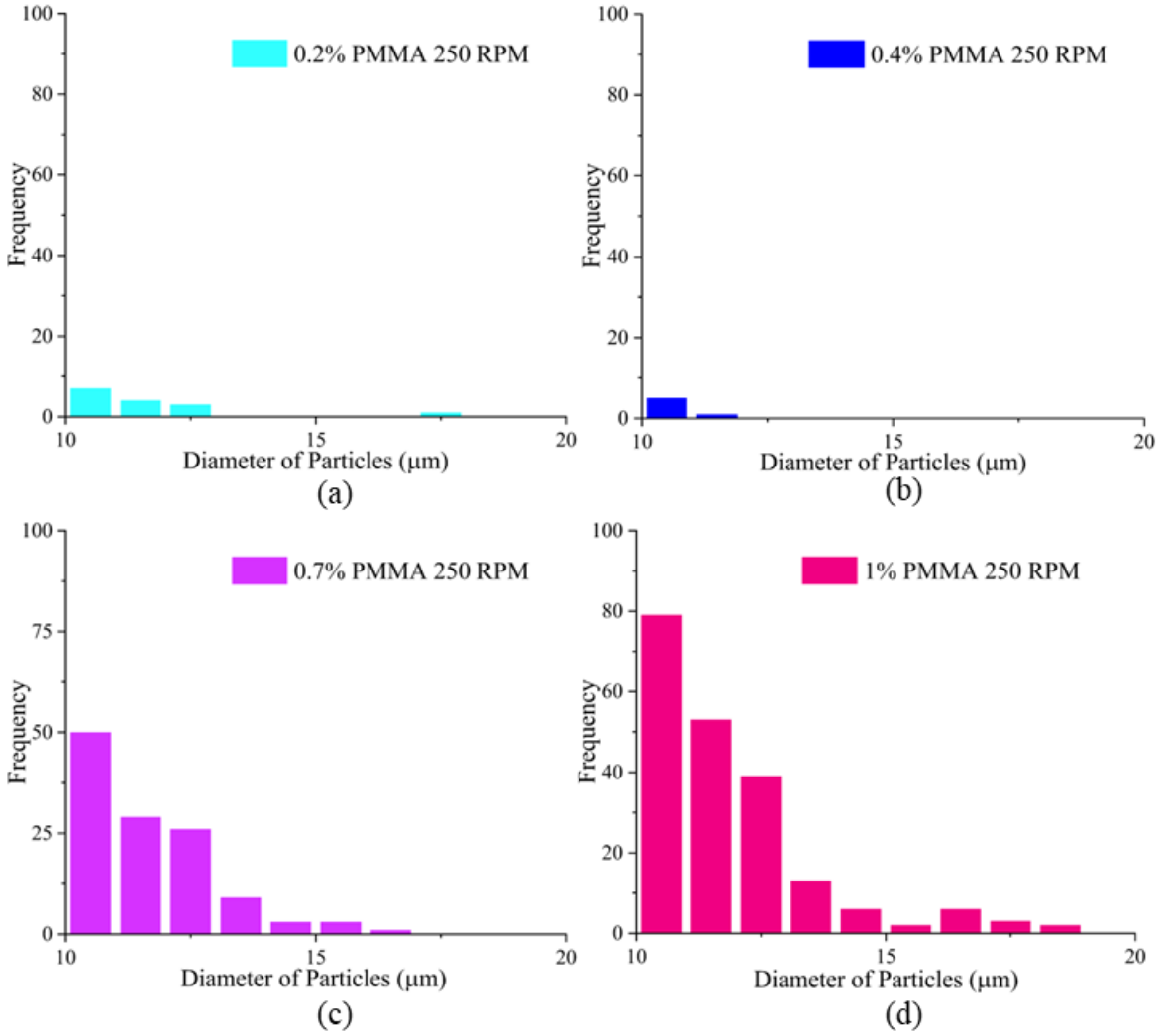

Figure 14: Distribution of the entrapped particles ≥ 10µm. 0.2% binder concentration (a), 0.4% binder concentration (b), 0.7% binder concentration (c), 1% binder concentration (d).

Figure 13 depicts the distribution of entrapped particles at various concentrations of binder, revealing a systematic trend. The particle counts varied with changes in binder concentrations in the suspension. The minimum number of entrapped particles (approximately 7368) was observed

when using 0.2% binder, while the maximum number of particles (approximately 18511) was observed at the highest binder concentration (1%) in the suspension. Interestingly, contrary to our prediction, the particle count was higher in the case of 0.4% binder concentration due to entrapment of similarly sized smaller particles in the polymer film, compared to the particle count at 0.7% binder concentration. All particle count calculations were based on a total image area of 1.195 mm2. By varying the binder concentration, we can control the viscosity of the suspension. As the adsorbed polymer layer thickness increases with the viscosity of the suspension, the maximum size of the entrapped particles also increases at high rotational regimes (after 200 rpm) which is presented in figure 4. For example, at 300 rpm, the maximum size of the entrapped particle is 14.88 ± 1.67 μm at 0.7% binder concentration (1.04 mPa.S) and 18.46 ± 1.03 μm at 1% binder concentration (1.24 mPa.S), which represents a significant increase in the maximum entrapped particle size. Figure 14 illustrates the distribution of larger particles (≥ 10 μm) at different binder concentrations. Notably, there is a significant increase in the number of larger particles entrapped in the polymer film at higher binder concentrations (0.7% and 1%) in the suspension. Thus, controlling the binder concentration can lead to size-based separation of the poly-disperse particle mixture. However, we observed no effect of binder concentration and rotational speed on the minimum size of the entrapped particles (as presented in figure 5). Smaller sized particles require low kinetic and binding energy to entrap them into the thin polymer film, which keeps the minimum size of the entrapped particles constant.

Concluding Remarks

In this study, we examined two process parameters of a novel particle transfer technique called entrapment: kinetic energy of the impacting particle and binder concentration. High-density solid micro particles were utilized with organic polymer as the binder, which was varied at different

concentrations. The magnetic stirrer provided kinetic energy to the particles, and particle transfer during entrapment depended on the competition between the particle's kinetic energy and the viscous strength of the polymer film. A systematic increase in particle transfer was observed as the kinetic energy of the particles increased until the minimum suspending speed ($\leq$ 250 rpm) was reached for that particle. The minimum suspending speed was characterized by the maximum particle transfer during the entrapment process. Particle transfer decreased at higher rotational speeds due to the particles' increased kinetic energy. However, a sudden increase in particle transfer was observed at 400 rpm due to turbulence generated in rotational flow.

Additionally, we observed the impact of binder concentration on particle transfer, as it directly affects the suspension's viscosity, which contributes to polymer layer formation. The maximum size of the entrapped particle increases with binder concentration, resulting in size-based separation of poly-disperse particle mixtures. We also noted a systematic variation in particle transfer with increasing binder concentration at a specific rotational speed. However, we observed small-sized almost monodisperse particles entrapping into the polymer film at 4% binder concentration, resulting in a decrease in maximum particle size and an increase in particle counts.

CHAPTER 3

SORTING OF POLY-DISPERSE PARTICLE BY ENTRAPMENT USING LIQUID CARRIER SYSTEM

Abstract

A thin viscous layer is found over a substrate when it is immersed in a polymer solution. The layer thickness depends on the polymer and solvent type, their volume fraction, and the substrate. If the liquid solution contains particles, they are entrapped in the viscous polymer layer, acting as the binder. The trade-off between the viscous force and the centrifugal force on the particle determines the entrapment. Furthermore, the size of entrained particles is dictated by the binder concentration of the solution., A particle filtration technique is presented using the entrapment phenomenon from a poly-disperse mixture. A dimensionless number called the entrapment factor is introduced to correlate the particle entrapment with various parameters. By changing the entrapment factor, three distinct entrapment regimes are achieved and explained from a poly-disperse mixture. The experimental result shows that entrapped particles become larger as the factor increases, which can be controlled with multiple parameters of the dipping process. The proposed technique can lead to a filtration process of the wide-range poly-disperse particle mixture over the capillary filtration processes.

Keywords: sorting, poly-disperse particle, inorganic micro-particle, entrapment factor.

Introduction

The gravitational force has a negligible effect on sub-micron particles, which are often adhered to the solid substrate almost effortlessly [1]. This is due to the adhesion force between the particle and the substrate, which can result from one or more of the attraction forces (i.e., van der Waals and electrostatic forces [2], covalent and acid-base interactions [3] or surface asperities [4]).

However, when the gravitational force becomes prominent, a binder is required to attach the particle to the substrate. Both micro and nanoparticles are carried toward the receiver substrate using the carrier media (i.e., gas, solid or liquid) and particles are transferred following the force balance equilibrium (interfacial entropy). For example, color pigment (metal oxide) travels through the gas are deposited on the substrate in the dry printing process [83]. Similarly, in the contact-transfer printing process, donor substrate (often elastomeric stamp) carries the particle and transfer them to the receiver substrate upon contact [84]. In the wet deposition technique, particles are added to the liquid, which carries and delivers the particles to the desired site using transfer processes such as Langmuir-Blodgett [22], dip coating, and spin-coating [23]. The resultant liquid carrier system (LCS) can be of various forms, i.e., solution, sol-gels [85, 86], colloids [87], slurry, suspension [30, 31], or heterogeneous mixture. Common transferrable are either organic (polymer chain from the solution) or inorganic nanoparticles (ceramics or metal oxides). Among all the wet deposition techniques, evaporation-based dip coating or dipping lacquers is the simplest, facile to scale up, low-cost, waste-free, low energy consumption [24]. It is suitable for large surface film generation [1, 88, 89] on complex structures, including porous architecture (low volumetric flux). A plethora of work has been reported on wet deposition-based dip-coating, and many of them are focused on material transfer from suspension (direct transfer) or from precursor chemicals (ionic transfer). It allows a wide range of density and viscosity of the liquid carrier system for the preparation of thin layers over flat and circular substrates [90]. Material is transferred on the interfacial substrate while withdrawing from a mixture or solution (entrainment) [25, 91]. The competition between the capillary force and the viscous drag force at the time of the withdrawal determines the thickness of the polymer layer on the substrate [26]. The thickness is also influenced by the withdrawal speed, shape, and physical properties of the substrate [1]. In one of the

pioneering works of the dip-coating process, the thickness of the film is determined by $h = 0.94 l_c Ca^{2/3}$ which is known as famous LLD equation [27, 28]. Here $l_c = \sqrt{\gamma/\rho g}$ is the capillary length, $Ca = \eta U/\gamma$ is the capillary number and γ and η are the surface tension and the viscosity of the suspension respectively; *U* is the withdrawal speed of the substrate and *g* is the acceleration with respect to gravity.

The thin-film generation technique is commonly used in various industrial applications, including corrosion protective layer [6, 7], roller lubrication process, printing technologies, medical application [92, 93], modification of cutting tools [5] and wire coating [8, 9], biosensors [43], and hybrid coating [94], etc. In recent works, the dip-coating process demonstrates the size-based separation of particles from the suspensions [33, 95, 96] by tailoring capillary force and the viscous drag force at the liquid-gas interface. The polymer layer governs particle entrainment during withdrawal onto the substrate, which changes with the withdrawal speed of the substrate from the suspension and the percentage of the binder in the solution. Silicone oil is used as the liquid carrier system to carry the neutrally buoyant polystyrene micro-beads particles (20 µm-250 µm) in their studies. Three regions are reported after withdrawal which are explained with capillary number (*Ca*); no particle entrainment for low *Ca* regime; cluster of micron size particle entrainment at medium *Ca* regime and individual large particles are entrained at high *Ca* regime.

Larger inorganic micro-scale particles are commonly used in manufacturing industries (e.g., brazing powder, metal filler, and 3D printing powder). Common powder particle manufacturing processes include gas atomization, plasma atomization, and plasma rotating electrode process. These processes are commonly known as droplet-based particle fabrication techniques and generate a spherical particle size distribution with a large standard deviation (poly-disperse). The size distribution often follows a continuous exponential pattern commonly expressed with rosin-

rammler expression [97]. A narrow particle size range is an essential trait for their utilization in various manufacturing domains (i.e., additive manufacturing [35-37], powder sintering, metal injection molding, powder bed fusion, etc. [98]). Mono-disperse particle fabrication is difficult, costly, and challenging [99] and oversized particles are very common. Different filtration processes are employed to reduce the poly-dispersity as post-processing steps, including membranes [100-102] or motion of the bubble [103]. However, their size separation capacity can be limited and can become energy intensive. Capillary filtration via dip coating is relatively a facile process and has been demonstrated in separating the bi-disperse particles [95] from density matching dilute suspensions. However, the inorganic-micro particle has a higher density and will generate slurries than the solution if added to LCS. Thus, capillary filtration may not be a viable option. The particle transfer mechanism using the dip-coating process is rarely investigated with density mismatching heterogeneous mixture.

In this work, we are reporting a poly-disperse particle filtration technique from density mismatching heterogeneous mixture at the solid-liquid interface (submerged condition). The novelty of this work is to investigate particle entrapment rather than entrainment, which is the deviation from the *status quo*. When a substrate is dipped in a polymer solution, a thin viscous layer is formed due to fundamental molecular interactions leading to reversible or irreversible adsorption [46] layer. The adsorbed layer consists of (i) interphase metal and oxide, (ii) interface, and (iii) interphase polymer. The thickness of this adsorbed layer can range from a few nanometers to a couple of micrometers, which is the driving force for particle entrapment. By controlling the process parameters, the adsorbed layer can entrap inorganic nano to micro-particles in the presence of a relative motion. The particle entrainment and the boundary layer formation during withdrawal

are shown in Figure 15(a). In contrast, the particle entrapment on the substrate in the submerged condition is shown in Figure 15(b), which is the focus of this paper.

Methodology

The liquid carrier system used in the experiments consists of solute (binder) and solvent (1, 3-Dioxolane) to deliver solid brazing (Nicrobraz 51) particles. Poly-methyl methacrylate (PMMA) is used as the binder, and the chemical formula of the binder is $CH_2=C[CH_3]CO_2H$. The density of the binder and the solvent are 1.17 g/cm^3 and 1.06 g/cm^{3,} respectively at room temperature (RT = 25°C). Both solute (granular) and solvent (liquid) are procured from Sigma Aldrich, USA. A magnetic stirrer is used for two hours at RT to dissolve the solute into the solvent. Table 1 shows the viscosity of the solution at different binder percentages, as measured with an Anton Paar MCR 302 Rheometer with a parallel plate/plate geometry. The binder concentration varies at different intervals ranging from 1% to 13% for the sorting of the particles within the range of particles used in the mixture. All viscosity measurements are taken at RT.

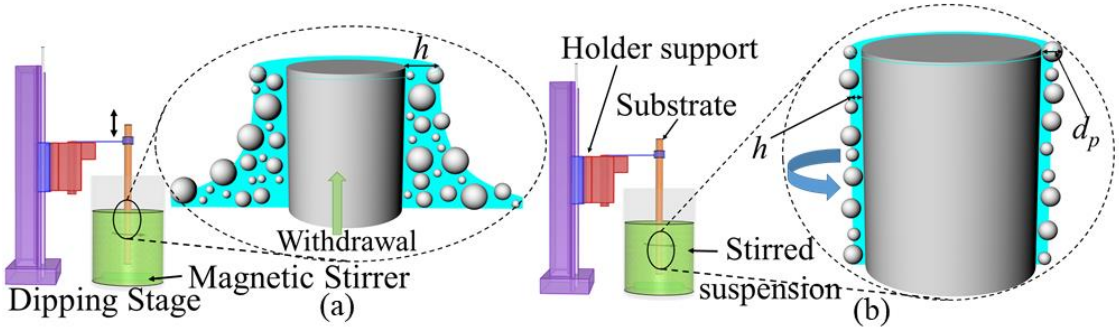

Figure 15: Schematic diagram of particles transfers into the thin layer over the substrate (not to scale): (a) particle entrainment at the time of withdrawal of the substrate is shown and (b) particle entrapment to the substrate in the submerged condition.

Brazing powder (Nicrobraz 51; Wall Colmonoy company, Ohio; Spherical dia range ~0-100 µm) is sieved with Gilson Performer III shaker through Stainless Steel 635 Mesh (20 µm) in our lab to

reduce polydispersity and are analyzed using SEM. The average diameter of the particles is found 5.69 μm. For submicron size particles, the electrostatic force and van der Waals forces become prominent for coagulation due to their possession of a large specific surface. However, for larger particles (>1μm) the specific surface area is reduced, which makes them non-interacting and non-agglomerating spherical solid particles in the liquid matrix (non-Brownian regime) [104, 105]. Thus, no dispersant is needed here. The density of the particles is 7.8 g/cm^3, and the particle to liquid density ratio >7. Due to this density mismatching, fast sedimentation will occur, which will accumulate at the bottom of the dipping vessel and create a phase separation. The external kinetic energy in the form of agitation is applied in the mixing reactor to encounter the gravitational force. A cylindrical magnetic stirrer is used; the stirrer's length and diameter are 14.88 mm and 5.95 mm. The stirring will create a pressure difference (normal stresses), and the particles will lift off and stay suspended, creating a dispersed mixture (‘pseudo suspension’).

In this study, the substrate is a cylindrical AISI 1006 mild steel rod with an average diameter of 1.1 mm (procured from ClampTite LLC). Rod samples are cleaned in the ultrasound bath with acetone for 10 minutes at 50 ºC, which will remove any surface contaminant and passive film. Before dipping, the mixture is stirred for 15 minutes at a rotation of 150 rpm for stabilizing. The dipping reactor used in this experiment is a 20 mL 95020-0CV Vials, screw top; clear borosilicate glass, round bottom with the dimension of 75.5 x 22.5mm. The rod is mounted on the Z-axis stage controlled with a Flashcut CNC controller. A high-precision bipolar stepper motor (SANYO) connected with a computer will be used to control the dipping speed within ±2% precision, which is controlled using G-code.

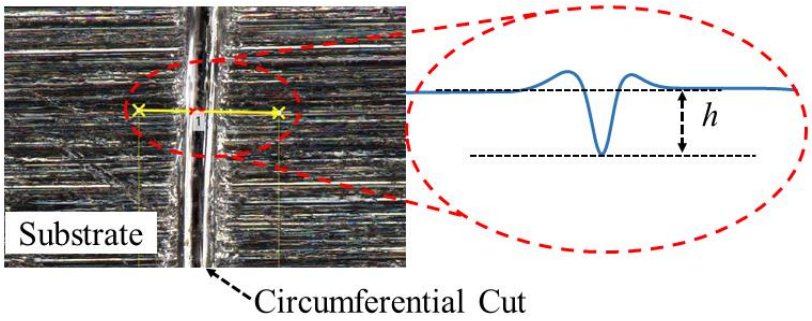

Figure 16: Experimental measurement of the polymer layer thickness with a round cut.

The rod entered the center of the dipping reactor at a speed of 10 mm/s during the experiment. The dwelling time is a total of 90 minutes. Stirring continues for the first fifty minutes, and then the stirrer is switched off. The mixture settled down in the remaining 40 minutes creating the phase-separated mixture. This ensures that no particles are floating in the mixture to entrain the substrate while withdrawing. Afterward, the substrate is withdrawn from the particle-laden mixture very slowly at 0.1 mm/s to minimize any vibration. The solvent evaporates quickly from the substrate leaving the transparent binder and the entrapped particles. The liquid film thickness is measured with 3D profile depth variation using VHX 7000 Digital 4K microscope (KEYENCE corp., IL) at 1500X. A narrow groove is created with a round edge cut on the substrate in three different locations. The profile depth is measured and averaged as shown in Figure 16. The high-resolution 4K images of the dipped rod are analyzed with image J software. To ensure statistical significance, ten samples (regions) are randomly selected for each measurement (i.e., particle count, surface coverage) in each sample which is then averaged for further calculation in this paper. While plotting the experimental values, the standard error is calculated for the error bar and 2σ (95.45% confidence level) bar is used in the plotted data to demonstrate the repeatability.

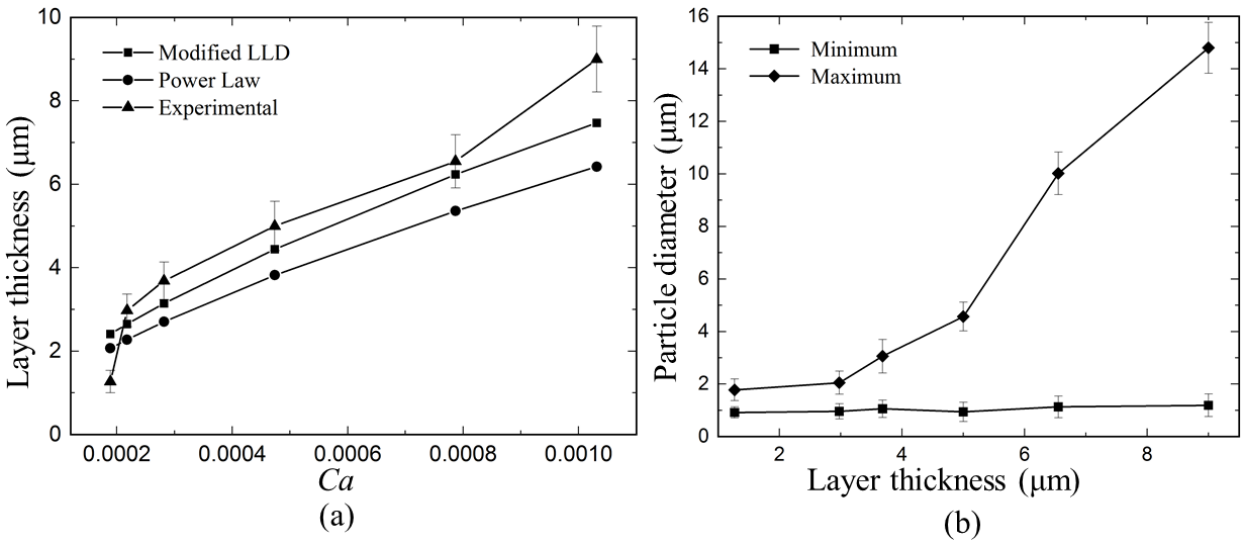

Figure 17: (a) Comparison of theoretical and experimental polymer layer thickness with the capillary number (both circle and squares are the theoretical results and triangle indicate the experimental results) (b) The variation of the entrapped particle size with the variation of polymer layer thickness observed from the experiment.

The volume fraction of the particles is measured by the ratio of the volume of particles and the total volume of the mixture (solute, solvent, and particles) as $\phi_p = V_p/(V_p + V_{solute} + V_{solvent})$; here V_p is the volume of particles. The volume fraction of the particles is kept constant (ϕ_p= 10%) for our the experiments as the previous studies have found that the mixture with $\phi_p < 20\%$ remains in the Newtonian regime at a low share rate, $\dot{\gamma}$ [106]. Only the binder percentage is varied to observe the entrapment phenomenon. The viscosity of the suspension is measured by using the Krieger-Dougherty equation [48] using the viscosity of the solution $\eta_\phi = \eta_0(1 - \phi/\phi_{max})^{-B\phi_{max}}$; here ϕ_{max} is the maximum volume fraction of the particles and *B* is the Einstein coefficient. Packing for monodisperse sub-micron spherical particles (ϕ_{max}) can range from 0.52 to 0.74 with some staking scheme. However, their random close packing (RCP) density is about 0.64 [107], which may increase up to ~0.74 for poly-disperse particles [74, 108]. For the rigid

sphere under sheared suspensions, the maximum particle volume fraction is reported as ϕ_{max} = 0.68 [109] and ϕ_{max} = 0.67 [88]. The value of B is used as 2.5 [29] to calculate the viscosity of the suspension is listed in table 2.

Result and Discussion

In the classical dip-coating process, particle entrainment to the substrate is due to the competition between the viscous force and the capillary force during the withdrawal of the substrate [25, 110]. To verify the present experimental model, the substrate is dipped into the solution without the particles and stirring energy. To minimize the convective flux (entrainment of polymer chain) during withdrawal, a very low withdrawal speed (0.001 mm/s) is used, for which the film thickness is measured using the methodology discussed in the previous section. To compare the experimental result of this system, the polymer layer thickness is also determined with the modified LLD [1] equation ($h_{LLD} = 1.34 r_f Ca^{2/3}$) and power-law equation ($h_{power} = \frac{1.34 r_f Ca^{2/3}}{1+2.53Go^{1.85}/[1+1.79Go^{0.85}]}$) [96]. Here r_f is the radius of the fiber; Go is the Goucher number and expressed as $Go = r_f/l_c$; l_c is the capillary length. The data are plotted in Figure 17(a), which shows the experimental thickness is slightly higher than the theoretical value. This variation can be attributed to the very low withdrawal speed (0.001 mm/s) [111] during this experiment. In addition, the size of the entrapped particle and their variation is shown with the entrained polymer layer thickness in Figure 17(b). The size of the maximum entrapped particles increases with the polymer layer; however, the maximum particle size increases sharply when the polymer layer thickness $\geq 5\ \mu m$.

Table 3: Parameters of Experiment and the physical properties of the solution

Binder (%)	**Velocity of particle (m/s)**	**Particle volume fraction (%)**	**Viscosity of the solution (mPa.s)**	**Density of the solution (g/cm^3)**	**Surface Tension (mJ/m^2)**
1	8.64×10^{-3}	10	0.752	1.037	34.374
2	8.64×10^{-3}	10	0.868	1.038	34.449
4	8.64×10^{-3}	10	1.128	1.042	34.598
7	8.64×10^{-3}	10	1.908	1.047	34.821
10	8.64×10^{-3}	10	3.191	1.052	35.044
13	8.64×10^{-3}	10	4.210	1.057	35.268

The particles are entrapped into the thin layer that is due to the relative motion of the substrate and suspension, as shown in Figure 18. As the stirring speed is low, it assumes minimum slippage, like laminar flow. Moreover, the length of the stirrer is close to the diameter of the dipping reactor. Thus, the radial speed of the mixture near the substrate can be assumed steady. Similarly, the speed variation in particles along the vertical direction can also be neglected in this experiment [52]. The rotational speed of the particles can be assumed as the same as the stirrer speed ($\pi dN/60$, where d is the rotation diameter of the particles and N is the RPM) near the substrate.

When the substrate is dipped into the solution, a polymer layer is adsorbed on the substrate (polymer film as shown in Figure 18(b)), and the thickness of the polymer layer is dependent on the binder concentration. As the particle comes closer to the substrate, the viscous polymer film will entrap the particle with the viscous force, while the centrifugal force acting on the particle will push it to roll and drive them towards the bulk. The balance between these two forces will cause the entrapment of the particle on the substrate, for which the mechanism is shown in Figure 18. The experimental parameters and the physical properties of the solution are listed in table 1. As discussed in the methodology section, the entrapped particle size and their coverage on the substrate are measured from the microscope image analyzed by ImageJ software. The size

variation of the entrapped particles is shown in Figure 19 with schematic and actual microscope images. The results of the experiments are divided into three different zones (Zone A, B and C) based on the particle sizes entrapped into the polymer layer on the substrate. From the image (Figure 19), a positive correlation between entrapped particle size and the binder volume fraction can be observed, for which the quantitative data are presented in Table 2. Such a correlation can be used for the batch-wise filtration of the poly-disperse particles.

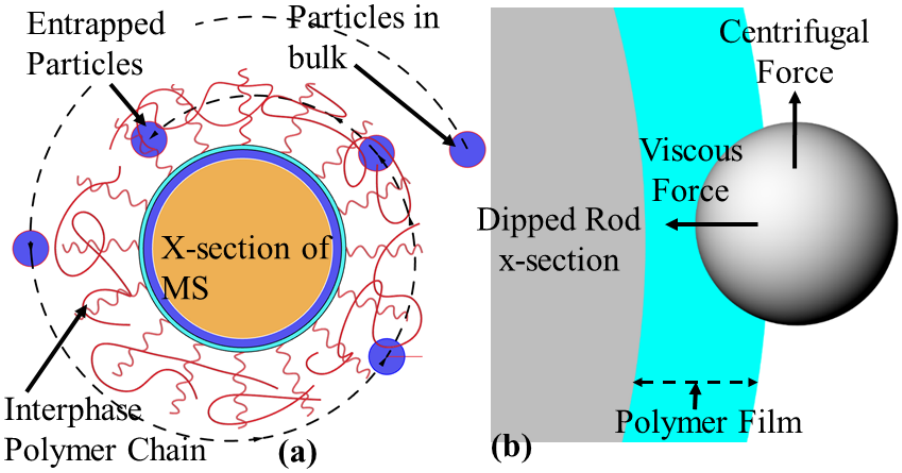

Figure 18: Particle entrapment mechanism in the vicious layer at submerged condition (a) particle entrapped in polymer chain (b) acting forces.

For further investigation of this phenomenon, a parametric relationship needs to be established. The traditional dip-coating process uses dimensionless numbers (e.g., Capillary number or Bond Number) that consider the dipping parameter, substrate, and mixture characteristics. Such dimensionless numbers work well for entrainment in the solid-liquid-gas interface [112], which can predict the properties of the entrained film. However, the particles are entrapped into the thin polymer by the relative motion, similar to the collision of particles through media in cold spray coating [113]. As the particle is entrapped in the submerged condition in the solid-liquid interface, and the Capillary number ($Ca = \eta U/\gamma$) and Bond Number ($Bo = (d_p/2l_c)^2$) are not appropriate.

Moreover, the substrate is motionless in the submerged condition during the entrapment of particles, that is why the capillary number is not suitable to explain the entrapment phenomenon.

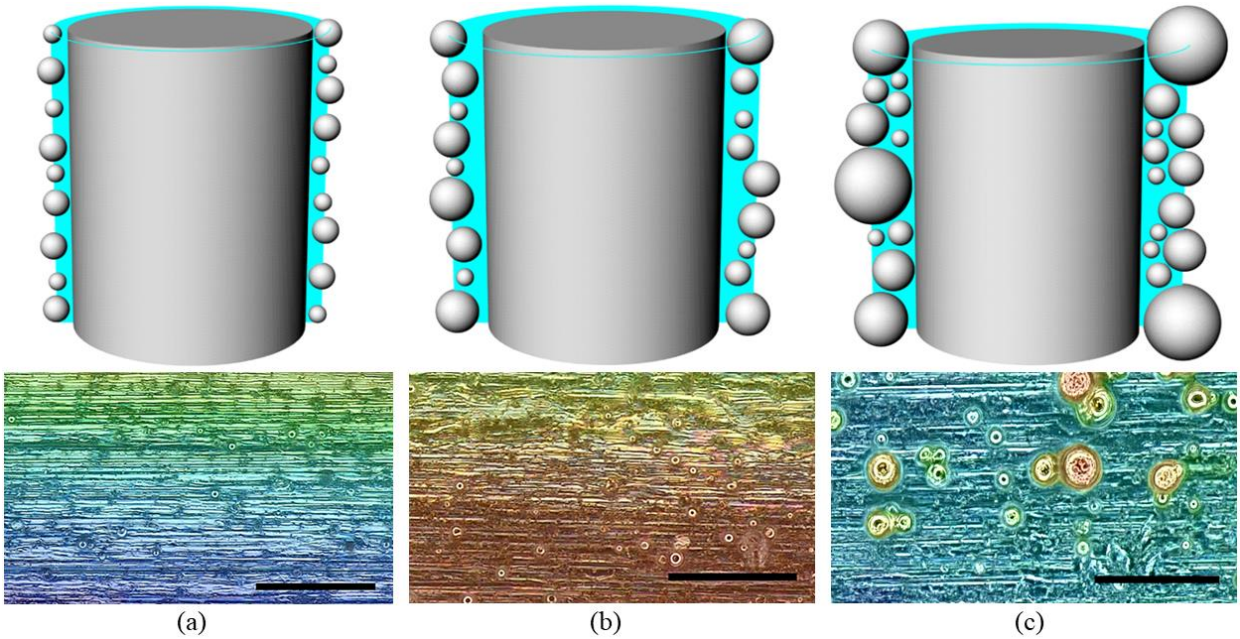

Figure 19: Visualization of particle entrapment at binder percentage schematic in the upper side and experimental in the lower side (a) Zone-A, (b) Zone-B, (c) Zone-C. 20µm scale bar.

A new non-dimensional factor is introduced to correlate the variation of the entrapped particle size in the polymer layer. In submerged conditions, the entrapment of the particles depends on the competition between the viscous force, F_V and the centrifugal force, F_C acting on the particles. The viscous force can be defined as $F_V = 1.7009 \times 3\pi\eta d_P v_P$; η, d_P and v_P are the viscosity of the suspension, the average diameter of the particle, and the velocity of the particle, respectively; whereas, the centrifugal force can be expressed as $F_C = \rho V v_p^2/r$; $\rho, V,$ and r are the density, average volume of the particles, and rotational radius of the particles, respectively.

Table 4: Variation of Particle size and coverage with Binder concentration.

Percentage of Binder	Viscosity of the suspension (Pa.s)	Surface Coverage (%)	Average Particle Diameter (µm)	Maximum Particle Diameter (µm)	Minimum Particle Diameter (µm)	Range of particle diameter (µm)
1	9.86×10^{-4}	0.564	1.23	1.78	0.92	0.80
2	1.14×10^{-3}	0.993	1.37	2.05	0.96	1.09
4	1.48×10^{-3}	2.348	1.72	3.06	1.06	2.00
7	2.50×10^{-3}	2.937	2.13	4.57	0.94	3.63
10	4.19×10^{-3}	3.478	3.98	10.02	1.13	8.89
13	5.53×10^{-3}	5.673	5.66	14.80	1.19	13.61

Since the rod is dipped at the center, r is considered as the radius of the rod. The constant 1.7009 is used to observe the effect of surface on drag force [81]. The viscous force helps the particle remain in the polymer layer on the substrate; conversely, the centrifugal force drives the particles out of the polymer layer. Thus, the entrapment factor is defined here as the ratio of viscous force and the centrifugal force, which is calculated by the following equation.

$$\text{Entrapment Factor } (Ef) = \frac{\text{Viscous Force } (F_V)}{\text{Centrifugal Force } (F_C)} = \frac{1.7009 \times 3\pi\eta d_p r}{\rho V v_p}$$

The force variation acting on the particles is shown in Figure 20. As the particle distribution (mass) and rotational diameter remain fixed, the centrifugal force acting on the particles remains constant. The viscous force changes with LCS viscosity through the binder concentration. Increasing the stirring energy or decreasing the binder viscosity both will reduce the entrapment factor and hence the particle entrapment. However, in this work, the centrifugal force remains constant by keeping the same stirring RPM (150 RPM) which is close to the just suspended speed of the mixture. The increase in entrapment factor indicates a clear dependency of layer thickness and the size of entrapped particles. This entrapment factor helps us to compare the entrapment of different-sized

particles with the binder volume fraction. The variation of the entrapment factor with the concentration of the binder is presented in Figure 20.

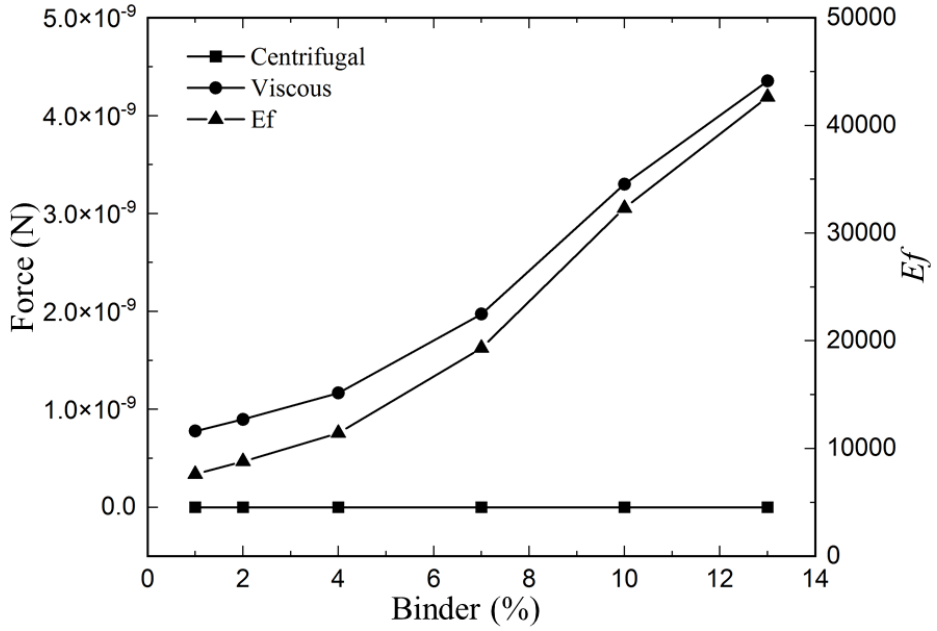

Figure 20: Variation of Force (viscous force is indicated by circle legend, square denoted the centrifugal force) over the particle and entrapment factor (shown by triangle) with the variation of binder percentage.

As the thickness of the polymer layer in the submerged condition depends on the viscosity of the dispersion [114], the viscous force increases with the entrapment factor, and hence larger particles are entrapped into the polymer layer. Figure 21 depicts the variation in entrapped particle size into the polymer layer as a function of the entrapment factor. For the particle separation analysis, three different zones are defined, which are shown as the yellow regions in Figure 21. The first zone is the small particle entrapment zone, which is Zone-A ($7.6\times10^3 < Ef < 8.8\times10^3$) where small particles ($0.92\ \mu m < d_{p,min} < 0.96\ \mu m$; $1.78\ \mu m < d_{p,max} < 2.05\ \mu m$) are entrapped into the polymer layer. Zone-B ($11.4\times10^3 < Ef < 19.3\times10^3$) contains particle size range of $0.94\ \mu m < d_{p,min} < 1.06\ \mu m$ and

3.06 μm < $d_{p,max}$ < 4.57 μm. Finally, entrapped particles range is 1.13 μm < $d_{p,min}$ < 1.19 μm and 10.02 μm < $d_{p,max}$ <14.8 μm in Zone-C ($32.3\times10^3 < Ef < 42.6\times10^3$). Moreover, the transition zones ($8.8\times10^3 < Ef < 11.4\times10^3$ and $19.3\times10^3 < Ef < 32.3\times10^3$ indicates the transition from Zone-A to Zone-B and Zone-B to Zone-C respectively) are shown as the light green region in Figure 21.

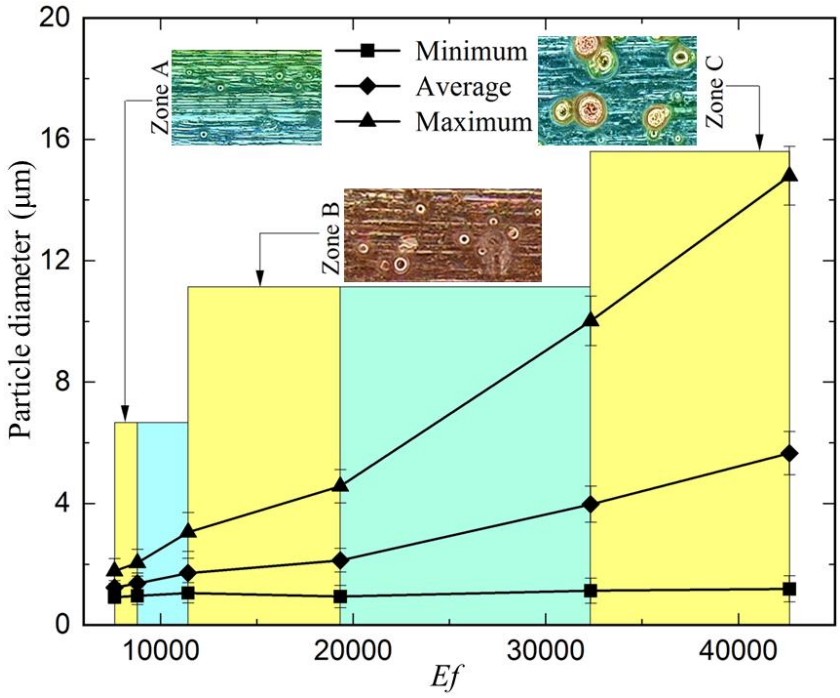

Figure 21: Variation of particle size with the variation of entrapment factor. Three zones are shown by the yellow region, and the transition from one zone to another zone is shown by the light green region.

To measure the effectiveness of the process, the sorted particles are counted, and diameter is measured for their distribution. Figure 22 represents the sorted particle distribution after dipping for each zone (Zone A, B and C). Compared to the bulk particle distribution, it can be observed that the particles with small diameters are only entrapped into the substrate in Zone-A. Similarly, clearly distinct particle distribution can be observed in Zone B and C as well. It can also be seen

that by increasing the entrapment factor, particle counts can be increased, and thus the efficiency of the process will depend upon the sorting range.

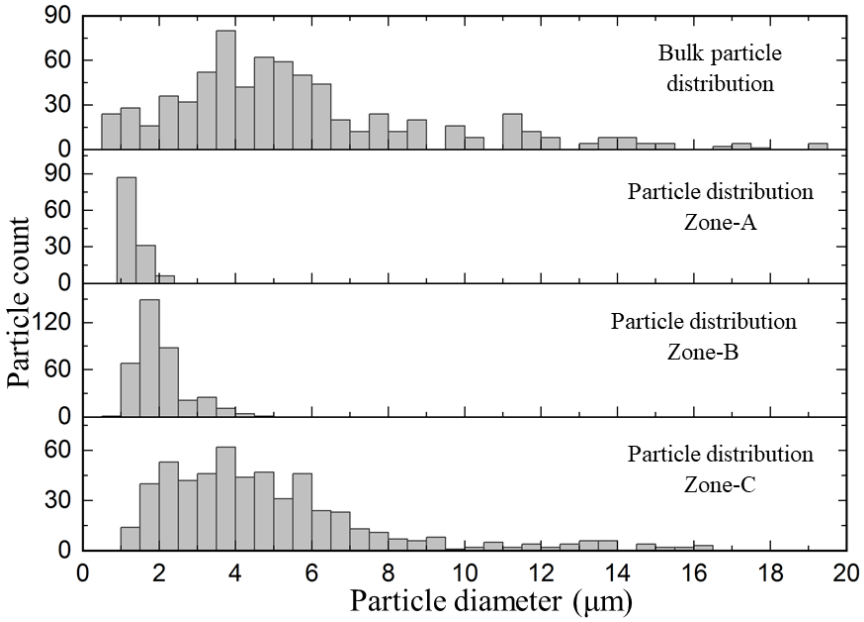

Figure 22: Particle distribution of different zones of filtration process. The scale of particle diameter is the same for all the graphs.

The minimum particle size entrapped in the three zones is almost similar; however, the maximum particle size entrained into the polymer layer increases with the increase of the entrapment factor. The maximum particle size increases rapidly when the value of the entrapment factor is greater than 20000. Successive filtration in Zone-A enables this process to separate the small particles (0.92 μm < d_p < 2.05 μm) from the suspension of poly-disperse particle mixture, leaving the medium and the large particles in the suspension. Larger particles (d_p >10.0 μm) are only left into the suspension when the binder volume fraction is increased (Zone-B). This unique process can repeat itself for the batch-wise separation of particles from both the bi-disperse and the poly-disperse particles mixture. To expedite the filtration process, a larger reactor and multiple

substrates can be used that will increase the transfer surface area. The entrapped particles can be removed by scraping from the substrate or by using the solvent to dissolve the binder.

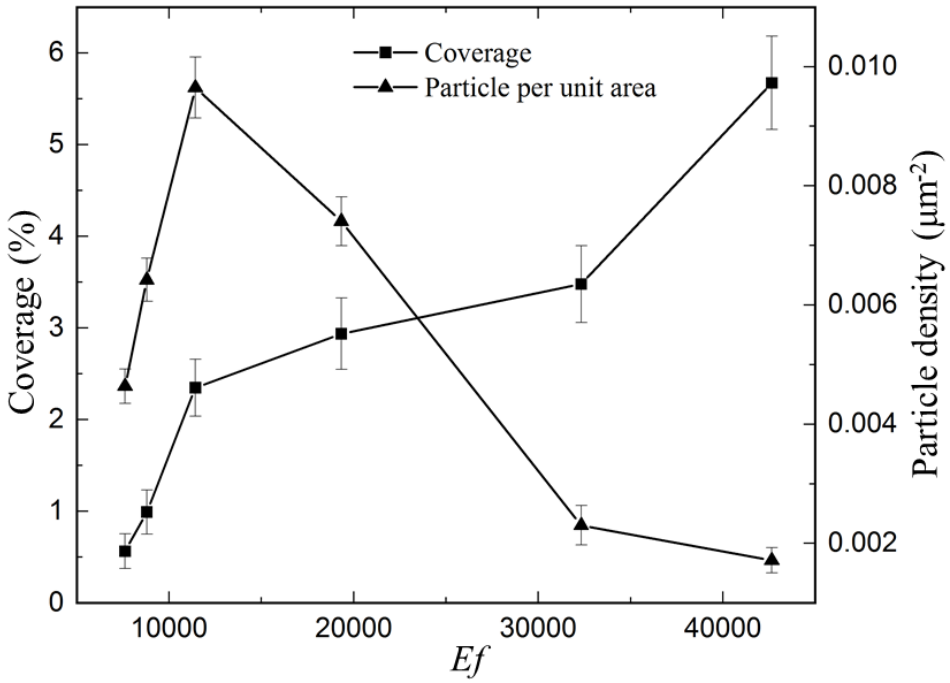

Figure 23: Variation of Coverage and Particle density with the variation of Entrapment Factor.

Two additional matrices, coverage, and particle density are measured in this work which is plotted in Figure 23. Ten randomly selected regions over the substrate are imaged, and particles and their diameters are counted using image J software. Coverage is calculated by taking the ratio of the covered and uncovered area after withdrawal by the entrapped particles. On the other hand, particle density is the number of particles per unit area, which is averaged from the ten samples collected for measurement. A higher coverage rate increase is observed at low and high *Ef* value in our experiment. At lower *Ef*, the coverage increases rapidly; however, no cluster formation is observed. With a higher *Ef* value, the entrapped particle size exceeds the cluster effect. The particle density increases till $Ef < 11500$ and, then starts to decrease. This is because larger particles are entrapped as the entrapment factor increases.

Conclusion

Particle-sorting or filtration works using the dip-coating process are based on the entrainment threshold of a wide range of particle size and working fluids [30, 115]. This work demonstrates the successful separation of the particles from a poly-disperse mixture with particle volume fraction (ϕ_p =10%) using the entrapment phenomenon. The density of the microparticles used in this work is almost eight times higher than the solution used, which is parameterized with the entrapment factor (EF). The particle entrapment occurred due to the viscous force at the time of particle rotation. The results of this experiment clearly show there are no clusters of particles at low binder concentration; however, some clusters of particles are observed at higher binder concentrations. The entrapment factor (EF) varies by varying the viscosity of the solution; however, the effect of the centrifugal force on particle entrapment will be the future work.

The filtration process mentioned in this work shows a promising way of separating hard inorganic dense ploy-disperse particles from density-mismatching suspension. Additionally, the process can be utilized for removing solid or soft impurities from suspension or mixture sediment [116]. As this sorting process is free from clogging (not like the membrane filtration), the process can also be successfully used for the separation of biological microorganisms and pollutants from the suspension. Simple control over particle size at the time of filtration using this method makes it more attractive for industrial and biological applications.

CHAPTER 4

SYSTEMATIC VARIATION OF FRICTION OF RODS

Abstract

The mechanical response of a knot tied in elastic rods strongly depends on the frictional force due to rod-rod contact. The behavior of a knot can be qualitatively different based on the frictional coefficient of the elastic rod. Systematic variation of friction during rod-rod contact is a crucial component of any experimental design to uncover the underlying ingredients behind the mechanics of knots. In this paper, we demonstrate a novel process of controlling the friction of a continuous rod by adhering non-spherical inorganic microparticles. A polymeric binder is used to deliver the particles as asperities over the rod substrate and by controlling their size and distribution the coefficient of friction of the rod are determined. In parallel, numerical simulations with the Discrete Elastic Rods algorithm are used to reproduce the experimental observations. Tabletop experiments are performed where overhand knots with a variety of unknotting numbers are pulled tight. The force-extension curve of these experiments shows that the proposed process can successfully tune the friction between rods.

Keywords: computational mechanics, elasticity, mechanical properties of materials.

Introduction

We use knots in ropes everyday for sailing, fishing, climbing, surgical procedures, and various industrial applications. The Ashley Book of Knots contains illustrations of more than 3800 different types of knots [117], each with a different topology. A knot almost invariably involves frictional contact between rods except in extremely rare cases [118]. In addition to the topology, the mechanical response of a knot is governed by the frictional coefficient of the contact [119]. Overall, the mechanics of a knot are the functions of its topology, friction, and material parameters.

This leads to a highly coupled system with fascinating mechanical behavior. Examples abound in our everyday life. When tying shoelace knots, mistakenly tying the “granny” knot instead of the “reef” knot can dramatically decrease its performance, i.e., the knot may get undone at a small amount of external force. Knots can even serve as a “topological battery” where a number of tangled rods remain tangled without any external force or boundary conditions and keep elastic strain energy stored within it [120].

Due to the rich—and often physically non-intuitive-mechanical behavior of knots and tangles, researchers have explored their mechanics using theory [121], simulations [122-126], and experiments [119, 127]. Modeling of friction in theories and simulations usually relies on heuristic observations, e.g., Coulomb’s law of friction. Systematic experiments can help uncover the role of various ingredients—topology, friction, and material stiffness—on the mechanics of knots. Jawed et al. [119] varied the topology of overhand knots and explored the force required to pull the knots tight. Patil et al. [127] used knotted fibers that change their color upon material deformation and analyzed the mechanics of a few commonly used knots. To the best of our knowledge, none of these prior works used the coefficient of friction as a control parameter despite its critical role in determining the strength of a knot [119]. This paper addresses the critical challenge of systematically varying the friction coefficient of rods by welding asperities to the outer surface of otherwise smooth elastomeric rods.

Various particle delivery techniques are available under different operating conditions. Vacuum deposition techniques like physical vapor deposition [16, 17], chemical vapor deposition [18, 19], or plasma sputtering [20, 21] methods are generally applied for thin and uniform deposition of metallic layers in low to high vacuum conditions, which makes them slow, arduous, and expensive at industrial scale. For example, a nickel-phosphorus (Ni–P) thin film through electroless plating

is reported a uniform 64 μm thickness with 6 h of operation time [128]. In contrast, solution or sol-gel coating methods [86] (i.e., dip coating, spin coating, spray coating, roll coating, blade coating, and Langmuir–Blodgett) can be applied in atmospheric conditions where the solution evaporates and makes a dried thin-film [85, 129, 130].

Dip coating is a wet deposition method by immersion of the substrate into a solution, mixture, or collision. It is an effective and straightforward way of thin film/layers formation of pure liquid or hydrolyzable metal compounds or readily formed particles. It is extensively used as a coating method due to its simplicity, low cost, and reasonable control over the thickness. The mixtures are often embedded with inorganic fillers, nanoparticles, or clusters (d < 30 nm) that produce thin-film-impregnated particles ranging from nanometers to a couple of microns. Such a coat of pure-polymer or impregnated nanoparticles acts as a lubricant [131] and creates abrasion-resistance coating for many applications including orthodontic wires [132], guidewires for angiography and interventional procedures, self-lubricated corona resistant electrical wire [133], anti-icing surface [134], super hydrophilic or olio-phobic surface, etc.

In previous studies, four parameters (coating-to-substrate hardness relationship, the thickness of the coating, surface roughness, and size and hardness of debris in the contact) have been mentioned that control friction in the tribological contact process [135]. Particles are transferred in the interface of the substrate while withdrawing from the suspension [25, 91]. The efficiency of particle transfer is dictated by the competition between the capillary force and viscous drag force during the withdrawal of the substrate [26]. The thickness of the material transfer over a flat plate can be determined by the famous Landau–Levich–Derjaguin (LLD) equation [27, 28] which is $h = 0.94 L_C Ca^{2/3}$. Here, $L_C = \sqrt{\gamma/\rho g}$ is the capillary length and $Ca = \eta U/\gamma$ is the capillary number; γ and η are the surface tension and the viscosity of the suspension, U is the withdrawal

speed of the substrate, and g is the acceleration with respect to gravity. The modified LLD equation for the cylindrical substrate is expressed as $h = 1.34rCa^{2/3}$which is used to predict the material transfer over the wires and fibers [47]. This film formation technique over the substrate is widely used in various industrial applications such as modification of cutting tools [136], corrosion protective layer [7], biosensors [43], particle filtration [13, 41], and joining of the metal lattice structure produced with a continuous thin rod [37, 105].

The aim of this work is to observe the mechanical response of the knots by the variation of the friction force. The comparison of the snapshots of the shape of the knots of experiment and simulation at six different positions are presented in Figure 24. Non-spherical irregular edge-shaped particles are entrained over the elastic rods which are subject to introduce the asperities. The asperities over the elastic rods result in an increase in friction forces. Thus, the friction force is controlled by controlling the particle adherence over the substrate during the coating process. Moreover, the coefficient of friction is determined by fitting the experimental results with the simulation results.

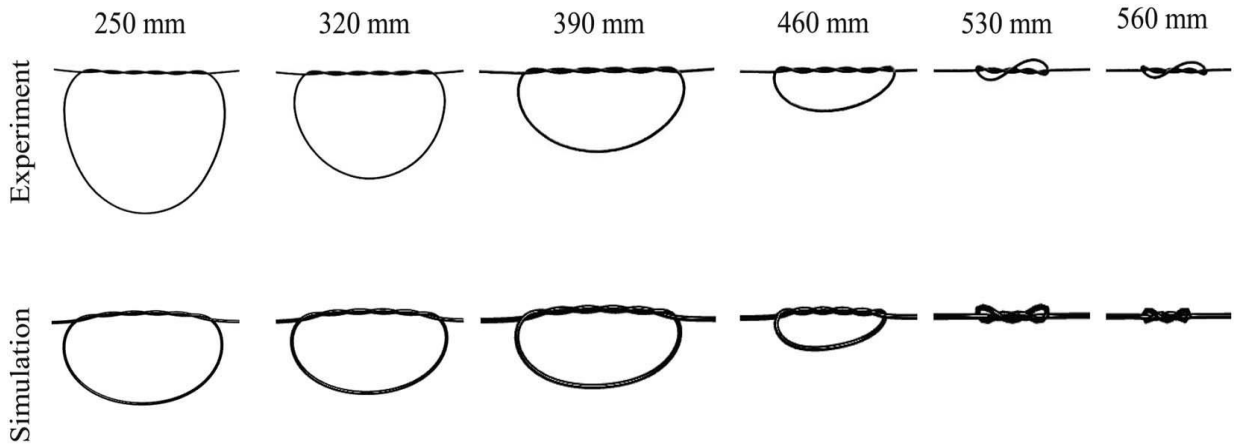

Figure 24: Comparison of the shape of the knots in both experiment and simulation at six different positions. The uncoated rod at n=3 is used for the comparison and initially, the end-to-end length is 250 mm for both experiment and simulation. [Simulation figures were provided by collaborator]

Experimental Setup: Materials and Method

This section includes the materials used for the experiments and the method of the experiments. First, the preparation of the rods and the coating mixture is discussed. The following sections discuss the development of coating setup, characterization of the coated rod, and friction test method.

Preparation of Rods and Coating Mixture

Natural rubber rod (weather and abrasion resistant; color: black; purchased from McMaster-Carr, USA) is used as the substrate to observe the variation of friction forces with the variation of particle volume fraction in the suspension. The temperature range of the rubber rod is -59 °C to 122 °C and the diameter (d) of the rod used in all the experiments is 1/16 in. (1.59 mm approximately). The Young's modulus (E) of the elastic rod is 1.83 MPa, measured by the universal testing machine (MTS criterion, USA) and the tensile strength of the rod is 17.24 MPa (manufacturer provided).

The surface of the rod is fairly smooth, and the friction will be introduced by delivering inorganic particle asperities on the surface. For uniform deposition of the particles on the rod substrate, a liquid carrier system (LCS) is prepared as the particle-bearing liquid.

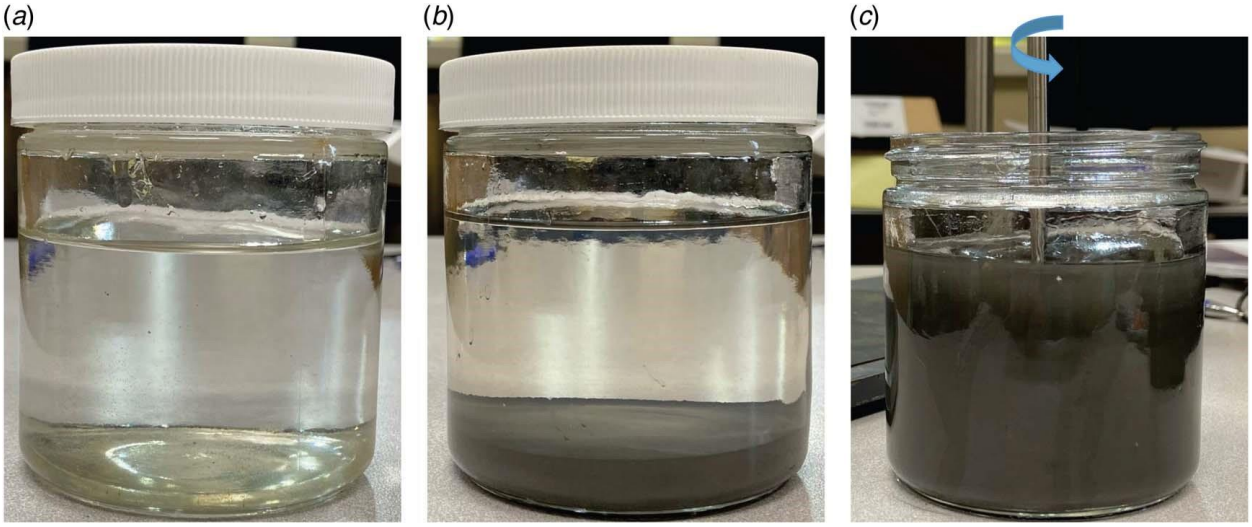

Figure 25: Preparation of particle mixture: (a) LCS; solution (solute+solvent), (b) added particles in LCS, and (c) pseudosuspension of the mixture by stirring.

The LCS consists of polymethyl methacrylate (MW ~ 15000 g/ mol; Sigma Aldrich, USA) as the binder, which has low density (~1.19 g/cm^3), ~41 mN/m surface tension, and is a benign, nonexplosive, and non-flammable material [137]. 1,3-Dioxolane (from Sigma Aldrich, USA) is used as the solvent, which has 34.3 mN/m surface tension, 1.06 g/cm^3 density, and vapor pressure of 79 mmHg at 20 °C [138]. A magnetic stirrer is used for 8 h to confirm the complete dissolution of the granular solute in the liquid solvent, which is also confirmed by XPS (Figure 25(a)). Iron metal reduced powder (particles size 45–150 μm, ChemCenter LLC, CA) is considered to create the asperities on the elastic rod surface. The solid inorganic particles are added at a premeasured particle volume fraction (ϕ_p) in the LCS gradually to create the dipping mixture as shown in Figure 25(b).

Adding binder and immiscible particles to a liquid transforms its rheological properties. The addition of particles will act as obstacles to the fluid flow which will induce a non-linear dependency under applied shear (non-Newtonian). At a higher volume fraction, the mixture may exhibit friction-induced continuous shear thickening or discontinuous shear thickening [106], causing a stress-induced solid-like shear jammed state. Similarly, adding binder will increase the viscosity, which may facilitate the particle adherence, but it may cause non-uniform particle to transfer due to the high viscosity nature of the mixture. For our experiments, the binder volume fraction is kept at ϕ_b = 5%, while the volume fraction of the particles is varied between ϕ_p = 1% and 13% so that the mixture performs way below the effective viscous regime. The non-spherical irregular edged shape rough surface morphology of the raw particles is shown in Figure 26. The particle size selected to alter the friction coefficient is $\ll$1 mm, which will ensure that the other relevant physical parameters (e.g., cross-sectional radius) are not altered when the friction is varied.

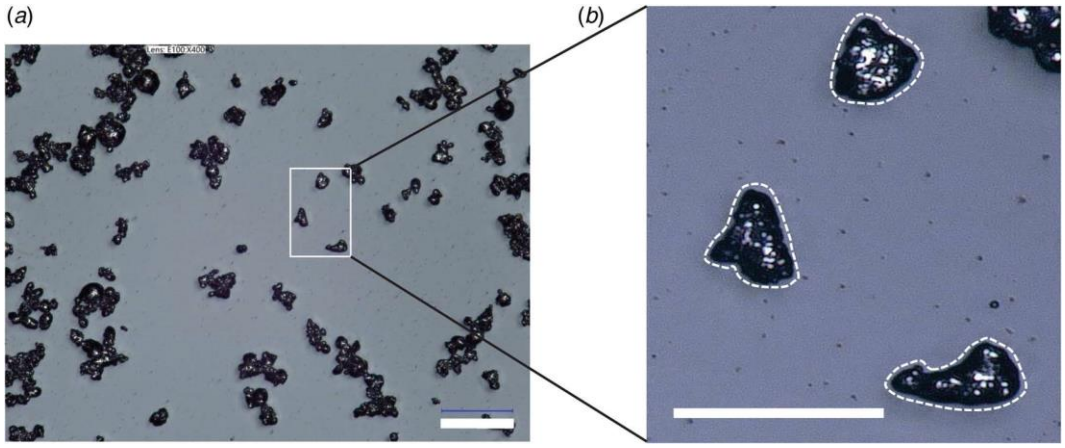

Figure 26: (a) Shape and morphology of the raw particles. Scale bar is 100 μm for (a) and 50 μm for (b).

Development of Coating Setup

A standardized continuous dip coating protocol has been developed in our laboratory for depositing particles from a liquid carrier system to the cylindrical elastic rod substrate. The schematic of the coating setup is depicted in Figure 27 which is composed of a dipping jar, guiding rollers, impeller, motor, and the control box for the motor. The dipping jar used in the experiments is cylindrical in shape, screw top, clear borosilicate glass with round bottom, and the inner diameter (D_i) and height of the dipping jar (H) are 80 mm and 100 mm, respectively. Two sink rollers (*R1* and *R2* in Figure 27) are used as guides for the elastic rods to ensure the fixed dwelling time and another turn-up roller (*R3*) is used as a guide during the pulling of the coated rod by the motor *M*. The diameter of both *R1* and *R2* is 0.75 mm and the diameter of *R3* is 35 mm. The gap between *R1* and *R2* (R) is 50 mm. The clearance between the two guide rollers (*R1* and *R2*) and the impeller is 5 mm. The height of the mixture (Z) is kept at 60 mm, shown in Figure 27.

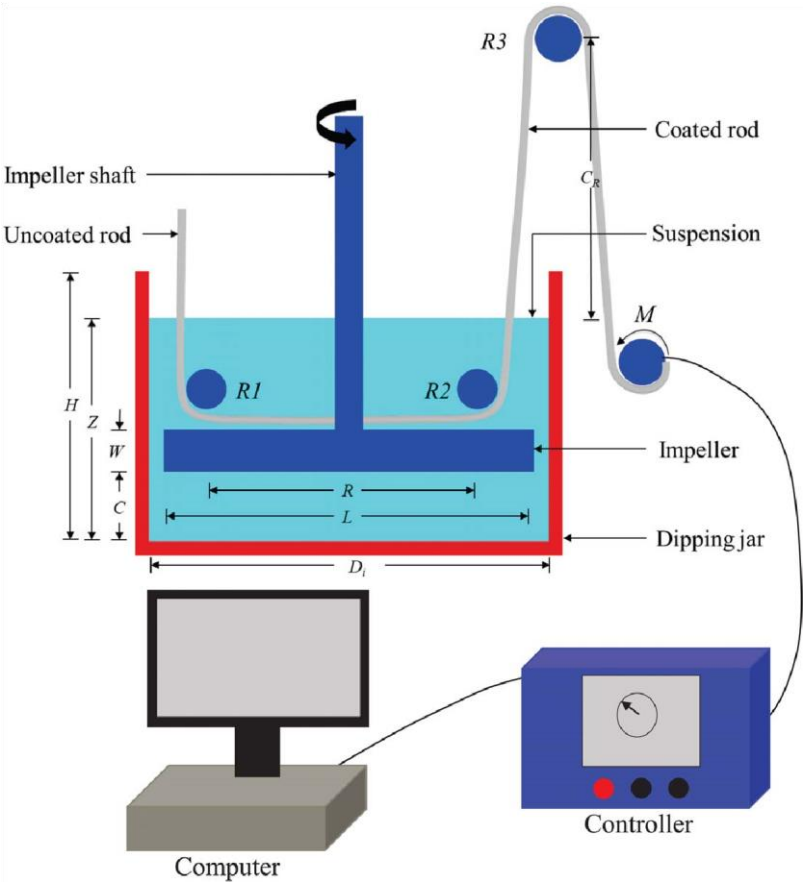

Figure 27: Schematic diagram of the experimental setup for continuous coating of the elastic rod (not to scale)

The density of the particles is 7.8 g/cm^3 which is much higher than the LCS used in this experiment. Due to higher density, sedimentation of the particles is observed within a very short time. As a result, external kinetic energy is required to keep the particles suspended. A straight blade impeller is used in the experiments to provide kinetic energy to keep the particles suspended. The length (L) and the width (W) of the impeller are 70 mm and 12.5 mm, respectively, which are shown in Figure 27. A pressure difference is created from the rotation of the impeller which helps the particles to encounter the gravitational force of the particles. The clearance between the impeller

and the bottom of the dipping jar (*C*) is 5 mm. The rotational speed of the impeller is kept at just suspending speed of the particles to minimize the vortex in the mixture.

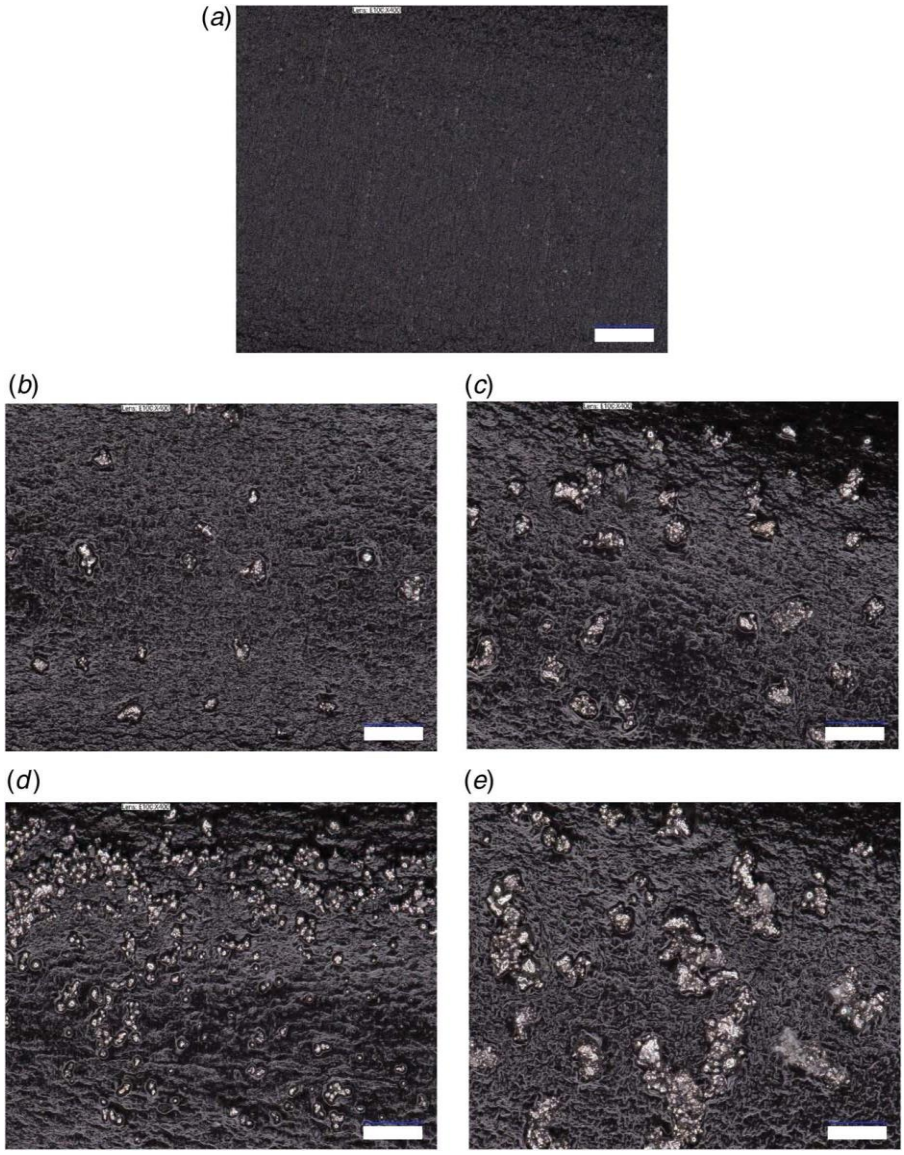

Figure 28: Surface morphology of the elastic rod: (a) uncoated; coated with (b) 1% particle, (c) 4% particle, (d) 7% particle, and (e) 13% particle. Scale bar is 100 μm.

A Flashcut controller controls the motion of the motor, which is driven by G-code and pulls the rod. The withdrawal speed of the rod is kept at 5 mm/s which makes the dwell time of the rod in

the suspension to be about 10 s. The withdrawal speed is controlled within ±2% precision by using the high-precision bipolar stepper motor (SANYO) connected to a computer. After the rod is immersed in the dipping mixture, the evaporating solvent dries from the surface before it reaches the roller *R3*, where C_R is 2.5 m. The coated rod is then collected and is placed inside an oven at 80 °C for an hour to ensure uniform drying.

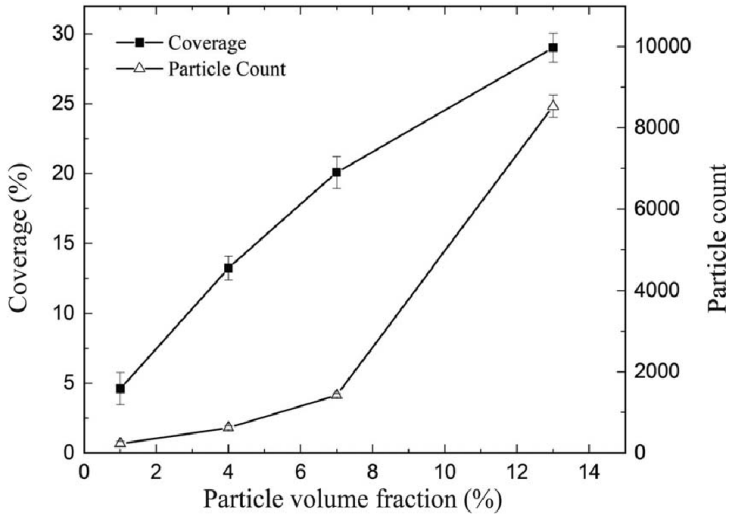

Figure 29: Variation of coverage and particle count with particle volume fractions.

Characterizing the Coated Rod

The morphology of the micro-particle-coated elastic rods is investigated after drying. VHX 7000 Digital 4K microscope (KEYENCE Corp., IL) at 400× is used for the imaging of the particle-coated elastic rods. High resolution 4K images of the dipped rod are taken with the microscope and the images are analyzed with IMAGEJ software. The surface morphology of the coated rod is shown in Figure 28. Surface coverage is measured as the ratio of the area covered by the particles and the area of the rod. At least three images from three different regions are selected and analyzed over the substrate for determining the particle counts and surface coverage to ensure statistical significance. The variation of the coverage and particle count is presented in Figure 29.

Developing the Friction Test Setup

To measure the friction, three samples of particle-coated elastic rods of 600 mm length are prepared and dried. Self-intersection of the rod is achieved by tying knots as shown in Figure 30. One end of the coated rod is mounted to a fixed clamp and the other end is joined with the hook of the digital push-pull force gauge (20 N). The force gauge is connected to a computer and the variation of forces at different pulling lengths is recorded at a 10 Hz rate. The motion of the force gauge is controlled by a controller with a high-precision bipolar stepper motor. The pulling speed of the rod is kept at 200 mm/min for the experiments.

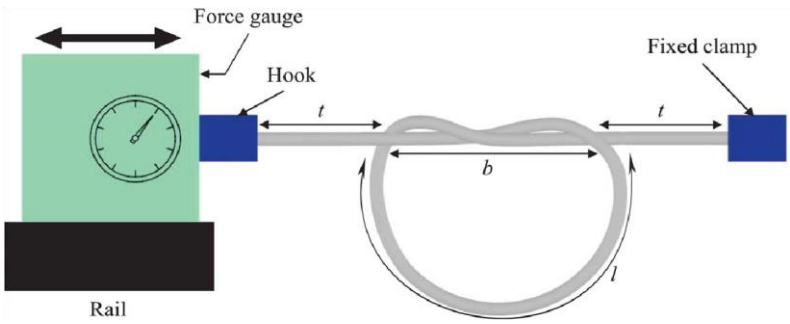

Figure 30: Schematic diagram of pulling force measurement setup with different parameters of knots (not to scale)

In this present work, the length of self-intersection for the rod is controlled with knot numbers. Up to four knots are used to observe the variation of the friction force for the rod coated with different volume fraction of particles. Tail length (t), braid length (b), and loop arc length (l) are the defining parameters shown in Figure 30. The end-to-end length is defined as the gap between the fixed clamp and hook of the force gauge where two ends of the elastic are mounted. Similar parameters can resemble the higher number of knots. The total length is taken as 300 mm for one and two knots, while 600 mm for three and four knots. This is to overcome the fluctuations of the forces

due to the large tail length. Each friction test is performed three times to demonstrate the statistical significance. The parameters of different knots before pulling are listed in Table 3.

Table 5: Pulling parameters for different knots (n = 1, 2, 3, 4)

Knot (n)	Tail length, t (mm)	Braid length, b (mm)	Loop arc length, l (mm)	End to end length (mm)
1	35	30	170	100
2	25	55	140	100
3	80	95	250	250
4	45	110	290	200

Results and Discussion

The experimental and simulation results are presented in this section. During the experiment, the forces required for pulling the rods are measured and discussed here. The asperities introduced by the adhesion of hard particles on the substrate are also discussed. The variation of forces measured by the push–pull force gauge is then plotted to compare with the simulation result in this section.

When the thin rod is dipped in the heterogeneous mixture, a thin polymer film is adsorbed at the solid-liquid interface, creating a viscous layer. As the rod exits the mixture, a convective flux acts on particles which is generated from the solvent evaporation and the capillary rise [25, 50]. The upward convective flux increases with the withdrawal speed, and the viscous drag force starts to dominate the particle adhesion. At a lower volume fraction of binder and particles, the viscous layer is thinner and the capillary effect in LCS remains high. The balance between the viscous drag and the capillary action determines the particle entrainment on the rod substrate. Particle transfer occurs at the three-phase boundary [139] during the withdrawal stage due to entrainment, when the viscous drag force becomes larger than the resistive capillary force in liquid molecules. The liquid film thickness (viscous layer), particle size, and volume fraction influence the entrainment

of particles [13]. The effects of convective flux acting on the particle-laden mixture vary due to particle polydispersity, which creates a variation in the viscous drag force for entrainment. Additionally, the volumetric density of particles in the entrainment zone can become higher than the rest of the mixture due to the continuous flux of particles formed by the convective forces in the heterogeneous mixture [50]. For this reason, entrained particle coverage can become higher than the corresponding particle area coverage in the bulk mixture which can be observed in Figure 29. For example, with the same 10% volume fraction of particles in the mixture, coverage increases from 5% to 27%. The adhesion of these particles on the elastic rod transforms the smooth surface morphology through asperities.

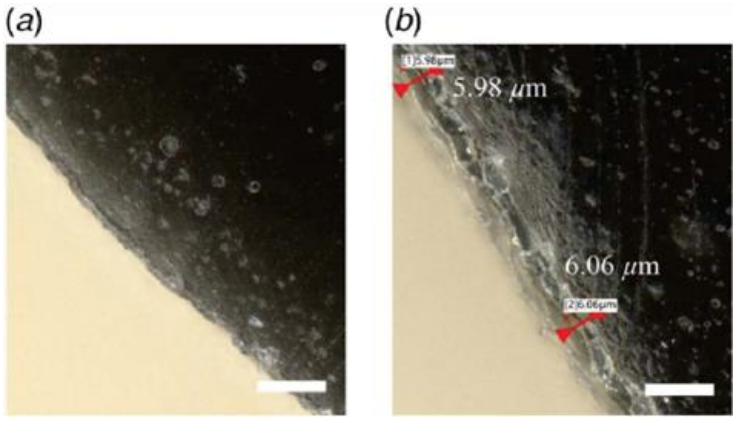

Figure 31: Cross section of the elastic rod: (a) uncoated and (b) polymer coated. The polymer film is clearly evident in (b). Scale bar is 25 μm.

During the pulling of the elastic rods, each strand of the braid is subjected to two external forces [119]. The forces are traction/pulling force (acting due to tensile load on the tails) and the friction forces (due to the self-contact of the rods in the braid). Total elastic energy of a rod is composed of stretching energy, twisting energy, and bending energy [125]. The detailed simulation process of the elastic rod is described in Sec. 2. The pulling force provided by the push–pull force gauge

during the experiment can be used to determine the friction force and friction coefficient as discussed in Sec. 2.

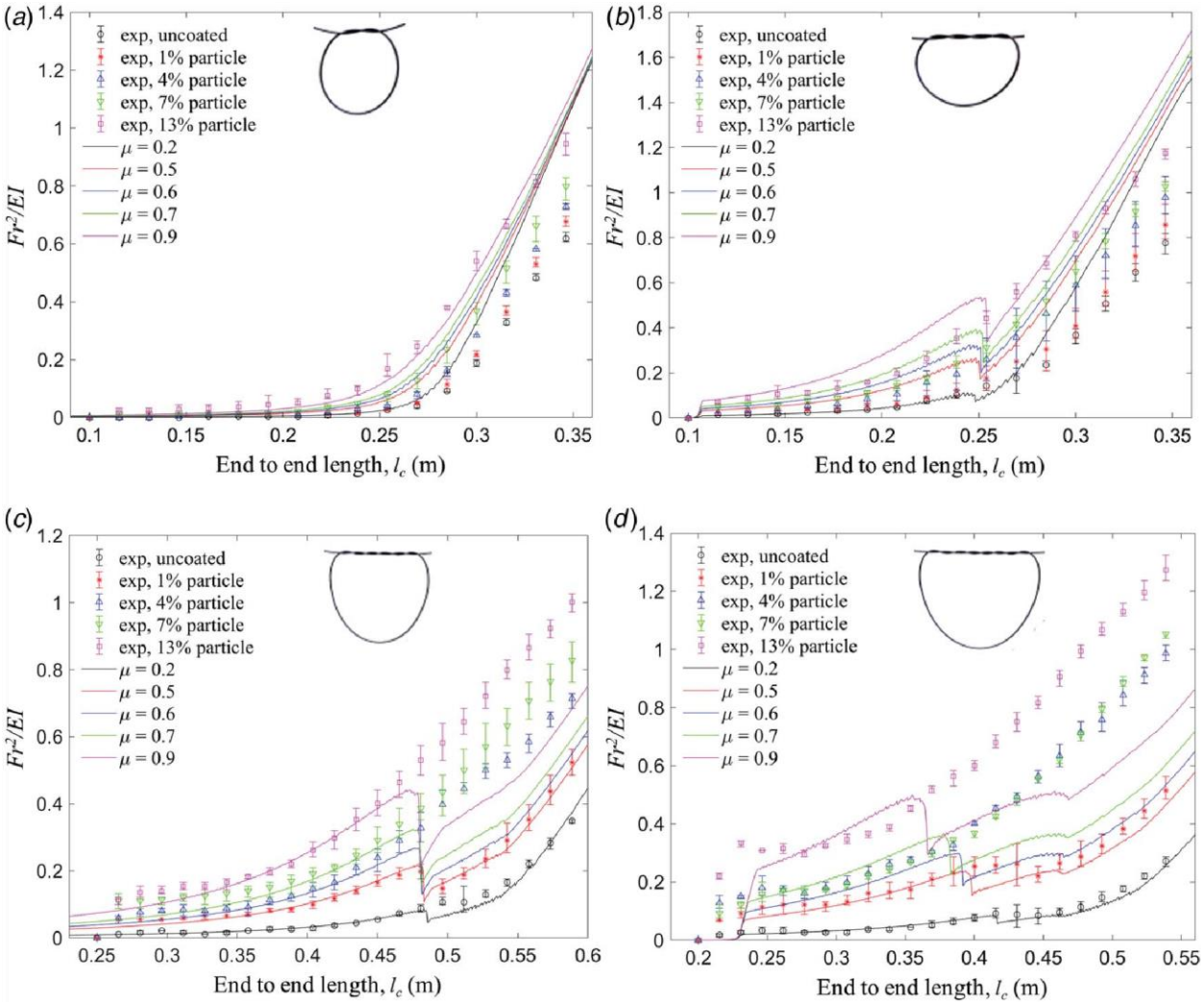

Figure 32: Experimental and simulation result of pulling force: (a) one knot, (b) two knots, (c) three knots, and (d) four knots. The point with the error bar represents the experimental results and the continuous line represents the simulation results. [Simulation results were produced by collaborator]

The pulling force required is dependent on the surface asperities produced by the transferred particles adhered to the viscous binder layer, which can be observed in Figs. 9(*a*) and 9(*b*)

representing the cross section of the uncoated and coated substrates. The polymer layer thickness is a function of dimensionless capillary number which is measured as (5.85 ± 0.17 μm) using a VHX 7000 Digital 4K microscope (KEYENCE corp., IL) after 8 h from dipping. During the continuous dipping process described in Sec. 3, particles are entrained on the viscous layer changing the surface morphology. We have observed some loss of loosely adhered particles during pulling, but the number is insignificant compared to the total number of transferred particles. The oven drying has helped the uniform adhesion of particles on the substrate and no significant difference between the three pulling replications has been observed in our experiment. Increasing the particle volume fraction in the dipping mixture increases the volumetric density of particles in the entrainment zone and a systematic variation can be observed in Figure 28.

The deposition of the particles on the elastic rod increases with the increase of the particle volume fraction in the suspension. Uniformly distributed particles deposition over the substrate is observed for lower volume fraction (≤ 7%) particle. Particles started to cluster at an increased volume fraction (13%) as shown in Figure 28(*e*). Such aggregates will induce larger asperities, which can increase the self-intersecting friction during pulling. Surface coverage follows the similar pattern of increased coverage with increasing volume fraction as shown in Figure 29. A total of 4.61 ± 1.15% surface coverage is measured for 1% particle volume fraction while the maximum surface coverage (29.02 ± 1.05%) is observed with the 13% particle volume fraction in the suspension. Particle count also follows a similar pattern as the surface coverage (i.e., minimum particle count is observed in 1% and maximum particle count is observed in 13% particle) which is presented in Figure 29. The pulling forces recorded by the force gauge confirm this relationship of increasing friction forces.

The experimental results shown in Figure 32 represent the increasing trend of pulling forces with increased particle volume fraction and contact area (i.e., knot number). Regularized pull force (Fr^2/EI) is plotted against end-to-end length (l_c), where F is the pull force, r is the cross-sectional radius of the rod, and EI is the bending stiffness. For each knot number, the contact area in the braid represented in the knot geometry (shown in Figure 30) remains the same. Due to the thin polymer layer generation after coating, no significant difference can be assumed between coated and uncoated contact areas along the length. Furthermore, no infusion of polymer binder can be observed from the cross section (Figure 31), thus the elastic properties of the rod before and after coating have been assumed unchanged in our simulation. As a result, the variation in the external pulling force within each knot can be attributed to the change in contact friction force. The uncoated rod experienced the lowest friction force at each end-to-end length which gradually increases with particle volume fraction. Three sets of data are collected for each experiment with each knot and particle volume fraction. The simulation data are generated and compared with the best fitted friction coefficient parameter which is found as μ = 0.2, 0.5, 0.6, 0.7, and 0.9 for uncoated, 1%, 4%, 7%, and 13%, respectively. The fitting between simulation and experimental data can be observed in Figure 34. We observed good agreement between simulation and experimental results with a few exceptions, which is discussed in the later section.

Comparison of the experimental and the simulation results at different conditions are shown in Figure 32 which demonstrates the increase in friction forces with the increase in knot number and particle volume fraction. During pulling, a tensile force will be applied along the tail length which will propagate through the braid length. This will create a sliding motion shrinking the loop length. As a result, static friction followed by dynamic friction should be observed in our force-displacement plot. The higher slope at the beginning of the force-displacement curve represents

the static friction; after that, dynamic friction shows gradual increase in the friction force. This is clearly observed for n > 1 in both experimental and simulation results. However, for n = 1, sudden increase of the friction force at the beginning of pulling (static friction) is not observed due to minimum contact area in the braid length.

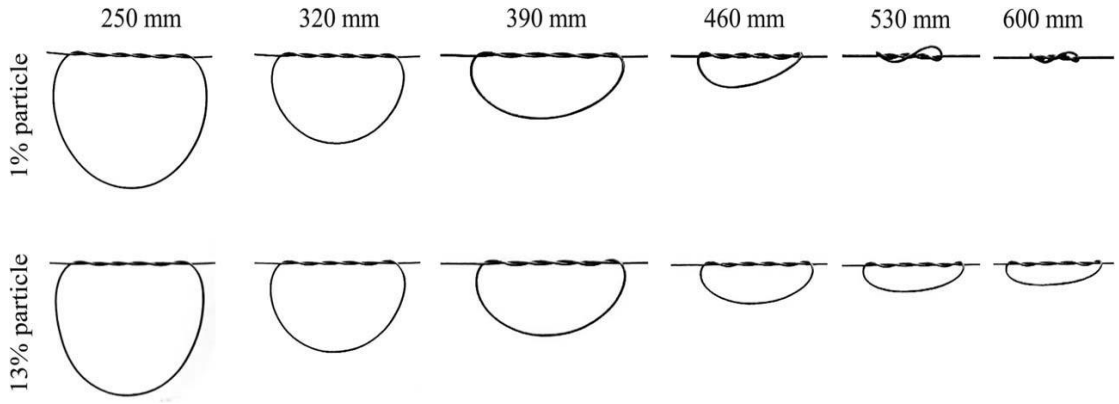

Figure 33: Change in shape of knots (n=3) rods coated with 1% (top) and 13% (bottom) particle.

During pulling of the tails, the traction/pulling force is transferred along the longitudinal direction of the rod. Due to the self-intersecting topology of the knot, an opposing friction force will act to counter the traction/pulling force. As the magnitude of the traction/pulling force increases, the internal energy of the rod (i.e., stretching, twisting, and bending) increases accordingly, which is expressed in Eq. (9). The spiral topology of the knots creates two opposing flows at the braid resulting in a local moment inside the loop. Additionally, it counters the global moment caused at the two ends of the tails due to pulling. The sliding force facilitates the internal moment causing instability in the loop which is defined as the inversion point [125]. A sudden drop in pull force can be observed at the inversion point and the knot comes to the lowest energy state. In experiments, when the sliding is refrained due to higher friction caused by asperities or contact area (knot number), the knot starts to behave differently and stretching energy dominates the pulling behavior. In such scenarios, no inversion point can be observed. In another word, inversion

or no inversion will depend upon the friction force experienced at the knot. These phenomena are clearly evident in our experimental result presented in Figure 32.

At single knot (n = 1), no inversion point can be observed in both experiment and simulation results. This is due to minimum self-contact sliding region which result in minimum friction force. The force versus displacement curve generated by experiment and simulation shows good agreement till the end-to-end length of 250 mm. Afterward, the simulation data overpredicts the experimental results except 13% particle volume fraction. The overprediction by the simulation can be observed in two knots as well. However, inversion point has been observed for uncoated (μ = 0.2) and 1% particle (μ = 0.5) volume fraction. The drop in forces at the inversion point is relatively low compared to the prediction from simulation. For higher friction coefficient (μ = 0.6, 0.7, and 0.9), the deviation increases including disagreement in inversion point, but the curve shows similar pattern. It is observed both from the experiment and simulation that the inversion point occurs sooner as the friction increases. This shows the dependency of the inversion point with friction coefficient [125].

In the case of three and four knots (n = 3 and 4), the experimental result nicely follows the prediction from simulation. The fits mostly remain within the one sigma of the error bar till the inversion points. Inversion point has been observed for uncoated (μ = 0.2) and 1% particle (μ = 0.5) volume fraction. Both the drop in force and the predicted force matches the experiment beyond the inversion point. It should be noted that no inversion point can be observed for higher friction coefficient (μ = 0.6, 0.7, and 0.9) due to the complex nature of the acting force discussed above.

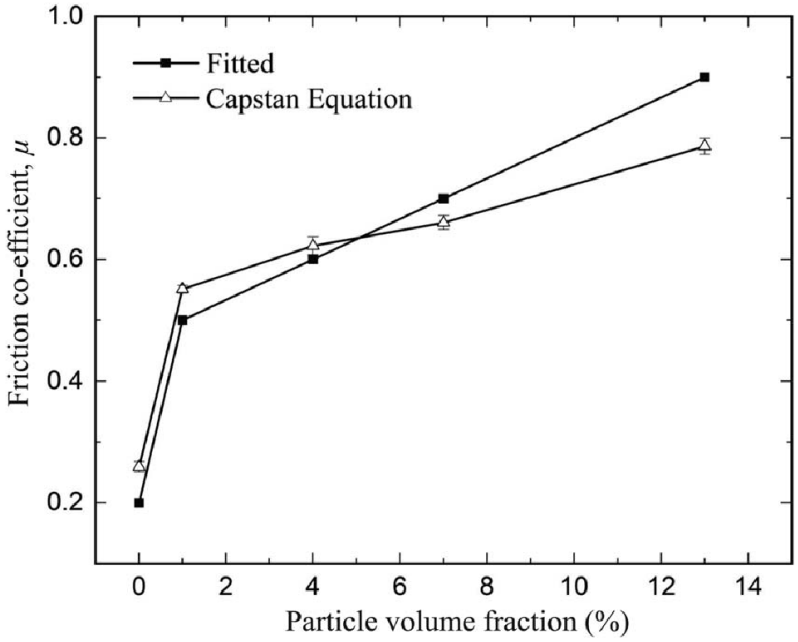

Figure 34: Variation of friction coefficient with particle volume. [Fitted data were provided by collaborator]

Variation in the shape of the knots, presented in Figure 33, confirms the effect of the particle volume fractions on the friction forces. The snapshot of the knots is taken at six different positions for the uncoated rod and the coated with 13% particle in the suspension and is presented in this work. It is clearly evident from Figure 33 that the shape of the knots at different pulling lengths is controlled by the friction coefficients of the coated rods that depends on the particle volume fractions in the suspensions.

The relation between the friction coefficient and the particle volume fraction is shown in Figure 34 which shows that the variation of the coefficient of the friction is directly dictated by the volume fraction of particles in the suspension. It is observed from Figure 34 that coated rod with only 1% particle in the suspension changes the friction coefficient almost 150% (μ = 0.5). Moreover, proportional relationship is observed between the variation of friction coefficient and particle

volume fraction in the suspension. To compare the fitted simulation, an experiment is designed to measure the friction coefficient following the capstan equation. A larger diameter rod (1/4 in.) of the same material is used as the capstan. Both the capstan and the rod are coated in the same suspension following the protocol discussed earlier. The rod slides over the capstan following the weight difference at two ends and the friction coefficient is calculated [140] which is presented in Figure 34. The friction coefficient of the coated rod increases with the increase of the particle volume fraction in the suspension which is also observed in the simulation results. A slight variation between capstan and simulation method can be observed at higher particle volume fractions (7% and 13%). This is due to particle cluster formation at higher particle volume fractions compared to non-clustered particle distributed at low particle volume fraction (uncoated, 1%, and 4%) coat. The similar trend between the two methods demonstrates the accuracy of our proposed simulation technique. This relationship between the friction coefficient and particle volume fraction can help to predict the required particle volume fractions for achieving desired friction coefficient.

Concluding Remarks

This article reports a novel method for the variation of friction forces of the elastic rods by adhering non-spherical irregular edged shaped particles. When the particles are transferred, asperities are introduced over the surface which results in an increase in the friction forces. The particle transfer increases with the increase in the particle volume fraction in the suspension. The friction force increases during the self-contact of the rods due to the increase in particle transfer. Experimental results demonstrate the variation of friction forces and friction coefficient with particle volume fractions. Moreover, a systematic variation of experimental value of the friction force is observed with the particle volume fractions in the suspension except one case in four knots. The relationship

between the friction coefficient and particle volume fraction in the suspension shows promising result to manufacture an elastic rod with specific friction coefficient. The results can be extrapolated to find the particle volume fraction to obtain an elastic rod with desired friction coefficient. However, changes in particle morphology may require establishing a new relationship.

A numerical prediction technique is also proposed and implemented for determining the coefficient of friction which shows good agreement with the experiment data at lower coefficient of friction. Some disagreements can be observed with the increase in asperities due to the effect of the other forces (bending, twisting, and contact forces; the moment due to these forces) present at higher contact area (increased knot number) and higher friction force. Some possible causes of discrepancies in Figure 33 may also be attributed to particle clustering, particle polydispersity, irregular particle shape, local variation in adhered particle distribution, and change in mechanical properties of the coated rod. Performing the experiment at a slow speed, with uniform particle morphology, and gripping the tail to avoid rotation can help minimize the difference between experiment and simulation results.

CHAPTER 5

CONCLUSION

The main focus of this thesis is the optimization of process parameters for particle transfer using both entrainment and entrapment methods. This involves creating a polymer thin film from a density mismatching heterogeneous suspension, which can regulate friction force on a smooth surface and filter particles from a polydisperse mixture. High-density inorganic particles are transferred onto the substrate using an organic binder, with rotational energy maintaining their suspension. Process parameters were optimized to achieve controlled particle delivery, and the optimal conditions for particle delivery were determined to be at 250 rpm, with binder concentration having no impact on the minimum suspending speed due to the low density of the binder.

The size of the entrapped particle is primarily dependent on the thickness of the film formed over the substrate in the submerged condition and we used this for the particle filtration. A non-dimensional parameter called entrapment factor (*Ef*) was introduced to describe different regimes of sorted particles. For example, Zone-A ($7.6\times10^3 < Ef < 8.8\times10^3$) can separate the particles ≤ 2.05 μm.

By controlling the particle concentration in the suspension, the transfer of particles over a smooth rod can be regulated during entrainment, and this, in turn, controls the friction force. By systematically delivering particles over the surface, the friction force of an elastic during self-contact can also be controlled. At a coating condition of 13% particle transfer, the maximum friction force was observed, with a friction coefficient value of 0.9.

REFERENCES

[1] D. Quéré, "Fluid coating on a fiber," *Annual Review of Fluid Mechanics*, vol. 31, no. 1, pp. 347-384, 1999.

[2] R. A. Bowling, "A Theoretical Review of Particle Adhesion," Springer US, 1988, pp. 129-142.

[3] M. Brogly, "Forces Involved in Adhesion," Springer International Publishing, 2017, pp. 1-28.

[4] Y. I. Rabinovich, J. J. Adler, A. Ata, R. K. Singh, and B. M. Moudgil, "Adhesion between Nanoscale Rough Surfaces: II. Measurement and Comparison with Theory," *Journal of Colloid and Interface Science*, vol. 232, no. 1, pp. 17-24, 2000/12/01/ 2000, doi: https://doi.org/10.1006/jcis.2000.7168.

[5] C. Islam and Y. Altintas, "A Two-Dimensional Transient Thermal Model for Coated Cutting Tools," *Journal of Manufacturing Science and Engineering*, vol. 141, no. 7, 2019, doi: 10.1115/1.4043578.

[6] X. Tang and X. Yan, "Dip-coating for fibrous materials: mechanism, methods and applications," *Journal of Sol-Gel Science and Technology*, vol. 81, no. 2, pp. 378-404, 2017/02/01 2017, doi: 10.1007/s10971-016-4197-7.

[7] A. F. Galio, S. V. Lamaka, M. L. Zheludkevich, L. F. P. Dick, I. L. Müller, and M. G. S. Ferreira, "Inhibitor-doped sol–gel coatings for corrosion protection of magnesium alloy AZ31," *Surface and Coatings Technology*, vol. 204, no. 9, pp. 1479-1486, 2010/01/25/ 2010, doi: https://doi.org/10.1016/j.surfcoat.2009.09.067.

[8] S. D. R. Wilson, "The drag-out problem in film coating theory," *Journal of Engineering Mathematics*, vol. 16, no. 3, pp. 209-221, 1982, doi: 10.1007/BF00042717.

[9] C. Gutfinger and J. A. Tallmadge, "Films of non-Newtonian fluids adhering to flat plates," *AIChE Journal*, vol. 11, no. 3, pp. 403-413, 1965, doi: 10.1002/aic.690110308.

[10] E. K. Choi, J. Park, B. S. Kim, and D. Lee, "Fabrication of electrodes and near-field communication tags based on screen printing of silver seed patterns and copper electroless plating," *International Journal of Precision Engineering and Manufacturing*, vol. 16, pp. 2199-2204, 2015.

[11] R. Liang, J. Hou, H. Zang, J. Chung, and S. Tseng, "Microcup® displays: Electronic paper by roll-to-roll manufacturing processes," *Journal of the Society for Information Display*, vol. 11, no. 4, pp. 621-628, 2003.

[12] K. S. Nanjundaswamy, H. D. Friend, C. O. Kelly, D. J. Standlee, and R. L. Higgins, "Electrode fabrication for Li-ion: processing, formulations and defects during coating," in

IECEC-97 Proceedings of the Thirty-Second Intersociety Energy Conversion Engineering Conference (Cat. No. 97CH6203), 1997, vol. 1: IEEE, pp. 42-45.

[13] I. Khalil and B. Khoda, "Sorting of Poly-Disperse Particle by Entrapment Using Liquid Carrier System," *Journal of Manufacturing Science and Engineering,* vol. 144, no. 5, 2021, doi: 10.1115/1.4052440.

[14] M. I. Khalil and B. Khoda, "Size-Based Filtration of Poly-Disperse Micro-Particle by Dipping," 2022. [Online]. Available: https://doi.org/10.1115/MSEC2022-85680.

[15] M. Ibrahim Khalil, D. Tong, G. Wang, M. Khalid Jawed, and B. Khoda, "Systematic Variation of Friction of Rods," *Journal of Applied Mechanics,* vol. 89, no. 11, p. 111007, 2022.

[16] D. W. Kang, M. Kang, and J. W. Hahn, "Keystone error analysis of projection optics in a maskless lithography system," *International Journal of Precision Engineering and Manufacturing,* vol. 16, no. 2, pp. 373-378, 2015.

[17] J.-T. Lv, Y. Yan, W.-K. Zhang, Y.-H. Liu, Z.-Y. Jiang, and G.-Y. Si, "Plasmonic nanoantennae fabricated by focused Ion beam milling," *International Journal of Precision Engineering and Manufacturing,* vol. 16, no. 4, pp. 851-855, 2015.

[18] T. Kobayashi *et al.*, "Production of a 100-m-long high-quality graphene transparent conductive film by roll-to-roll chemical vapor deposition and transfer process," *Applied Physics Letters,* vol. 102, no. 2, p. 023112, 2013.

[19] W.-S. Chu *et al.*, "Hybrid manufacturing in micro/nano scale: a review," *International journal of precision engineering and manufacturing-green technology,* vol. 1, no. 1, pp. 75-92, 2014.

[20] Y.-S. Hong, S.-R. Lee, J.-H. Kim, and S.-Y. Lee, "Application of a DLC-Coating for improving hydrostatic piston shoe bearing performance under mixed friction conditions," *International Journal of Precision Engineering and Manufacturing,* vol. 16, no. 2, pp. 335-341, 2015.

[21] Y. Yang, K.-H. Kim, and J. L. Ong, "A review on calcium phosphate coatings produced using a sputtering process—an alternative to plasma spraying," *Biomaterials,* vol. 26, no. 3, pp. 327-337, 2005.

[22] Q. Zheng *et al.*, "Transparent conductive films consisting of ultralarge graphene sheets produced by Langmuir-Blodgett assembly," 2011/07//, vol. 5: American Chemical Society, 7 ed., pp. 6039-6051, doi: 10.1021/nn2018683. [Online]. Available: https://pubs.acs.org/doi/abs/10.1021/nn2018683

[23] E. Cohen and E. J. Lightfoot, "Coating Processes." Hoboken, NJ, USA: John Wiley & Sons, Inc., 2011, pp. 1-68.

[24] X. Gu, P. A. Trusty, E. G. Butler, and C. B. Ponton, "Deposition of zirconia sols on woven fibre preforms using a dip-coating technique," *Journal of the European Ceramic Society,* vol. 20, no. 6, pp. 675-684, 2000, doi: 10.1016/S0955-2219(99)00206-X.

[25] B. Khoda, A. M. M. N. Ahsan, and S. M. N. Shovon, "Dip Coating From Density Mismatching Mixture," *Journal of Micro and Nano-Manufacturing,* vol. 9, no. 2, 2021, doi: 10.1115/1.4051260.

[26] E. Rio and F. Boulogne, "Withdrawing a solid from a bath: How much liquid is coated?," vol. 247, ed: Elsevier B.V., 2017, pp. 100-114.

[27] B. Levich and L. Landau, "Dragging of a liquid by a moving plate," *Acta Physicochim. URSS,* vol. 17, p. 42, 1942.

[28] B. Deryagin and A. Titievskaya, "Experimental study of liquid film thickness left on a solid wall after receeding meniscus," 1945, vol. 50, p. 307.

[29] A. Einstein, "Berichtigung zu meiner Arbeit: „Eine neue Bestimmung der Moleküldimensionen”," *Annalen der Physik,* vol. 339, no. 3, pp. 591-592, 1911, doi: 10.1002/andp.19113390313.

[30] A. Gans, E. Dressaire, B. Colnet, G. Saingier, M. Z. Bazant, and A. Sauret, "Dip-coating of suspensions," *Soft Matter,* 10.1039/C8SM01785A vol. 15, no. 2, pp. 252-261, 2019, doi: 10.1039/C8SM01785A.

[31] S. Palma and H. Lhuissier, "Dip-coating with a particulate suspension," *Journal of Fluid Mechanics,* vol. 869, p. R3, 2019, Art no. R3, doi: 10.1017/jfm.2019.267.

[32] S. M. N. Shovon, I. Khalil, A. Alam, and B. Khoda, "Effect of Withdrawal Velocity on Particle Entrainment From Density Mismatched Mixture," 2022. [Online]. Available: https://doi.org/10.1115/MSEC2022-85745.

[33] A. Sauret, A. Gans, B. Colnet, G. Saingier, M. Z. Bazant, and E. Dressaire, "Capillary filtering of particles during dip coating," *Physical Review Fluids,* vol. 4, no. 5, 2019, doi: 10.1103/PhysRevFluids.4.054303.

[34] M. Alderliesten, "Mean Particle Diameters. Part VII. The Rosin-Rammler Size Distribution: Physical and Mathematical Properties and Relationships to Moment-Ratio Defined Mean Particle Diameters," *Particle & Particle Systems Characterization,* https://doi.org/10.1002/ppsc.201200021 vol. 30, no. 3, pp. 244-257, 2013/03/01 2013, doi: https://doi.org/10.1002/ppsc.201200021.

[35] Y. Bai, C. Wall, H. Pham, A. Esker, and C. B. Williams, "Characterizing Binder–Powder Interaction in Binder Jetting Additive Manufacturing Via Sessile Drop Goniometry,"

Journal of Manufacturing Science and Engineering, vol. 141, no. 1, 2018, doi: 10.1115/1.4041624.

[36] C. Y. Park and T. I. Zohdi, "Numerical Modeling of Thermo-Mechanically Induced Stress in Substrates for Droplet-Based Additive Manufacturing Processes," *Journal of Manufacturing Science and Engineering*, vol. 141, no. 6, 2019, doi: 10.1115/1.4043254.

[37] B. Khoda, A. M. M. N. Ahsan, A. N. Shovon, and A. I. Alam, "3D metal lattice structure manufacturing with continuous rods," *Scientific Reports*, vol. 11, no. 1, p. 434, 2021/01/11 2021, doi: 10.1038/s41598-020-79826-6.

[38] S. F. Kistler and P. Schweizer, "Liquid film coating : scientific principles and their technological implications," 1997.

[39] K. J. Ruschak, "Coating flows," *Annual Review of Fluid Mechanics*, vol. 17, no. 1, pp. 65-89, 1985.

[40] Y. Shimizu, S. Tupin, C. Kiyomitsu, K. Kitamura, K. Takashima, and M. Ohta, "Development of a stereo dip-coating system for fabrication of tube-shaped blood vessel models," *Scientific reports*, vol. 10, no. 1, pp. 1-10, 2020.

[41] B. M. Dincau, M. Z. Bazant, E. Dressaire, and A. Sauret, "Capillary Sorting of Particles by Dip Coating," *Physical Review Applied*, vol. 12, no. 1, pp. 011001-011001, 2019, doi: 10.1103/PhysRevApplied.12.011001.

[42] Q. Zhang, D. J. Roach, L. Geng, H. Chen, H. J. Qi, and D. Fang, "Highly stretchable and conductive fibers enabled by liquid metal dip-coating," *Smart Materials and Structures*, vol. 27, no. 3, p. 035019, 2018.

[43] M. S. Crosley and W. T. Yip, "Kinetically Doped Silica Sol-Gel Optical Biosensors: Expanding Potential Through Dip-Coating," *ACS Omega*, vol. 3, no. 7, pp. 7971-7978, 2018, doi: 10.1021/acsomega.8b00897.

[44] J. H. Burroughes *et al.*, "Light-emitting diodes based on conjugated polymers," *nature*, vol. 347, no. 6293, pp. 539-541, 1990.

[45] H.-L. Chou, S.-Y. Hsu, and P.-K. Wei, "Light emission in phase separated conjugated and non-conjugated polymer blends," *Polymer*, vol. 46, no. 13, pp. 4967-4970, 2005.

[46] H. G. W. Pierson, "18 - The Selection of Solid—Liquid Separation Equipment," in *Solid–Liquid Separation*, L. Svarovsky Ed.: Butterworth-Heinemann, 1977, pp. 313-326.

[47] D. A. White and J. A. Tallmadge, "A theory of withdrawal of cylinders from liquid baths," *AIChE Journal*, vol. 12, no. 2, pp. 333-339, 1966.

[48] I. M. Krieger and T. J. Dougherty, "A mechanism for non-Newtonian flow in suspensions of rigid spheres," *Transactions of the Society of Rheology,* vol. 3, no. 1, pp. 137-152, 1959.

[49] D. J. Jeffrey and A. Acrivos, "The rheological properties of suspensions of rigid particles," *AIChE Journal,* vol. 22, no. 3, pp. 417-432, 1976.

[50] S. M. N. Shovon, A. Alam, W. Gramlich, and B. Khoda, "Micro-particle entrainment from density mismatched liquid carrier system," *Scientific Reports,* vol. 12, no. 1, p. 9806, 2022/06/13 2022, doi: 10.1038/s41598-022-14162-5.

[51] G. Halász, B. Gyüre, I. M. Jánosi, K. G. Szabó, and T. Tél, "Vortex flow generated by a magnetic stirrer," *American Journal of Physics,* vol. 75, no. 12, pp. 1092-1098, 2007.

[52] T. Mahmud, J. N. Haque, K. J. Roberts, D. Rhodes, and D. Wilkinson, "Measurements and modelling of free-surface turbulent flows induced by a magnetic stirrer in an unbaffled stirred tank reactor," *Chemical Engineering Science,* vol. 64, no. 20, pp. 4197-4209, 2009, doi: 10.1016/j.ces.2009.06.059.

[53] T. N. Zwietering, "Suspending of solid particles in liquid by agitators," *Chemical engineering science,* vol. 8, no. 3-4, pp. 244-253, 1958.

[54] D. A. R. Brown, P. N. Jones, J. C. Middleton, G. Papadopoulos, and E. B. Arik, "Experimental Methods," in *Handbook of Industrial Mixing,* 2003, pp. 145-256.

[55] I. Ayranci and S. M. Kresta, "Critical analysis of Zwietering correlation for solids suspension in stirred tanks," *Chemical Engineering Research and Design,* vol. 92, no. 3, pp. 413-422, 2014.

[56] K. J. Myers, E. E. Janz, and J. B. Fasano, "Effect of solids loading on agitator just-suspended speed," *The Canadian Journal of Chemical Engineering,* vol. 91, no. 9, pp. 1508-1512, 2013.

[57] P. M. Armenante, E. U. Nagamine, and J. Susanto, "Determination of correlations to predict the minimum agitation speed for complete solid suspension in agitated vessels," *The Canadian Journal of Chemical Engineering,* vol. 76, no. 3, pp. 413-419, 1998.

[58] J. Oldshue and R. Sharma, "The Effect of Off-Bottom Distance of an Impellar for the" Just Suspended Speed" N~ j~ s," in *AIChE Symposium Series*, 1992, vol. 88: American Institute of Chemical Engineers, pp. 72-72.

[59] Y. Zhu and J. Wu, "Critical impeller speed for suspending solids in aerated agitation tanks," *The Canadian Journal of Chemical Engineering,* vol. 80, no. 4, pp. 1-6, 2002.

[60] F. Rieger and P. Ditl, "Suspension of solid particles," *Chemical Engineering Science,* vol. 49, no. 14, pp. 2219-2227, 1994.

[61] A. Brucato, A. Cipollina, G. Micale, F. Scargiali, and A. Tamburini, "Particle suspension in top-covered unbaffled tanks," *Chemical Engineering Science,* vol. 65, no. 10, pp. 3001-3008, 2010.

[62] A. Tamburini, A. Cipollina, G. Micale, and A. Brucato, "Dense solid-liquid suspensions in top-covered unbaffled stirred vessels," *Chem. Eng. Trans,* vol. 24, pp. 1441-1446, 2011.

[63] A. Brucato, "Determination of the amount of unsuspended solid particles inside stirred tanks by means of pressure measurements," in *Recents Progres en Genie des Procedes, Proc. 9th European Mixing Conf., Paris, France, 1997*, 1997, vol. 11, pp. 3-10.

[64] Y. Selima, Y. Fangary, and N. Mahmoud, "Determination of minimum speed required for solids suspension in stirred vessels using pressure measurements," *The Canadian Journal of Chemical Engineering,* vol. 86, no. 4, pp. 661-666, 2008.

[65] A. Tamburini, A. Cipollina, G. Micale, A. Brucato, and M. Ciofalo, "CFD simulations of dense solid–liquid suspensions in baffled stirred tanks: Prediction of suspension curves," *Chemical Engineering Journal,* vol. 178, pp. 324-341, 2011.

[66] M. Kraume, "Mixing times in stirred suspensions," *Chemical Engineering & Technology: Industrial Chemistry-Plant Equipment-Process Engineering-Biotechnology,* vol. 15, no. 5, pp. 313-318, 1992.

[67] M. Micheletti, L. Nikiforaki, K. C. Lee, and M. Yianneskis, "Particle concentration and mixing characteristics of moderate-to-dense solid− liquid suspensions," *Industrial & engineering chemistry research,* vol. 42, no. 24, pp. 6236-6249, 2003.

[68] R. Panneerselvam, S. Savithri, and G. D. Surender, "CFD modeling of gas–liquid–solid mechanically agitated contactor," *Chemical Engineering Research and Design,* vol. 86, no. 12, pp. 1331-1344, 2008.

[69] N. C. Kee and R. B. Tan, "CFD simulation of solids suspension in mixing vessels," *The Canadian Journal of Chemical Engineering,* vol. 80, no. 4, pp. 1-6, 2002.

[70] L. Musil and J. Vlk, "Suspending solid particles in an agitated conical-bottom tank," *Chemical Engineering Science,* vol. 33, no. 8, pp. 1123-1131, 1978.

[71] F. Wang, Z. Mao, and X. Shen, "Numerical study of solid-liquid two-phase flow in stirred tanks with Rushton impeller-(II) Prediction of critical impeller speed," *Chinese Journal of Chemical Engineering,* vol. 12, no. 5, pp. 610-614, 2004.

[72] B. Khoda, W. Gramlich, S. M. N. Shovon, and I. Khalil, "Effect of molecular weight on polymer solution facilitated transfer of non-Brownian particles," *Progress in Organic Coatings,* vol. 176, p. 107394, 2023/03/01/ 2023, doi: https://doi.org/10.1016/j.porgcoat.2022.107394.

[73] K. Nakanishi and M. Kurata, "Density measurement in dilute aqueous solution of polyvinyl alcohol," *Bulletin of the Chemical Society of Japan,* vol. 33, no. 2, pp. 152-157, 1960.

[74] S. Mueller, E. W. Llewellin, and H. M. Mader, "The rheology of suspensions of solid particles," *Proceedings of the Royal Society A: Mathematical, Physical and Engineering Sciences,* vol. 466, no. 2116, pp. 1201-1228, 2010, doi: 10.1098/rspa.2009.0445.

[75] D. Gilbert, R. Valette, and E. Lemaire, "Impact of particle stiffness on shear-thinning of non-Brownian suspensions," *Journal of Rheology,* vol. 66, no. 1, pp. 161-176, 2022.

[76] R. Pasquino, N. Grizzuti, P. L. Maffettone, and F. Greco, "Rheology of dilute and semidilute noncolloidal hard sphere suspensions," *Journal of Rheology,* vol. 52, no. 6, pp. 1369-1384, 2008.

[77] G. Barnocky and R. H. Davis, "Elastohydrodynamic collision and rebound of spheres: experimental verification," *The Physics of fluids,* vol. 31, no. 6, pp. 1324-1329, 1988.

[78] G. Joseph, R. Zenit, M. Hunt, and A. Rosenwinkel, "Particle–wall collisions in a viscous fluid," *Journal of Fluid Mechanics,* vol. 433, pp. 329-346, 2001.

[79] S. Veerapaneni, J. Wan, and T. K. Tokunaga, "Motion of Particles in Film Flow," *Environmental Science & Technology,* vol. 34, no. 12, pp. 2465-2471, 2000/06/01 2000, doi: 10.1021/es9912731.

[80] M. Corn, "The Adhesion of Solid Particles to Solid Surfaces, I. a Review," *Journal of the Air Pollution Control Association,* vol. 11, no. 11, pp. 523-528, 1961/11/01 1961, doi: 10.1080/00022470.1961.10468032.

[81] M. E. O'Neill, "A sphere in contact with a plane wall in a slow linear shear flow," *Chemical Engineering Science,* vol. 23, no. 11, pp. 1293-1298, 1968, doi: 10.1016/0009-2509(68)89039-6.

[82] R. Zenit, M. Hunt, and C. Brennen, "Collisional particle pressure measurements in solid–liquid flows," *Journal of Fluid Mechanics,* vol. 353, pp. 261-283, 1997.

[83] S. Banerjee and M. K. Mazumder, "Adhesion of charged powders on metal surface in powder coating process," in *Conference Record of the 1993 IEEE Industry Applications Conference Twenty-Eighth IAS Annual Meeting,* 2-8 Oct 1993 1993, pp. 1897-1901 vol.3, doi: 10.1109/IAS.1993.299114.

[84] A. Carlson, S. Wang, P. Elvikis, P. M. Ferreira, Y. Huang, and J. A. Rogers, "Active, Programmable Elastomeric Surfaces with Tunable Adhesion for Deterministic Assembly by Transfer Printing," vol. 22, no. 21, pp. 4476-4484, 2012, doi: https://doi.org/10.1002/adfm.201201023.

[85] L. L. Hench and J. K. West, "The sol-gel process," *Chemical Reviews,* vol. 90, no. 1, pp. 33-72, 1990/01/01 1990, doi: 10.1021/cr00099a003.

[86] C. J. Brinker, G. C. Frye, A. J. Hurd, and C. S. Ashley, "Fundamentals of sol-gel dip coating," *Thin Solid Films,* vol. 201, no. 1, pp. 97-108, 1991/06/05/ 1991, doi: https://doi.org/10.1016/0040-6090(91)90158-T.

[87] M. Ghosh, F. Fan, and K. J. Stebe, "Spontaneous Pattern Formation by Dip Coating of Colloidal Suspensions on Homogeneous Surfaces," *Langmuir,* vol. 23, no. 4, pp. 2180-2183, 2007/02/01 2007, doi: 10.1021/la062150e.

[88] T. Kitano, T. Kataoka, and T. Shirota, "An empirical equation of the relative viscosity of polymer melts filled with various inorganic fillers," *Rheologica Acta,* vol. 20, no. 2, pp. 207-209, 1981, doi: 10.1007/BF01513064.

[89] J. B. S. Hamm, A. Ambrosi, L. D. Pollo, N. R. Marcilio, and I. C. Tessaro, "Thin polymer layer-covered porous alumina tubular membranes prepared via a dip-coating/phase-inversion process," *Materials Chemistry and Physics,* vol. 265, p. 124511, 2021/06/01/ 2021, doi: https://doi.org/10.1016/j.matchemphys.2021.124511.

[90] L. E. Scriven, "Physics and Applications of DIP Coating and Spin Coating," *MRS Proceedings,* vol. 121, 1988, doi: 10.1557/proc-121-717.

[91] B. Khoda, A. M. M. Nazmul Ahsan, and S. M. N. Shovon, "Solid Transfer of Large Particles by Dipping in a Heterogeneous Mixture," in *ASME 2021 16th International Manufacturing Science and Engineering Conference*, 2021, vol. Volume 2: Manufacturing Processes; Manufacturing Systems; Nano/Micro/Meso Manufacturing; Quality and Reliability, V002T08A017, doi: 10.1115/msec2021-64079. [Online]. Available: https://doi.org/10.1115/MSEC2021-64079

[92] K. Arcaute and R. B. Wicker, "Patient-Specific Compliant Vessel Manufacturing Using Dip-Spin Coating of Rapid Prototyped Molds," *Journal of Manufacturing Science and Engineering,* vol. 130, no. 5, 2008, doi: 10.1115/1.2898839.

[93] I. Yu, S. Grindrod, and R. Chen, "Controllability Over Wall Thickness of Tubular Structures and Encapsulation During Co-Axial Extrusion of a Thermal-Crosslinking Hydrogel," *Journal of Manufacturing Science and Engineering,* vol. 142, no. 8, 2020, doi: 10.1115/1.4047091.

[94] R. Figueira, C. Silva, and E. Pereira, "Influence of Experimental Parameters Using the Dip-Coating Method on the Barrier Performance of Hybrid Sol-Gel Coatings in Strong Alkaline Environments," *Coatings,* vol. 5, no. 2, pp. 124-141, 2015, doi: 10.3390/coatings5020124.

[95] B. M. Dincau, M. Z. Bazant, E. Dressaire, and A. Sauret, "Capillary Sorting of Particles by Dip Coating," *Physical Review Applied,* vol. 12, no. 1, p. 011001, 07/16/ 2019, doi: 10.1103/PhysRevApplied.12.011001.

[96] B. M. Dincau, E. Mai, Q. Magdelaine, J. A. Lee, M. Z. Bazant, and A. Sauret, "Entrainment of particles during the withdrawal of a fiber from a dilute suspension," 2020.

[97] M. Alderliesten, "Mean Particle Diameters. Part VII. The Rosin-Rammler Size Distribution: Physical and Mathematical Properties and Relationships to Moment-Ratio Defined Mean Particle Diameters," vol. 30, no. 3, pp. 244-257, 2013, doi: https://doi.org/10.1002/ppsc.201200021.

[98] A. Rota, T. V. Duong, and T. Hartwig, "Micro powder metallurgy for the replicative production of metallic microstructures," *Microsystem Technologies,* vol. 8, no. 4, pp. 323-325, 2002/08/01 2002, doi: 10.1007/s00542-002-0157-y.

[99] E. W. Sequeiros, O. Emadinia, M. T. Vieira, and M. F. Vieira, "Development of Metal Powder Hot Embossing: A New Method for Micromanufacturing," vol. 10, no. 3, p. 388, 2020.

[100] B. B. Stogin, L. Gockowski, H. Feldstein, H. Claure, J. Wang, and T. S. Wong, "Free-standing liquid membranes as unusual particle separators," *Science Advances,* vol. 4, no. 8, pp. eaat3276-eaat3276, 2018, doi: 10.1126/sciadv.aat3276.

[101] R. W. Sheldon, "Size separation of marine seston by membrane and glass-fiber filters," *Limnology and Oceanography,* vol. 17, no. 3, pp. 494-498, 1972, doi: 10.4319/lo.1972.17.3.0494.

[102] D. Aussawasathien, C. Teerawattananon, and A. Vongachariya, "Separation of micron to sub-micron particles from water: Electrospun nylon-6 nanofibrous membranes as pre-filters," *Journal of Membrane Science,* vol. 315, no. 1-2, pp. 11-19, 2008, doi: 10.1016/j.memsci.2008.01.049.

[103] Y. E. Yu, S. Khodaparast, and H. A. Stone, "Separation of particles by size from a suspension using the motion of a confined bubble," *Applied Physics Letters,* vol. 112, no. 18, pp. 181604-181604, 2018, doi: 10.1063/1.5023341.

[104] C. Ness, R. Mari, and M. E. Cates, "Shaken and stirred: Random organization reduces viscosity and dissipation in granular suspensions," vol. 4, no. 3, p. eaar3296, 2018, doi: 10.1126/sciadv.aar3296 %J Science Advances.

[105] B. Khoda and A. M. M. N. Ahsan, "A Novel Rapid Manufacturing Process for Metal Lattice Structure," *3D Printing and Additive Manufacturing,* 2021, doi: 10.1089/3dp.2020.0184.

[106] S. Dhar, S. Chattopadhyay, and S. Majumdar, "Signature of jamming under steady shear in dense particulate suspensions," *Journal of Physics: Condensed Matter,* vol. 32, no. 12, p. 124002, 2019/12/19 2019, doi: 10.1088/1361-648x/ab5bd2.

[107] M. D. Rintoul and S. Torquato, "Computer simulations of dense hard-sphere systems," *Journal of Chemical Physics,* vol. 105, no. 20, pp. 9258-9265, 1996, doi: 10.1063/1.473004.

[108] É. Guazzelli and J. F. Morris, *A physical introduction to suspension dynamics*. Cambridge University Press, 2011, pp. 1-229.

[109] I. R. Rutgers, "Relative viscosity of suspensions of rigid spheres in Newtonian liquids," *Rheologica Acta,* vol. 2, no. 3, pp. 202-210, 1962, doi: 10.1007/BF01983952.

[110] A. Sauret, A. Gans, B. Colnet, G. Saingier, M. Z. Bazant, and E. Dressaire, "Capillary filtering of particles during dip coating," *Physical Review Fluids,* vol. 4, no. 5, pp. 054303-054303, 2019, doi: 10.1103/PhysRevFluids.4.054303.

[111] M. Faustini, B. Louis, P. A. Albouy, M. Kuemmel, and D. Grosso, "Preparation of Sol−Gel Films by Dip-Coating in Extreme Conditions," *The Journal of Physical Chemistry C,* vol. 114, no. 17, pp. 7637-7645, 2010/05/06 2010, doi: 10.1021/jp9114755.

[112] J. Lee and G. Son, "Numerical simulation of liquid film formation and evaporation in dip coating," *International Communications in Heat and Mass Transfer,* vol. 68, pp. 220-227, 2015/11/01/ 2015, doi: https://doi.org/10.1016/j.icheatmasstransfer.2015.09.008.

[113] N. B. Maledi, O. P. Oladijo, I. Botef, T. P. Ntsoane, A. Madiseng, and L. Moloisane, "Influence of cold spray parameters on the microstructures and residual stress of Zn coatings sprayed on mild steel," *Surface and Coatings Technology,* vol. 318, pp. 106-113, 2017/05/25/ 2017, doi: https://doi.org/10.1016/j.surfcoat.2017.03.062.

[114] H. MacHrafi, "Universal relation between the density and the viscosity of dispersions of nanoparticles and stabilized emulsions," *Nanoscale,* vol. 12, no. 28, pp. 15081-15101, 2020, doi: 10.1039/d0nr03130e.

[115] S. Palma and H. Lhuissier, "Dip-coating with a particulate suspension," *Journal of Fluid Mechanics,* vol. 869, pp. R3-R3, 2019, doi: 10.1017/jfm.2019.267.

[116] A. Habib and B. Khoda, "Fiber-Filled Hybrid Hydrogel for Bio-Manufacturing," *Journal of Manufacturing Science and Engineering,* vol. 143, no. 4, 2021, doi: 10.1115/1.4049479.

[117] W. A. Clifford, "The Ashley Book of Knots," ed: Doubleday, New York, 1944.

[118] D. E. Moulton, P. Grandgeorge, and S. Neukirch, "Stable elastic knots with no self-contact," *Journal of the Mechanics and Physics of Solids,* vol. 116, pp. 33-53, 2018.

[119] K. Jawed, P. Dieleman, B. Audoly, and P. Reis, "Untangling the Mechanics and Topology in the Frictional Response of Long Overhand Elastic Knots," *Physical Review Letters,* vol. 115, 08/01 2015, doi: 10.1103/PhysRevLett.115.118302.

[120] V. P. Patil, Ž. Kos, M. Ravnik, and J. Dunkel, "Discharging dynamics of topological batteries," *Physical Review Research,* vol. 2, no. 4, p. 043196, 2020.

[121] N. Clauvelin, B. Audoly, and S. Neukirch, "Matched asymptotic expansions for twisted elastic knots: a self-contact problem with non-trivial contact topology," *Journal of the Mechanics and Physics of Solids,* vol. 57, no. 9, pp. 1623-1656, 2009.

[122] G. Daviet, F. Bertails-Descoubes, and L. Boissieux, "A hybrid iterative solver for robustly capturing coulomb friction in hair dynamics," in *Proceedings of the 2011 SIGGRAPH Asia Conference,* 2011, pp. 1-12.

[123] D. Durville, "Contact-friction modeling within elastic beam assemblies: an application to knot tightening," *Computational Mechanics,* vol. 49, no. 6, pp. 687-707, 2012.

[124] D. M. Kaufman, R. Tamstorf, B. Smith, J.-M. Aubry, and E. Grinspun, "Adaptive nonlinearity for collisions in complex rod assemblies," *ACM Transactions on Graphics (TOG),* vol. 33, no. 4, pp. 1-12, 2014.

[125] A. Choi, D. Tong, M. K. Jawed, and J. Joo, "Implicit contact model for discrete elastic rods in knot tying," *Journal of Applied Mechanics,* vol. 88, no. 5, 2021.

[126] M. Li *et al.*, "Incremental potential contact: intersection-and inversion-free, large-deformation dynamics," *ACM Trans. Graph.,* vol. 39, no. 4, p. 49, 2020.

[127] V. P. Patil, J. D. Sandt, M. Kolle, and J. Dunkel, "Topological mechanics of knots and tangles," *Science,* vol. 367, no. 6473, pp. 71-75, 2020.

[128] S. C. Han, J. M. Choi, G. Liu, and K. Kang, "A microscopic shell structure with Schwarz's D-surface," *Scientific reports,* vol. 7, no. 1, pp. 1-8, 2017.

[129] Y. Xiao *et al.*, "Sheet collapsing approach for rubber-like graphene papers," *ACS nano,* vol. 11, no. 8, pp. 8092-8102, 2017.

[130] J. Park, K. Shin, and C. Lee, "Optimized design for anti-reflection coating process in roll-to-roll slot-die coating system," *Robotics and Computer-Integrated Manufacturing,* vol. 30, no. 5, pp. 432-441, 2014.

[131] J. Ressel, O. Seewald, W. Bremser, H.-P. Reicher, and O. I. Strube, "Low friction poly (amide-imide) coatings with silicones as tethered liquids," *Progress in Organic Coatings,* vol. 124, pp. 1-7, 2018.

[132] M. Iijima *et al.*, "Effect of coating on properties of esthetic orthodontic nickel-titanium wires," *The Angle Orthodontist,* vol. 82, no. 2, pp. 319-325, 2012.

[133] Y. Kikuchi, V. B. Graves, C. M. Strother, J. C. McDermott, S. G. Babel, and A. B. Crummy, "A new guidewire with kink-resistant core and low-friction coating," *Cardiovascular and interventional radiology,* vol. 12, pp. 107-109, 1989.

[134] T. J. Murray, "Poly (amide-imides): Wire Enamels with Excellent Thermal and Chemical Properties," *Macromolecular Materials and Engineering,* vol. 293, no. 5, pp. 350-360, 2008.

[135] K. Holmberg, "A concept for friction mechanisms of coated surfaces," *Surface and Coatings Technology,* vol. 56, no. 1, pp. 1-10, 1992.

[136] N. K. M. S. Islam *et al.*, "Manufacture by Selective Laser Melting & Physical Behaviour of Commercial 316L Stainless Steel," in *International Medical Device and Technology Conference*, 2017, vol. 2017, pp. 87-89.

[137] U. Ali, K. J. B. A. Karim, and N. A. Buang, "A review of the properties and applications of poly (methyl methacrylate)(PMMA)," *Polymer Reviews,* vol. 55, no. 4, pp. 678-705, 2015.

[138] J. Riddick, W. Bunger, and T. Sakano, "Techniques of chemistry, organic solvents," ed: John Wiley and Sons: New York, NY, 1985.

[139] B. G. Prevo, D. M. Kuncicky, and O. D. Velev, "Engineered deposition of coatings from nano-and micro-particles: A brief review of convective assembly at high volume fraction," *Colloids and Surfaces A: Physicochemical and Engineering Aspects,* vol. 311, no. 1-3, pp. 2-10, 2007.

[140] M. Sinclair, E. Ofek, M. Gonzalez-Franco, and C. Holz, "Capstancrunch: A haptic vr controller with user-supplied force feedback," in *Proceedings of the 32nd annual ACM symposium on user interface software and technology*, 2019, pp. 815-829.

[141] M. Bergou, M. Wardetzky, S. Robinson, B. Audoly, and E. Grinspun, "Discrete elastic rods," in *ACM SIGGRAPH 2008 papers*, 2008, pp. 1-12.

[142] M. Bergou, B. Audoly, E. Vouga, M. Wardetzky, and E. Grinspun, "Discrete viscous threads," *ACM Transactions on graphics (TOG),* vol. 29, no. 4, pp. 1-10, 2010.

[143] M. K. Jawed, A. Novelia, and O. M. O'Reilly, *A primer on the kinematics of discrete elastic rods*. Springer, 2018.

[144] M. K. Jawed, F. Da, J. Joo, E. Grinspun, and P. M. Reis, "Coiling of elastic rods on rigid substrates," *Proceedings of the National Academy of Sciences,* vol. 111, no. 41, pp. 14663-14668, 2014.

[145] M. K. Jawed, N. K. Khouri, F. Da, E. Grinspun, and P. M. Reis, "Propulsion and instability of a flexible helical rod rotating in a viscous fluid," *Physical review letters,* vol. 115, no. 16, p. 168101, 2015.

[146] C. Baek, A. O. Sageman-Furnas, M. K. Jawed, and P. M. Reis, "Form finding in elastic gridshells," *Proceedings of the National Academy of Sciences,* vol. 115, no. 1, pp. 75-80, 2018.

[147] V. J. Lumelsky, "On fast computation of distance between line segments," *Information Processing Letters,* vol. 21, no. 2, pp. 55-61, 1985.

APPENDICES

Appendix A. Simulations by Discrete Elastic Rods

The computational framework, based on discrete elastic rods (DERs) [141, 142], recently proposed in Ref. [125] was adopted and extended in this work for simulating knots with a systematic variation of frictional contact. DER, as a discrete-differential-geometry-based framework [143], was first introduced by the computer science community and is becoming progressively attractive to engineering disciplines for its high accuracy and low computational cost across various physical scenarios, i.e., coiling patterns on the moving substrate [144], buckling of rotating flagella [145], grid shells [146], etc.

In DER, as shown in Figure 35(a), an elastic rod will be discretized into $N + 1$ nodes x_i, where i is in the range from 0 to N, and N edges $e^i = x_{i+1} - x_i$. Subscripts are used for quantities associated with nodes and superscripts for those with edges. Each edge e_i is attached with two orthogonal frames: reference frame $[t^i, d^i_1, d^i_2]$ and material frame $[t^i, m^i_1, m^i_2]$. The reference frame is predefined at initial time t = 0 s, and the material frame can be obtained based on the reference frame with a rotation angle θ_i. $3N + 3$ nodal positions and N rotation angles can constitute the vector of a $4N + 3$ degrees-of-freedom:

$$q = [x_0, \theta^0, x_1, \theta^1, \ldots, x_{N-1}, \theta^{N-1}, x_N]^T \quad (1)$$

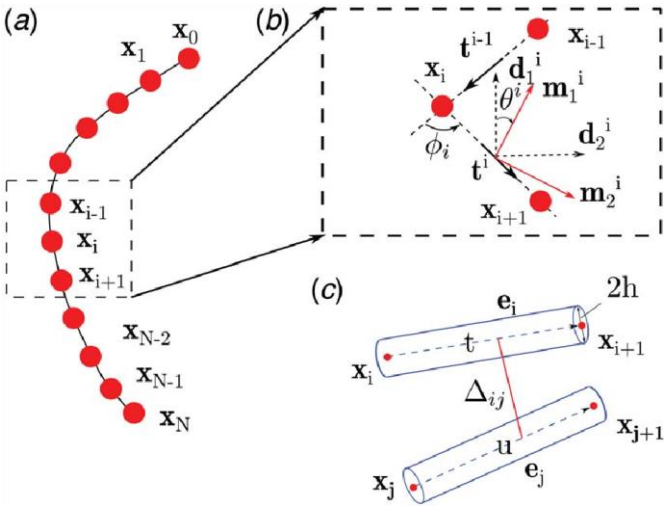

Figure 35: Discrete schematic and relevant notations: (a) discrete schematic of an elastic rod, (b) discrete notations about the reference frame [t^i, $d_1{}^i$, $d_2{}^i$], the material frame [t^i, $m_1{}^i$, $m_2{}^i$], the twist angle θ^i, and the turning angle ϕ^i, and (c) schematic diagram of a contact pair including the edge e_i and e_j

The equations of motion (EOM) can be constructed by the elastic energies of the rod, such as stretching, bending, and twisting energy, as well as external forces, like contact and friction, represented by the generalized coordinate in Eq. (1). Specifically, the stretching energy is defined as

$$E_i^s = \sum_{i=0}^{n-1} \frac{1}{2} EA \left(1 - \frac{||e_i||}{||\bar{e}_i||}\right)^2 ||\bar{e}_i|| \tag{2}$$

where EA is the stretching stiffness, E is the Young's modulus, A is the cross-sectional area, and $\bar{e}_i$ is the undeformed edge. Hereafter, all quantities with a bar mean the quantities under undeformed status. Next, the bending energy is written as

$$E_i^b = \sum_{i=1}^{n-1} \frac{1}{2} \frac{EI}{||\bar{e}_i||} \left(2tan\frac{\phi_i}{2} - 2tan\frac{\overline{\phi_i}}{2}\right)^2 \tag{3}$$

where EI is the bending stiffness, $I = \pi r_0^4/4$ is the moment of inertia, r_0 is the rod radius, and ϕ_i is the turning angle which is shown in Figure 35(b). After that, the twisting energy is defined as follows:

$$E_i^t = \sum_{i=2}^{n-} \frac{1}{2} \frac{GJ}{||\bar{e}_i||} (\tau - \bar{\tau})^2 \quad (4)$$

where GJ is the twisting stiffness, $G = E/2(1 + v)$ is the shear modulus, v is the Poisson's ratio, $J = \pi r_0^4/2$ is the polar second moment of inertia, $\tau_i = \theta_{i+1} - \theta_i + \Delta\tau^{ref}$ is the discrete twist at node $\mathbf{q}_i$, and $\Delta\tau^{ref}$ is the discrete reference twist. Then the internal force of the ith node F_i^{int} is defined in terms of energy as

$$F_i^{int} = \frac{\partial(E_i^s + E_i^b + E_i^t)}{\partial \mathbf{q}_i} \quad (5)$$

With that, the EOM for the system is written as

$$\boldsymbol{M\ddot{q}} - \boldsymbol{F}^{int} - \boldsymbol{F}^{ext} = 0 \quad (6)$$

In the DER algorithm, the implicit Euler method is implemented for time integration of the EOM, updating the status of $\mathbf{q}$ from told to $t_{new} + \Delta t$. Hereafter, all quantities with the subscript "new" mean that status is unknown, and quantities associated with the subscript "old" are known. Then, EOM is formulated as

$$f(\boldsymbol{q}_{new}) = \frac{M}{\Delta t}\left(\frac{\boldsymbol{q}_{new} - \boldsymbol{q}_{old}}{\Delta t} - \dot{\boldsymbol{q}}_{old}\right) - \boldsymbol{F}_{new}^{int} - \boldsymbol{F}_{new}^{ext} = 0 \quad (7)$$

Where $\boldsymbol{F}_{new}^{int}$ is defined as

$$\boldsymbol{F}_{new}^{int} = \frac{\partial(E_i^s + E_i^b + E_t E_i^t)}{\partial \mathbf{q}_{new}} \quad (8)$$

In Eq. (7), M is the diagonal mass matrix (size is $4N + 3 \times 4N + 3$), $\mathbf{F}^{int}$ are the elastic forces, and $\mathbf{F}^{ext}$ are the external forces. ($\dot{}$) stands for the derivative via time. In the knot tying case, $\mathbf{F}^{ext}$ includes contact forces F^c and friction forces F^r. The Newton-Raphson method was used to find the root of $f(\mathbf{q}_{new}) = 0$ of Eq. 7, in which the Jacobian of Eq. (7) is defined as

$$\boldsymbol{J}_{ij} = \frac{m_i}{\Delta t^2}\delta_{ij} + \frac{\partial^2 (E_s + E_b + E_t)_{new}}{\partial \boldsymbol{q}_i \partial \boldsymbol{q}_j} \tag{9}$$

where m_i is the mass of ith node, δ_{ij} is the Kronecker delta ($\delta_{ij} = 1$ when $i = j$, and $\delta_{ij} = 0$ when $i \neq j$), $\mathbf{J}_{ij}^c$ is the Jacobian of contact forces, and $\mathbf{J}_{ij}^r$ is the Jacobian of friction forces. The Jacobian of elastic energies can be obtained with Eqs. (2)-(4). More details of frictional contact forces $\mathbf{F}^c$ and $\mathbf{F}^r$ and their Jacobians $\mathbf{J}^c$ and $\mathbf{J}^r$ can be found in Ref. [125].

In addition to the elastic energies in DER formulation, contact and friction forces are also critical for simulating overhand knots. The contact energy and force model in Ref. [125] was adopted in this study, which is a penalty energy-based method. In this frictional contact, frictional contact is regarded as a constraint by introducing penalty energy when solving the EOM.

A contact pair is defined by combining two edges e_i and e_j, shown in Figure 35(c), which is made up of nodes $\mathbf{x}_i$, $\mathbf{x}_{i+1}$, $\mathbf{x}_j$, and $\mathbf{x}_{j+1}$. Therefore, a contact pair can be denoted as the following vector concatenation, $\mathbf{x}_{ij}$: = ($\mathbf{x}_i$, $\mathbf{x}_{i+1}$, $\mathbf{x}_j$, $\mathbf{x}_{j+1}$) (size 12 × 1). The formulation of the contact energy from Ref. [125] is written as

$$E(\boldsymbol{X}_{ij}) = \frac{\log(1+\exp(ce_k(2h-\Delta_{ij})))}{ce_k} \tag{10}$$

where ce_k is the contact stiffness—a user-defined parameter—which can determine the magnitude of the contact forces, and h is the radius of the rod. The advantages of the above formulation of contact modeling are (1) the penetration between edges is avoided by introducing artificial penalty

energy as a constraint. (2) Different from the Lumelsky algorithm [147], where the artificial energy is treated as a piecewise function, a smooth function is used to approximate the contact energy. Therefore, contact forces F_{ij}^{c} can be obtained via the negative gradient of the contact energy as $F_{ij}^{c} = -\nabla E(\mathbf{x}_{ij})$, and the Jacobian $\mathbf{J}_{ij}^{c}$ can be obtained via the negative hessian of the contact energy through chain rules.

From Coulomb's friction, magnitude of friction forces is irrelevant with the relative velocity between edges ei and ej. When sliding between two edges happens, the magnitude of friction force is $||\mathbf{F}^{fr}|| = \mu||F^{n}||$, where μ is the friction coefficient and F^{n} is the normal force. As mentioned before, the normal forces between edges e_i and e_j are $\mathbf{F}_{ij}^{c} = -\nabla E(\mathbf{x}_{ij})$. Therefore, we can define the normal contact force which is $\mathbf{F}^{n} = \mathbf{F}_{i}^{c} + \mathbf{F}_{j}^{c}$. The contact normal can also be calculated simply through $\mathbf{n} = \mathbf{F}^{n}/||\mathbf{F}^{n}||$. The direction of friction $\mathbf{F}^{fr}$ is then determined by tangential component of the relative velocity $(v^{rel})^{T}$. For simplicity, we approximate the relative velocity as the relative velocity between the middle points of two edges.

$$\mathbf{V}^{\text{rel}} = 0.5(\mathbf{V}_i + \mathbf{V}_{i+1}) - 0.5(\mathbf{V}_j + \mathbf{V}_{j+1})$$

$$(\mathbf{V}^{\text{rel}})^{T} = \mathbf{V}^{\text{rel}} - (\mathbf{V}^{\text{rel}} \cdot \mathbf{n})\mathbf{n} \tag{11}$$

$$(\overline{\mathbf{V}^{\text{rel}}})^{T} = \frac{(\mathbf{V}^{\text{rel}})^{T}}{||(\mathbf{V}^{\text{rel}})^{T}||}$$

wherein v_i and v_j are nodal velocities. With Eq. (11), we determine the direction of the frictional forces. In order to simulate the static frictional forces, we introduce a weight $\gamma \in [0, 1]$, which will adjust the magnitude of frictional forces based on the sliding (tangential components of relative velocity): when γ is close to 1, the friction formulation will be the sliding friction; when γ is not

close to 1, the sliding between the contacted segments should be small enough to simulate the static phenomena. Note that the frictional responses cannot be larger than $\mu||F^n||$.

$$\gamma = \frac{1}{1+\exp(-k(||(\mathbf{V}^{\mathrm{rel}})^T||-c))}$$

$$\mathbf{F}^{fr} = -\gamma\left(\overline{\mathbf{V}^{\mathrm{rel}}}\right)^T \mu||F^n|| \tag{12}$$

$$\mathbf{F}_{ij}^{fr} = (0.5\mathbf{F}^{fr}, 0.5\mathbf{F}^{fr}, -0.5\mathbf{F}^{fr}, -0.5\mathbf{F}^{fr})$$

Note that *k* and *c* are hyperparameters that users can adjust. The definition of *c* is described before, and *c* states the limit for the step transition. During the simulation, we set all k as $50/r_0$ and *c* as $0.15r_0$. Under such parameters, γ will be close to 1 when the magnitude of the relative velocity is larger than 0.205 mm/s. In other words, when $||v^{\mathrm{rel}}|| > 0.205$ mm/s, the dominant friction forces will be sliding friction. $\mathbf{F}_{ij}^{fr}$ is a 12 × 1 force vector that can be added to discrete nodes of the rod, and its Jacobian $\mathbf{J}_{ij}^{fr}$ can be calculated with the chain rule as well. More details are available in Ref. [125].

The pulling force measured in the experiment is treated as an external force at the boundary in DER simulation to determine the friction coefficient.

BIOGRAPHY OF THE AUTHOR

Md Ibrahim was born in Cumilla Bangladesh on December 31st, 1993. He raised in Dhaka Bangladesh and graduated from Ideal School and College and later Dhaka college. He completed his undergraduate in Mechanical Engineering from Bangladesh University of Engineering and Technology (BUET) in September 2017. He started his MS in Mechanical Engineering in Fall 2020 at the University of Maine with Dr. Bashir Khoda.

Ibrahim is a candidate for the Master of Science in Mechanical Engineering from the University of Maine in May 2023.